Max-Planck-Institut für Quantenoptik
Technische Universität München

Classical and Quantum Dynamics of a Strongly Coupled Atom-Cavity System

Markus Koch

Vollständiger Abdruck der von der Fakultät für Physik der Technischen Universität München zur Erlangung des akademischen Grades eines

Doktors der Naturwissenschaften (Dr. rer. nat.)

genehmigten Dissertation.

Vorsitzender :		Univ.-Prof. Dr. W. Zwerger
Prüfer der Dissertation :	1.	Hon.-Prof. Dr. G. Rempe
	2.	Univ.-Prof. Dr. R. Gross

Die Dissertation wurde am 27.10.2011 bei der Technischen Universität München eingereicht und durch die Fakultät für Physik am 20.12.2011 angenommen.

Technische Universität München

Physik Department

MPQ

Classical and Quantum Dynamics of a Strongly Coupled Atom-Cavity System

Markus Koch

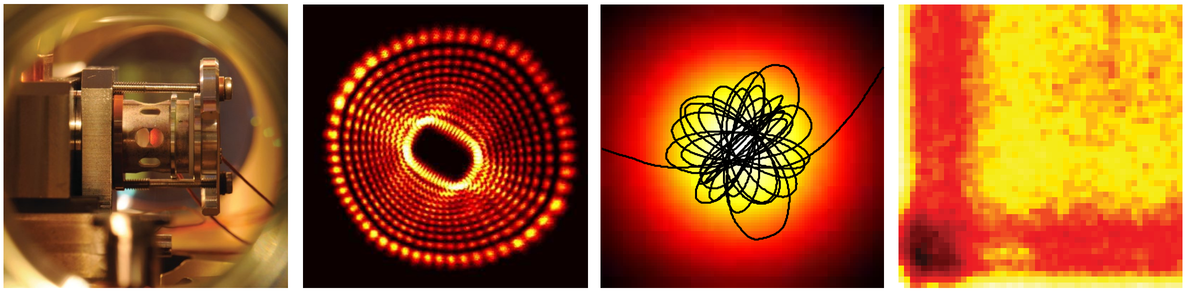

Dissertation

Max-Planck-Institut für Quantenoptik, Garching
and Physik Department, Technische Universität München

Oktober 2011

Cover illustration (from left to right): Photograph of the Fabry-Pérot resonator, Laguerre-Gaussian resonator mode, simulated trajectory of an atom trapped in an intracavity dipole trap, third-order correlation function.

Abstract

A single two-level atom interacting with just a single mode of the quantized electromagnetic field constitutes one of the most fundamental systems in quantum optics. We realize this situation in an experiment strongly coupling individual rubidium atoms to the mode of an optical high-finesse Fabry-Pérot cavity. The new experimental apparatus described in this work stands out due to a high detection efficiency, a length-adjustable cavity and excellent optical access.

We investigate the mode spectrum of the empty Fabry-Pérot cavity. We observe systematic deviations from the paraxial approximation. The resulting, fine-structure-like splitting is in excellent agreement with recent theoretical calculations taking into account corrections to the paraxial approximation. Moreover, we confirm predictions for a spin-orbit-like splitting due to the coupling between orbital and intrinsic angular momentum of the light modes.

Next, we trap individual rubidium atoms in an intracavity dipole trap. The transmission of a near-resonant probe beam carries information about the trajectory of the atom. Based on this information, we apply a feedback algorithm cooling the atomic motion and dramatically increasing the average storage time. This demonstration of feedback cooling of individual neutral particles nicely illustrates the degree of control over individual particles that is nowadays possible. The versatility of our cooling scheme makes it a very useful technique for future investigations of the atom-cavity system. It can easily be adapted to other strong-coupling cavity quantum electrodynamics experiments with atoms or ions.

In contrast to the atomic motion, which, in our case, can be considered classically, the internal degrees of freedom of the atom-cavity system are a genuine quantum system. Their dynamics, described by the Schrödinger equation, is inevitably perturbed by any attempt to observe it. This gives rise to complex quantum trajectories, in which the coherent evolution, due to the atom-cavity coupling and the driving of the system, is interrupted by unpredictable quantum jumps when an observation of the system, for example the detection of a photon leaking from the cavity, is made. We investigate the resulting dissipative quantum dynamics under strong driving where the excitation of multi-photon states gives rise to characteristic temporal patterns in the emitted photon stream. We characterize these by means of second- and third-order time-dependent intensity correlation functions. We observe the coherent exchange of photons between the atom and the cavity, between the atom-cavity system and the driving laser, and we find evidence for the dynamics of higher-order dressed states. Moreover, we observe a time-asymmetry in the emitted photon stream.

These results provide new insights into the quantum dynamics of a strongly coupled atom-cavity system with the perspective to control these dynamics by means of feedback. Moreover, we establish time-dependent third-order intensity correlation functions as a new tool to study complex quantum trajectories, which might also find applications for investigations of other open quantum systems.

Zusammenfassung

Ein einzelnes Zweiniveauatom, das mit einer einzelnen Mode des quantisierten elektromagnetischen Feldes wechselwirkt, stellt eines der fundamentalsten Systeme der Quantenoptik dar. Wir realisieren dies in einem Experiment, in dem wir einzelne Rubidiumatome an die Mode eines optischen Fabry-Pérot-Resonators hoher Güte koppeln. Die neue experimentelle Apparatur, die im Rahmen dieser Arbeit aufgebaut wurde, zeichnet sich dabei durch eine hohe Detektionseffizienz, einen längenveränderbaren Resonator sowie einen sehr guten optischen Zugang aus.

Zunächst untersuchen wir das Modenspektrum des leeren Resonators. Dabei beobachten wir systematische Abweichungen von der paraxialen Näherung. Die resultierende, Feinstruktur ähnliche Aufspaltung stimmt gut mit aktuellen theoretischen Berechnungen von Korrekturen zur paraxialen Näherung überein.

Als Nächstes fangen wir einzelne Atome in einer Dipolfalle in dem optischen Resonator. Die Transmission eines nahresonanten Lasers liefert uns Informationen über die Trajektorie des Atoms. Dies erlaubt es uns die Bewegung des Atoms durch eine Rückkoppelungsschleife zu kühlen, was zu einer erheblichen Verlängerung der mittleren Speicherzeit um einen Faktor 30 auf über 1 s führt.

Im Gegensatz zur Bewegung der Atome, die in unserem Fall klassisch beschrieben werden kann, sind die internen Freiheitsgrade des Atom-Resonator-Systems ein eindeutig quantenmechanisches System. Die Dynamik des Quantenzustandes, die durch die Schrödinger Gleichung beschrieben wird, wird notwendigerweise durch jeden Versuch sie zu beobachten gestört. Aus dem Zusammenspiel der kohärenten Dynamik durch die Atom-Resonator-Kopplung und das Treiben des Systems auf der einen Seite und dem zufälligen Auftreten von Quantensprüngen auf der anderen Seite ergeben sich komplexe Quantentrajektorien. Wir untersuchen die resultierende dissipative Quantendynamik, wenn das System stark getrieben wird. In diesem Fall führt die Besetzung von Mehrphotonenzuständen zu charakteristischen Mustern in der zeitlichen Verteilung der emittierten Photonen. Wir untersuchen diese durch die Analyse von zeitabhängigen Korrelationsfunktionen zweiter und dritter Ordnung. Wir beobachten den kohärenten Austausch von Photonen zwischen dem Atom und dem Resonator, zwischen dem Atom-Resonator-System und dem treibenden Laser und finden erste Hinweise auf die Dynamik der Zweiphotonzustände des gekoppelten Systems. Darüber hinaus weisen wir erstmalig eine zeitliche Asymmetrie in dem emittierten Photonenfluss nach.

Diese Ergebnisse vertiefen unser Verständnis der Dynamik eines stark gekoppelten Atom-Resonator-Systems. Außerdem etablieren sie Korrelationsfunktionen dritter Ordnung als neuartiges Hilfsmittel, um die komplexe Dynamik offener Quantensystem zu untersuchen - eine Methode, die möglicherweise auch Anwendungen zur Untersuchung anderer physikalischer Systeme finden wird.

Valentine: *Distortion. Interference. Real data is messy. (...) It's all very, very noisy out there. Very hard to spot the tune. Like a piano player in the next room, it's playing your song, but unfortunately it's out of whack, some strings are missing, and the pianist is tone deaf and drunk - I mean, the noise! Impossible!*

Hannah: *What do you do?*

Valentine: *You start guessing what the tune might be. You try to pick it out of the noise. You try this, you try that, you start to get something - it's half baked but you start putting in notes which are missing or not quite the right notes ... and bit by bit.. Dumdi-dum-dum, dear Val-en-tine, dumdidum-dum to you - the lost algorithm.*

Hannah: *Yes, I see. And then what?*

Valentine: *I publish.*

Tom Stoppard
Arcadia, 1993

Contents

List of Figures

Chapter 1

Introduction

1.1 Cavity Quantum Electrodynamics

Our understanding of the interaction between light and matter has profoundly changed throughout the last centuries. A first quantitative description was achieved by the Lorentz model in the 19^{th} century. It modeled atoms as oscillating dipoles interacting according to Newton's and Maxwell's laws with electromagnetic light waves. The advent of quantum mechanics at the beginning of the 20^{th} century refined our understanding of the atomic structure. This lead to the semi-classical theory of light-matter interaction by Schrödinger [1], in which the light field is treated classically, whereas quantum mechanics is employed to describe the atom. The most recent conceptual change was the quantization of the electro-magnetic field, first introduced heuristically by Planck and Einstein, but later on formalized as quantum electrodynamics (QED) by Dirac, Dyson, Feynman, Schwinger, Tomonaga and many others [2, 3].

In practice, quantum electrodynamics is a quite sophisticated theory, and it is used almost exclusively in a perturbative way to calculate scattering rates (e.g. spontaneous emission [4]), perturbative shifts (e.g. Lamb shifts [5]) or anomalous magnetic moments [6]. Exact calculations are difficult because of the infinity of modes of the electro-magnetic field that have to be taken into account. Moreover, it was found that some of the effects that are nowadays commonly assumed to be a direct consequence of the quantization of light, for example the photoelectric effect [7, 8], spontaneous emission [9] and even the Lamb shift [10], can be reproduced, at least qualitatively, in semi-classical models. This motivated Jaynes and Cummings to investigate theoretically the simplest possible system in which light-matter interaction occurs: a single two-level atom interacting with a single mode of the electro-magnetic field [11]. As in this case, exact calculations, even in the full quantum model, can be made, it is an ideal system to study the consequences of the quantization of the electro-magnetic field for the interaction between light and matter and, in particular, the differences with respect to different, e.g., semi-classical, models.

First considered merely as a Gedankenexperiment, it was soon realized that Jaynes' and Cummings' model could indeed be implemented in an experiment by placing a single two-level atom in a cavity with a very small mode volume. The latter is necessary to enhance the interaction between the atom and the mode of the resonator, such that all other modes can be neglected. In practice, this amounts to setting two conditions: First, the interaction strength between the cavity mode and the atom has to surpass the spontaneous emission rate of the atom, which can be achieved by reducing the mode volume of the cavity. Second, the interaction strength has to surpass the decay rate of the cavity, which requires a cavity with low losses, i.e., a high finesse. If both conditions are met, the system is said to be in the strong-coupling regime, as it can be demonstrated either by the observation of the normal-mode splitting, i.e., an avoided crossing between the cavity and the atomic resonance in the spectrum of the system, or by the direct observation of the coherent exchange of energy between the atom and the cavity, the vacuum Rabi oscillations. Either one of these signatures has been reported on for a variety of physical systems, such as Rydberg atoms in microwave cavities [12, 13], alkali atoms in Fabry-Pérot cavities [14, 15, 16, 17, 18] and in the evanescent field of microtoroidal resonators [19], quantum dots in semiconductor microcavities [20, 21, 22, 23] and photonic crystal cavities [24] and superconducting qubits in microwave resonators [25, 26, 27, 28].

This experimental progress has been accompanied by the development of new theoretical methods to describe the atom-cavity system in the presence of dissipation [29, 30]. In parallel, it was realized that a plethora of effects can be observed in this seemingly simple physical system going far beyond what Jaynes and Cummings originally envisioned. Generation of non-classical states of light, quantum non-demolition measurements, fundamental studies of decoherence and dissipative quantum systems, quantum communication, new cooling techniques for atoms and ions, quantum computation or feedback on quantum systems are just a few examples of research topics that are nowadays addressed in the field of cavity QED filling textbooks [31, 32, 33] and review articles [34, 35, 36, 37, 38].

In the course of this thesis, a new experimental apparatus was set up that achieves strong coupling between individual ^{85}Rb atoms and an optical mode of a high-finesse Fabry-Pérot cavity. The main improvements compared to the predecessor experiment [39] are an asymmetric cavity with coned mirrors providing a high detection efficiency and transverse optical access, respectively. Moreover, the cavity length can be adjusted via an inchworm piezo motor thus improving the versatility of the setup considerably.

1.2 Classical Dynamics in Cavity QED

The main focus of this work lies on investigations of the dynamics of a coupled atom-cavity system. Speaking of the dynamics, two very different degrees of freedom are considered. The first is the center of mass motion of the atom in the cavity mode. Our interest is motivated by the necessity to localize atoms within the cavity mode and by the potential to realize new, unprecedented cooling and trapping schemes beyond conventional laser cooling of atoms in free space.

The atomic motion and means to control it has been a reappearing theme in optical cavity QED experiments with neutral atoms ever since the first achievement of strong coupling in this system [14]. While the first experiments used thermal beams of atoms passing through the cavity, the application of laser cooling and trapping techniques [40] was prerequisite for many of the forthcoming experiments requiring better control over the atom number and longer interaction times.

The injection of ultra-cold atoms into the cavity mode by means of an atomic fountain or a magneto-optical trap was the first step in this direction. For the first time, individual atoms, passing through the cavity mode, could be observed [41, 42]. At the same time, it was found that strong coupling enables new techniques to manipulate and observe the atomic motion. First, the light forces induced by the near-resonant probe light strongly deviate from those in free space [43]. This enabled the trapping of individual atoms with the near-resonant probe light field containing on average less than one photon [44], and it opened up the new perspective of cavity cooling. Second, it was found that the transmitted intensity of a near-resonant probe field carries information about the position of the atom in the cavity [45]. This motivated the first attempts to control and cool the atomic motion by means of a simple feedback algorithm [46]. In these very first experiments with trapped atoms, storage times below 1 ms were observed.

Both cooling schemes, cavity cooling and feedback cooling, were considerably improved by the successive implementation of additional red-detuned [47, 48] and blue-detuned [49] dipole traps. The first enabled the direct demonstration of cavity cooling [50]. The latter led to significant improvement of the feedback scheme [51] achieving average storage times on the order of several tens of milliseconds limited merely by technical constraints, namely the low signal-to-noise ratio. Moreover, a quantitative analysis of feedback cooling, for example a direct measurement of the temperature reduction of the atom and a demonstration of its improved localization, has not yet been performed. These two loose ends are picked up in this work. The high detection efficiency of our new experimental apparatus enables storage times exceeding 1 s compatible with state-of-the-art laser cooling. Moreover, we develop new experimental techniques to quantify the performance of feedback cooling in detail by directly measuring the temperature reduction of the atom and its better localization [52].

1.3 Quantum Dynamics in Cavity QED

The other degree of freedom, in whose dynamics we are interested, is the internal quantum state of the atom-cavity system. Its observation allows to address several fundamental questions, such as: What are the consequences of the quantization of the light field for the dynamics of the coupled system? How can we observe the dynamics of this quantum system knowing that the act of observing it causes inevitably a perturbation of the system? What is the consequence of a dissipative interaction with the environment? How does the system respond to an external driving? Under what circumstances does the system start to behave classically? Can we potentially control the dynamics by means of feedback?

The observation of the dynamics of the internal degrees of freedom of the coupled atom-cavity system is far more challenging than the observation of the atomic motion. The reason is twofold: First, the typical timescales are about three orders of magnitude shorter than the timescales of the radial atomic motion. This reduces the signal dramatically. Second, as we are now dealing with a quantum system, the act of observing it inevitably affects and perturbs the dynamics. To be more precise, in optical cavity QED experiments with neutral atoms, one usually observes the system by monitoring the photons that are emitted from the cavity. Every photon click at the detector causes a quantum jump of the system. As a consequence, the system's state undergoes a quantum trajectory, in which the coherent evolution, described by the Jaynes-Cummings Hamiltonian, is interrupted by unpredictable quantum jumps. The observation of the system acts as an inevitable source of noise, which at the same time perturbs and stimulates the dynamics.

Measurements of time-dependent correlation functions are a powerful tool to reconstruct the dynamics of the system from the noisy photon stream emitted from the cavity. In the past, measurements of second-order intensity correlation functions have been used to analyze the dynamics of an ensemble of atoms [53] or single atoms [19, 54, 55, 56] coupled to a Fabry-Pérot cavity. In contrast to these previous experiments, we explore the dynamics of the system under strong driving. We observe a new dynamical process that has been predicted [57] but not yet observed, namely the coherent exchange of energy between the driving laser and the atom-cavity system. In addition, third-order intensity correlation functions are introduced as a new tool to address questions concerning the dynamics of the multi-photon states, the time symmetry of the emitted photon stream and the influence of multiple photon-detection events on the quantum trajectory of the system [58].

1.4 This Work

This work starts with a brief introduction to the theoretical concepts of cavity QED in Chapter 2. In Chapter 3, the new apparatus will be described in detail. Before continuing our previous lines of research in cavity QED, we describe in Chapter 4 measurements of the higher-order transverse-mode spectrum of the empty Fabry-Pérot cavity. A systematic deviation from the paraxial approximation is observed, which is very well explained by recent theoretical calculations. We confirm a predicted coupling between the orbital and intrinsic (polarization) angular momentum of the circulating modes.

Our experiments regarding the motional dynamics of a single atom in the cavity are described in Chapter 5. The atom is trapped in an intracavity dipole trap. We observe its trajectory by monitoring the transmitted intensity of a near-resonant probe laser. We implement a simple feedback loop to cool the radial motion of the atom. Due to the high detection efficiency of our new setup, feedback cooling works very efficiently increasing the average storage time by a factor 30 to more than 1 s. Moreover, we present temperature measurements and investigate the dynamics of the cooling process. Most of the observations can be explained qualitatively by a simple model stressing the importance of information for the performance of feedback cooling.

The dynamics of the system are also subject of Chapter 6. However, here we shift our attention to the internal degrees of freedom of the atom-cavity system. We present measurements of the time-dependent second- and third-order intensity correlation function to study the quantum dynamics of the coupled atom-cavity system under strong driving. The third-order correlation function also provides additional information about the photon statistics, which is exploited in Chapter 7 to reconstruct the photon-number distribution of the driven atom-cavity system under different driving conditions. We conclude with a summary of this work and an outlook on future directions in Chapter 8.

Bibliography

[1] E. Schrödinger, *Annalen der Physik* **386**, 109 (1926).

[2] S. S. Schweber, *QED and the Men Who Made It*, Princeton University Press (1994).

[3] C. Cohen-Tannoudji, J. Dupont-Roc, and G. Grynberg, *Photons and Atoms*, J. Wiley & Sons (1997).

[4] W. Weisskopf and E. Wigner, *Z. Phys.* **63**, 54 (1930).

[5] H. A. Bethe, *Phys. Rev.* **72**, 339 (1947).

[6] J. Schwinger, *Phys. Rev.* **73**, 416 (1948).

[7] G. Wentzel, *Zeitschrift für Physik A Hadrons and Nuclei* **40**, 574 (1926).

[8] G. Wentzel, *Zeitschrift für Physik A Hadrons and Nuclei* **41**, 828 (1927).

[9] R. K. Nesbet, *Phys. Rev. A* **4**, 259 (1971).

[10] M. D. Crisp and E. T. Jaynes, *Phys. Rev.* **179**, 1253 (1969).

[11] E. T. Jaynes and F. W. Cummings, *Proc. IEEE* **51**, 89 (1963).

[12] G. Rempe, H. Walther, and N. Klein, *Phys. Rev. Lett.* **58**, 353 (1987).

[13] M. Brune, F. Schmidt-Kaler, A. Maali, J. Dreyer, E. Hagley, J.-M. Raimond, and S. Haroche, *Phys. Rev. Lett.* **76**, 1800 (1996).

[14] R. J. Thompson, G. Rempe, and H. J. Kimble, *Phys. Rev. Lett.* **68**, 1132 (1992).

[15] A. Boca, R. Miller, K. M. Birnbaum, A. D. Boozer, J. McKeever, and H. J. Kimble, *Phys. Rev. Lett.* **93**, 233603 (2004).

[16] P. Maunz, T. Puppe, I. Schuster, N. Syassen, P. W. H. Pinkse, and G. Rempe, *Phys. Rev. Lett.* **94**, 033002 (2005).

[17] M. Khudaverdyan, W. Alt, T. Kampschulte, S. Reick, A. Thobe, A. Widera, and D. Meschede, *Phys. Rev. Lett.* **103**, 123006 (2009).

[18] R. Gehr, J. Volz, G. Dubois, T. Steinmetz, Y. Colombe, B. L. Lev, R. Long, J. Estève, and J. Reichel, *Phys. Rev. Lett.* **104**, 203602 (2010).

[19] D. J. Alton, N. P. Stern, Takao, H. Lee, E. Ostby, K. J. Vahala, and H. J. Kimble, *Nature Phys.* **7**, 159 (2011).

[20] J. P. Reithmaier, G. Sęk, A. Löffler, C. Hofmann, S. Kuhn, S. Reitzenstein, L. V. Keldysh, V. D. Kulakovskii, T. L. Reinecke, and A. Forchel, *Nature* **432**, 197 (2004).

[21] E. Peter, P. Senellart, D. Martrou, A. Lemaitre, J. Hours, J. M. Gerard, and J. Bloch, *Phys. Rev. Lett.* **95**, 067401 (2005).

[22] K. Hennessy, A. Badolato, M. Winger, D. Gerace, M. Atatüre, S. Gulde, S. Fält, E. L. Hu, and A. Imamoğlu, *Nature* **445**, 896 (2007).

[23] A. Laucht, F. Hofbauer, N. Hauke, J. Angele, S. Stobbe, M. Kaniber, G. Böhm, P. Lodahl, M.-C. Amann, and J. J. Finley, *New Journal of Physics* **11**, 023034 (2009).

[24] T. Yoshie, A. Scherer, J. Hendrickson, G. Khitrova, H. M. Gibbs, G. Rupper, C. Ell, O. B. Shchekin, and D. G. Deppe, *Nature* **432**, 200 (2004).

[25] A. Wallraff, D. I. Schuster, A. Blais, L. Frunzio, R.-S. Huang, J. Majer, S. Kumar, S. M. Girvin, and R. J. Schoelkopf, *Nature* **431**, 162 (2004).

[26] I. Chiorescu, P. Bertet, K. Semba, Y. Nakamura, C. J. P. M. Harmans, and J. E. Mooij, *Nature* **431**, 159 (2004).

[27] K. B. Cooper, M. Steffen, R. McDermott, R. W. Simmonds, S. Oh, D. A. Hite, D. P. Pappas, and J. M. Martinis, *Phys. Rev. Lett.* **93**, 180401 (2004).

[28] F. Deppe, M. Mariantoni, E. P. Menzel, A. Marx, S. Saito, K. Kakuyanagi, H. Tanaka, T. Meno, K. Semba, H. Takayanagi, E. Solano, and R. Gross, *Nature Phys.* **4**, 686 (2008).

[29] H. Carmichael, *An Open Systems Approach to Quantum Optics*, Springer-Verlag, Berlin (1993).

[30] H. Carmichael, *Statistical Methods in Quantum Optics 2: Non-Classical Fields*, Springer-Verlag, Berlin (2007).

[31] P. Berman, editor, *Cavity Quantum Electrodynamics*, volume 2 of *Advances in Atomic, Molecular, and Optical Physics*, Academic Press (1994).

[32] A. M. Dutra, *Cavity Quantum Electrodynamics: The Strange Theory of Light in a Box*, John Wiley & Sons, Hoboken (2005).

[33] S. Haroche and J. M. Raimond, *Exploring the Quantum: Atoms, Cavities, and Photons*, Oxford University Press (2006).

[34] S. Haroche, Cavity quantum electrodynamics, in *Fundamental Systems in Quantum Optics, Les Houches, Session LIII, 1990*, edited by J. Dalibard, J. M. Raimond, and J. Zinn-Justin, p. 767, Elsevier Science, Amsterdam (1992).

[35] H. Kimble, *Phys. Scr.* **T76**, 127 (1998).

[36] H. Walther, B. T. H. Varcoe, B.-G. Englert, and T. Becker, *Rep. Prog. Phys.* **69**, 1325 (2006).

[37] G. Khitrova, H. M. Gibbs, M. Kira, S. W. Koch, and A. Scherer, *Nature Phys.* **2**, 81 (2006).

[38] R. J. Schoelkopf and S. M. Girvin, *Nature* **451**, 664 (2008).

[39] P. Münstermann, *Dynamik einzelner Atome in einem optischen Resonator höchster Finesse*, PhD thesis, Universität Konstanz (1999).

[40] H. J. Metcalf and P. van der Straten, *Laser Cooling and Trapping*, Springer, New York (1999).

[41] C. J. Hood, M. S. Chapman, T. W. Lynn, and H. J. Kimble, *Phys. Rev. Lett.* **80**, 4157 (1998).

[42] P. Münstermann, T. Fischer, P. W. H. Pinkse, and G. Rempe, *Opt. Comm.* **159**, 63 (1999).

[43] P. Münstermann, T. Fischer, P. Maunz, P. W. H. Pinkse, and G. Rempe, *Phys. Rev. Lett.* **84**, 4068 (2000).

[44] P. W. H. Pinkse, T. Fischer, P. Maunz, and G. Rempe, *Nature* **404**, 365 (2000).

[45] C. J. Hood, T. W. Lynn, A. C. Doherty, A. S. Parkins, and H. J. Kimble, *Science* **287**, 1447 (2000).

[46] T. Fischer, P. Maunz, P. W. H. Pinkse, T. Puppe, and G. Rempe, *Phys. Rev. Lett.* **88**, 163002 (2002).

[47] J. Ye, D. W. Vernooy, and H. J. Kimble, *Phys. Rev. Lett.* **83**, 4987 (1999).

[48] P. Maunz, *Cavity cooling and spectroscopy of a bound atom-cavity system*, PhD thesis, Max-Planck-Institut für Quantenoptik und Technische Universität München (2004).

[49] T. Puppe, I. Schuster, A. Grothe, A. Kubanek, K. Murr, P. W. H. Pinkse, and G. Rempe, *Phys. Rev. Lett.* **99**, 013002 (2007).

[50] P. Maunz, T. Puppe, I. Schuster, N. Syassen, P. W. H. Pinkse, and G. Rempe, *Nature* **428**, 50 (2004).

[51] A. Kubanek, M. Koch, C. Sames, A. Ourjoumtsev, P. W. H. Pinkse, K. Murr, and G. Rempe, *Nature* **462**, 898 (2009).

[52] M. Koch, C. Sames, A. Kubanek, M. Apel, M. Balbach, A. Ourjoumtsev, P. W. H. Pinkse, and G. Rempe, *Phys. Rev. Lett.* **105**, 173003 (2010).

[53] G. Rempe, R. Thompson, H. Kimble, and R. Lalezari, *Opt. Lett.* **17**, 363 (1992).

[54] K. M. Birnbaum, A. Boca, R. Miller, A. D. Boozer, T. E. Northup, and H. J. Kimble, *Nature* **436**, 87 (2005).

[55] A. Kubanek, A. Ourjoumtsev, I. Schuster, M. Koch, P. W. H. Pinkse, K. Murr, and G. Rempe, *Phys. Rev. Lett.* **101**, 203602 (2008).

[56] A. Faraon, I. Fushman, D. Englund, N. Stoltz, P. Petroff, J. Vuckovic, A. Faraon, I. Fushman, D. Englund, N. Stoltz, P. Petroff, and J. Vučković, *Nature Physics* **4**, 859 (2008).

[57] L. Tian and H. Carmichael, *Phys. Rev. A* **46**, R6801 (1992).

[58] M. Koch, C. Sames, M. Balbach, H. Chibani, A. Kubanek, K. Murr, T. Wilk, and G. Rempe, *Phys. Rev. Lett.* **107**, 023601 (2011).

Chapter 2

Cavity Quantum Electrodynamics

Contents

In this chapter, we briefly review some of the theoretical concepts and methods which are needed to understand and analyze the experiments described in thesis. Three different models can be used to describe an atom-cavity system in the strong-coupling regime [1]: First, a purely classical model based on coupled harmonic oscillators. Second, a semi-classical model taking into account the quantization of the atom only. Third, the full quantum model. We only discuss the last one, which describes all the properties of the system under all conditions.

We begin by introducing the Jaynes-Cummings Hamiltonian, which describes the closed atom-cavity system. The model is then extended to include the driving and dissipation. We shortly review the master-equation and quantum-trajectory approach to describe the system theoretically in the presence of dissipation. As these concepts

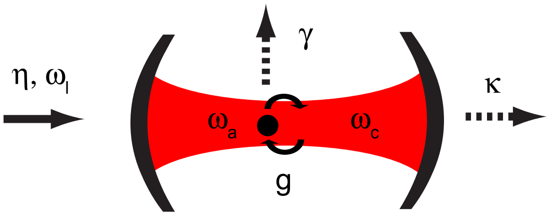

Figure 2.1: Schematic of the atom-cavity system and relevant frequencies and decay rates. A two-level atom (transition frequency ω_a) is coupled to the mode of Fabry-Pérot cavity (resonance frequency ω_c) with the coupling strength g. The cavity field decay and atomic polarization decay rates, corresponding to the half width at half maximum (HWHM) of the respective resonances, are κ and γ, respectively. The system is driven by a probe laser with frequency ω_l and amplitude η. When the empty cavity is driven on resonance, the average photon number in the cavity is η^2/κ^2.

are introduced in depth in several textbooks about cavity QED [2, 3] and quantum optics [4, 5, 6], we only provide a brief review here and omit complicated derivations.

2.1 The Jaynes-Cummings Model

2.1.1 Hamiltonian

A single two-level atom with resonance frequency ω_a is placed in an optical resonator with the resonance frequency ω_c (cf. Fig. 2.1). Treating the light-matter interaction in the dipole approximation and applying the rotating wave approximation, the interaction of the two-level atom (with ground state, $|g\rangle$, and excited state, $|e\rangle$) with the quantized mode of the cavity (with Fock states, $|n\rangle, n \in \mathbb{N}_{\geq 0}$) is described by the Jaynes-Cummings Hamiltonian [7]:

$$H_{jc} = \underbrace{\hbar\omega_a \sigma_+ \sigma_-}_{\text{bare atom}} + \underbrace{\hbar\omega_c a^\dagger a}_{\text{bare cavity}} + \underbrace{\hbar g(a^\dagger \sigma_- + a\sigma_+)}_{\text{dipole coupling}} \tag{2.1}$$

with the following parameters and operators:

- g is the dipole coupling constant, which depends on the atomic dipole transition strength, the mode volume of the cavity and the position of the atom with respect to the cavity mode.
- a and $a^\dagger$ are the annihilation and creation operators for photons in the cavity mode obeying the bosonic commutation relation $[a, a^\dagger]_- = 1$.
- $\sigma_+ = |e\rangle\langle g|$ and $\sigma_- = |g\rangle\langle e|$ are the creation and annihilation operators for an atomic excitation obeying the fermionic commutation relation $[\sigma_-, \sigma_+]_+ = 1$.

2.1.2 The Dressed States

Except for the ground state, $|0, g\rangle$, which is unchanged, the eigenstates of the Jaynes-Cummings Hamiltonian are arranged in doublets, which we call the nth-order dressed states, $|n, \pm\rangle$. Each pair shares the same number of excitations, $\langle n, \pm|(a^\dagger a + \sigma^+\sigma^-)|n, \pm\rangle = n$. The dressed states can be expressed in terms of the bare atom and cavity eigenstates as:

$$|n, +\rangle = \cos\theta|n-1, e\rangle + \sin\theta|n, g\rangle \tag{2.2}$$

$$|n, -\rangle = -\sin\theta|n-1, e\rangle + \cos\theta|n, g\rangle \tag{2.3}$$

with the mixing angle

$$\tan(\theta) = \frac{2g\sqrt{n}}{(\omega_a - \omega_c) + \sqrt{4g^2 n + (\omega_a - \omega_c)^2}}. \tag{2.4}$$

With $\sin(\theta) = \cos(\theta) = \frac{1}{\sqrt{2}}$ when the atom and cavity resonance are degenerate ($\omega_a = \omega_c$). The corresponding eigenvalues (i.e., the resonances of the system) and the splitting of the doublets are

$$E_{n,\pm} = \hbar n \omega_c + \frac{1}{2}\hbar(\omega_a - \omega_c) \pm \frac{1}{2}\hbar\sqrt{4g^2 n + (\omega_a - \omega_c)^2} \tag{2.5}$$

$$E_{n,+} - E_{n,-} = \hbar\sqrt{4g^2 n + (\omega_a - \omega_c)^2} \tag{2.6}$$

If the atom is on resonance with the cavity, the splitting of the dressed states simply increases with the square root of the number of excitations forming the anharmonic Jaynes-Cummings ladder depicted in Fig. 2.2 (a). The eigenenergies of the dressed states can be resolved spectroscopically by monitoring the transmission of a weak probe beam as a function of its frequency [8, 17].

2.1.3 Dynamics

In this work, we are particularly interested in the dynamics invoked by the Jaynes-Cummings Hamiltonian. In this context, the dipole-coupling term has a very intuitive explanation, namely it describes a coherent exchange of excitations between the two-level atom and the mode of the cavity. The frequency at which this exchange happens scales with the square root of the number of excitations in the system. In other words: The photons in the cavity cause a stimulated emission of photons from the atom. Due to the quantization of the intracavity field, the stimulated emission rate, which scales with the square root of the field amplitude, can assume only discrete values. Therefore, it is common to speak of quantum Rabi oscillations [10]. In the case of an empty cavity, the emission of a photon is stimulated by the vacuum giving rise to the vacuum Rabi oscillations at the vacuum Rabi frequency $2g$.

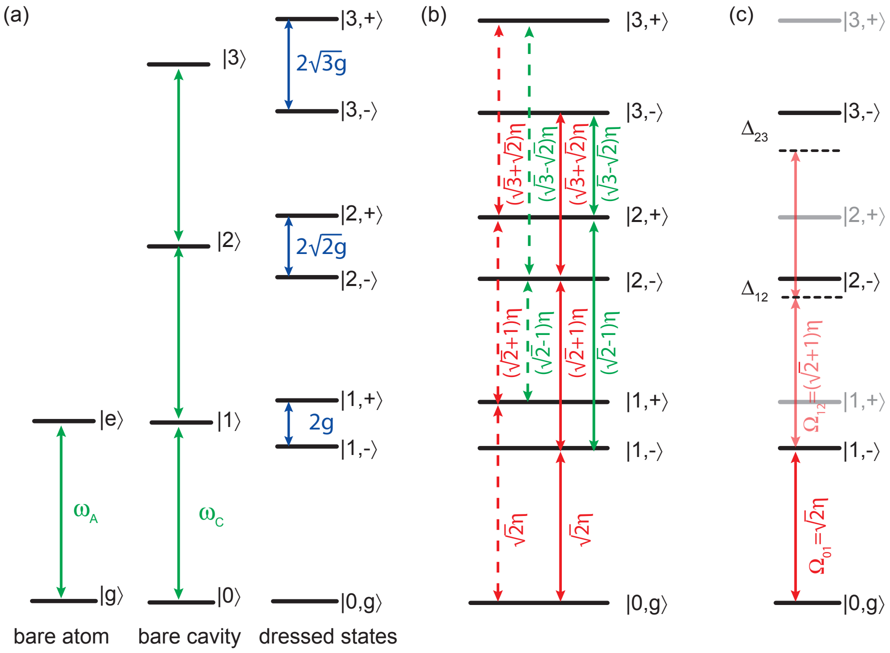

Figure 2.2: (a) Energy levels of the bare atom, the bare cavity and the dressed states of the coupled atom-cavity system. (b) Driving the cavity induces transition between the dressed states. The coupling between adjacent plus or minus states is stronger (red) than coupling between plus and minus states (green). (c) On resonance with one of the normal modes, the system behaves similar to a two-level system as long as the transition to the next dressed states is not driven too strongly.

2.2 Driving

2.2.1 Hamiltonian

To probe the system and to induce dynamics, we drive the system with a near-resonant probe laser with adjustable frequency and power (cf. Fig. 2.1). Driving of the cavity mode by a coherent light source with the frequency ω_l is described by the following time-dependent Hamiltonian [3]:

$$H_d = \hbar\eta(ae^{i\omega_l t} + a^\dagger e^{-i\omega_l t}) \tag{2.7}$$

The driving strength, η, is proportional to the amplitude of the probe laser. The energy of the system is no longer conserved, since photons can be exchanged with the probe laser. This is reflected by the explicit time dependence of the Hamiltonian. For further calculations, it is often convenient to transform the full Hamiltonian, $H_{JC} + H_d$, to a rotating frame eliminating the explicit time dependence. As shown in Appendix A one obtains the transformed Hamiltonian

$$H = \hbar\Delta_a\sigma_+\sigma + \hbar\Delta_c a^\dagger a + \hbar g(a^\dagger\sigma_- + a\sigma_+) + \hbar\eta(a + a^\dagger) \tag{2.8}$$

with the atom detuning, $\Delta_a = \omega_a - \omega_l$, and the cavity detuning, $\Delta_c = \omega_c - \omega_l$.

2.2.2 Driving in the Dressed-State Basis

In Eq. 2.8, the driving was expressed in terms of the bare eigenstates of the system without atom-light interaction. We can also express it in terms of dressed eigenstates, $|n\pm\rangle$, of the coupled system [6]. In this basis, the driving Hamiltonian is

$$\begin{aligned} H_d = \hbar\eta(a+a^\dagger) &= \hbar\eta\sum_{n=0}^{\infty}\left(\sqrt{n+1}|n+1\rangle\langle n| + h.c.\right)\otimes\left(|g\rangle\langle g| + |e\rangle\langle e|\right) \\ &= \hbar\eta(\sum_{n=1}^{\infty}\frac{\sqrt{n}+\sqrt{n+1}}{2}|n+1,+\rangle\langle n,+| + \frac{\sqrt{2}}{2}|1,+\rangle\langle 0,g| \\ &+ \sum_{n=1}^{\infty}\frac{\sqrt{n}+\sqrt{n+1}}{2}|n+1,-\rangle\langle n,-| + \frac{\sqrt{2}}{2}|1,-\rangle\langle 0,g| \\ &+ \sum_{n=1}^{\infty}\frac{\sqrt{n+1}-\sqrt{n}}{2}|n+1,-\rangle\langle n,+| + \sum_{n=1}^{\infty}\frac{\sqrt{n+1}-\sqrt{n}}{2}|n+1,+\rangle\langle n,-| + h.c.). \end{aligned} \tag{2.9}$$

The meaning of this complicated expression becomes much clearer when we consider the diagrammatic representation in Fig. 2.2 (b). First, we note that the coupling between plus and minus states is much weaker because of the minus sign in the coupling terms $(\sqrt{n+1}-\sqrt{n})$. It is often reasonable to neglect this coupling. With this approximation, we find two anharmonic energy ladders. The coupling of adjacent energy levels in each of the ladders has two consequences: The probe laser causes transitions between the dressed states and thus alters the dynamics of the system. Moreover, the coupling causes shifts of the dressed energy levels, which, in some cases, can be treated perturbatively. We will encounter both effects in Chapter 6 where we study the dynamics of the atom-cavity system experimentally.

2.2.3 Dynamics

One particularly interesting situation is depicted in Fig. 2.2 (c). When the probe laser is on resonance or close to resonance with the normal modes, it is detuned from the higher-order dressed states because of the anharmonicity of the Jaynes-Cummings ladder. One consequence is that photons can enter the cavity only one-by-one resulting in what has been called a photon blockade [11]. In terms of the dynamics, the system is expected to behave like a driven two-level system showing Rabi-like oscillations between the ground state and the normal mode [12] due to the coherent exchange of energy between the probe laser and the atom-cavity system. For a time resolved observation, the corresponding Rabi frequency of $\Omega_{01} = \sqrt{2}\eta$ must be larger than the dissipation rates of the system. In analogy to the strong-coupling regime, we refer to this as the strong-driving regime of cavity QED. It has only been accessed in some very recent experiments [13, 14]. The resulting dynamics has not yet been studied. If the driving strength is increased even further, one has to take into account transitions to the next dressed state, $|2,-\rangle$. The system then starts to behave like a driven anharmonic oscillator and deviations from the two-level approximation are expected [15]. We refer to the resulting coherent exchange of energy between the atom-cavity system and the driving laser as super Rabi oscillations.

2.3 Dissipation

The strong-coupling condition implies that the coherent internal dynamics of the atom-cavity system dominates over the dissipative interaction with the environment, which gives rise to spontaneous emission of photons from the atom or the cavity (cf. Fig. 2.1). Nevertheless, any attempt to describe the system quantitatively needs to take these dissipative processes into account. In the following, we will shortly review two common approaches to treat the dynamics of the atom-cavity system in the presence of dissipation.

In the first approach, the Schrödinger equation is expanded to include the environment consisting of the modes of the electro-magnetic field which couple to the excited atom (causing spontaneous emission) and to the cavity mode (causing cavity decay). By eliminating these additional degrees of freedom from the combined, complicated Schrödinger equation, a differential equation (the master equation) for the density matrix of the atom-cavity system can be derived.

In the second approach, the occurrence of quantum jumps, due to spontaneous emission and cavity decay, is incorporated into the Schrödinger equation in a phenomenological way. We obtain a stochastic quantum trajectory of the state of the atom-cavity system. Experimentally accessible observables can be determined by averaging over many such quantum trajectories.

2.3.1 Master Equation

The description of dissipative quantum systems by means of a master equation is a standard technique in quantum optics, which is discussed in many text books (e.g., [16]). In the following, we present a summary of the derivation based on [4]. In addition to the system Hamiltonian, H_S, we introduce a Hamiltonian modeling the environment as a reservoir of harmonic oscillators (described by a Hamiltonian, H_R). In our case, these harmonic oscillators represent the continuum of modes of the quantized electromagnetic field to which the cavity and the atom can emit photons. The interaction of this reservoir with the system, with the coupling Hamiltonian, H_RS, is assumed to be linear in the system and the bath operator [3]. The system plus the reservoir can be described by a density matrix, $\rho_\mathrm{RS}(t)$, whose time evolution is governed by the Schödinger equation

$$\dot{\rho}_\mathrm{RS} = \frac{1}{i\hbar}[H_\mathrm{S} + H_\mathrm{R} + H_\mathrm{RS}, \rho_\mathrm{RS}]. \tag{2.10}$$

We are interested in the system's dynamics only. Its density matrix is obtained by performing a partial trace over the eigenstates of the reservoir.

$$\rho(t) = \mathrm{tr}_\mathrm{R}\left(\rho_\mathrm{RS}(t)\right). \tag{2.11}$$

A relatively simple equation of motion for the reduced density matrix can be derived from 2.10 making two important approximations: First, the Born approximation neglecting second- and higher-order terms of the system-reservoir interaction, H_RS. Second, the Markoff approximation assuming that the future evolution of $\rho(t)$ depends only on its current and not its past values.

With these approximations one finds a Lindblad master equation for the density matrix. Most generally, it includes thermal excitations of the reservoir. However, as we are dealing with optical frequencies, these can be neglected at room temperature. The master equation then reads:

$$\dot{\rho} = \frac{1}{i\hbar}[H_S, \rho] + \underbrace{\kappa(2a\rho a^\dagger - a^\dagger a\rho - \rho a^\dagger a)}_{\text{cavity decay}} + \underbrace{\gamma(2\sigma_-\rho\sigma_+ - \sigma_+\sigma_-\rho - \rho\sigma_+\sigma_-)}_{\text{spontanteous emission}} \tag{2.12}$$

It involves three terms: the first term describes the coherent evolution of the driven atom-cavity system discussed before, the second-term takes into account the cavity decay, and the third term describes the spontaneous emission of the atom.

2.3.2 Solving the Master Equation

The master equation 2.12 can formally be expressed in terms of a Lindblad operator, $\mathcal{L}$:

$$\dot{\rho} = \mathcal{L}\rho \tag{2.13}$$

It can be solved numerically by truncating the Hilbert space of the cavity mode at some finite photon number. After diagonalizing the truncated master equation, the time-dependent density matrix can be expressed as an exponential series of the eigenvalues of the Lindblad operator (cf. e.g., [17]). We use the quantum optics toolbox for Matlab, written by Sze Tan [18], to carry out these steps. In the following, we will use the notation

$$\rho(t) = e^{\mathcal{L}t}\rho(0) \tag{2.14}$$

to denote a formal solution to the master equation. The time dependence of the expectation value of some arbitrary operator, $\hat{O}$, can now be written down as

$$\langle\hat{O}(t)\rangle = \mathrm{tr}(\hat{O}e^{\mathcal{L}t}\rho(0)). \tag{2.15}$$

In analogy to a classical driven damped harmonic oscillator, one finds a relaxation of the system to a steady state on a timescale determined by the dissipative processes. The steady-state density matrix is

$$\mathcal{L}\rho_\mathrm{s} = 0. \tag{2.16}$$

As a consequence, the time-averaged expectation value of any observable, $\hat{O}$, is given steady-state expectation value, $\langle\hat{O}\rangle = \mathrm{tr}(\hat{O}\rho_\mathrm{s})$. Experiments that probe time-averaged properties of the system, such as the average transmission through the cavity [8, 17, 19] or the probability of the system to emit two photons simultaneously [20, 21], are fully described by evaluating steady-state expectation values.

2.3.3 The Quantum Regression Theorem

The analysis of multi-time correlation functions is a powerful tool to observe the dynamics of the system. In this work, we characterize the photon stream that is emitted from the cavity by means of photon counting techniques. We measure the probability to detect n-photons with time separations, $\tau_1 \ldots \tau_{n-1}$. According to the standard quantum theory of photoelectric detection [22], this probability is proportional to time and normally ordered intensity correlation functions [23] of the form

$$\gamma_k(\tau_1 \ldots \tau_{\text{k-1}}) = \langle a^\dagger a^\dagger(\tau_1) \ldots a^\dagger(\tau_1 + \ldots + \tau_{k-1}) a(\tau_1 + \ldots + \tau_{k-1}) \ldots a(\tau_1) a \rangle. \qquad (2.17)$$

The quantum regression theorem, first put forward by Lax [24], enables us to calculate arbitrary correlation functions based on the solution of the master equation obtained in the last paragraph. At the same time, it provides a relatively simple interpretation of the physical meaning of the correlation function. We will skip the derivation of the quantum regression theorem, which can be found in [4], but we only state the results. The second-order intensity correlation function can be written as

$$\langle a^\dagger a^\dagger(\tau) a(\tau) a \rangle = \operatorname{tr}\left\{ a^\dagger a e^{\mathcal{L}\tau} \left[a \rho_{\text{s}} a^\dagger \right] \right\} \qquad (2.18)$$

where the term $e^{\mathcal{L}\tau}\left[a\rho_{\text{s}}a^\dagger\right]$ refers to the time evolution (governed by the master equation) of the initial density matrix, $a\rho_{\text{s}}a^\dagger$ (cf. Eq. 2.14). This directly suggests the following interpretation of the time-dependent second-order correlation function: Before the detection of the first photon, the system is described by the steady-state density matrix, ρ_{s}. The detection, that is the annihilation of a photon, causes a projection of ρ_{s} onto the new density matrix, $a\rho_{\text{s}}a^\dagger$. Except for some constant normalization factor, the time-dependent second-order correlation function then reflects the time evolution of the average photon number, $\langle a^\dagger a \rangle$, back to its steady-state expectation value.

Similar arguments can be applied to the third-order correlation function

$$\langle a^\dagger a^\dagger(\tau_1) a^\dagger(\tau_1 + \tau_2) a(\tau_1 + \tau_2) a(\tau_1) a \rangle = \operatorname{tr}\left\{ a^\dagger a e^{\mathcal{L}\tau_2} \left[a e^{\mathcal{L}\tau_1} \left[a \rho_{\text{s}} a^\dagger \right] a^\dagger \right] \right\}. \qquad (2.19)$$

The system starts in the steady state, ρ_{s}. The detection of a photon causes a projection onto $a\rho_{\text{s}}a^\dagger$. The system evolves according to the master equation, $e^{\mathcal{L}\tau}\left[a\rho_{\text{s}}a^\dagger\right]$. Then, the detection of a second photon after the time τ_1 causes another projection onto $a e^{\mathcal{L}\tau_1}\left[a\rho_{\text{s}}a^\dagger\right] a^\dagger$. This density matrix also evolves according to the master equation. The probability to detect a third-photon at the time τ_2 later then reflects the evolution of the average photon number back to the steady state.

2.3.4 Quantum Trajectories

From our previous discussion, one could naively conclude that the state of the system undergoes a deterministic time evolution described by the master equation. This seems to be at odds with the standard probabilistic interpretation of quantum mechanics, which predicts the occurrence of probabilistic quantum jumps caused by measurements (e.g., the detection of a photon) performed on the system. The solution to this apparent dilemma is that the mixed density matrix appearing in the master equation always incorporates an ensemble average over different probabilistic trajectories of the system.

In principle, we can also calculate these probabilistic trajectories of the system's state. This is the approach followed by quantum trajectory (also called quantum Monte-Carlo) simulations. They have been introduced independently by Mølmer et al. [25]

and Carmichael [16]. Their basic idea is to calculate the deterministic time evolution of the pure state of the driven, closed atom-cavity system by numerically integrating the Schrödinger equation with the Hamiltonian $H = H_{\text{JC}} + H_{\text{d}}$. Dissipation is then introduced in a phenomenological way by allowing at each integration step for probabilistic quantum jumps associated with the spontaneous emission of a photon from the atom or the cavity.

To be more concrete, we consider the atom cavity system without dissipation first. Assuming that the system is in the state $|\Psi(t)\rangle$ at time t. The unnormalized state at a short time, Δt, later is given by

$$|\Psi(t+\Delta t)\rangle = (1 - i\frac{H\Delta t}{\hbar})|\Psi(t)\rangle \tag{2.20}$$

where H is the full Hamiltonian of the system including atom-cavity coupling and driving. The Schrödinger equation can be integrated numerically by iterating this step many times. Dissipation is included by allowing at each time step for the spontaneous emission of a photon from the atom or the cavity. The probabilities for these two events are $p_\sigma = 2\gamma\Delta t\langle\Psi(t)|\sigma_+\sigma_-|\Psi(t)\rangle$ and $p_a = 2\kappa\Delta t\langle\Psi(t)|a^\dagger a|\Psi(t)\rangle$, respectively. Whether such an event occurs is determined by chance. In conclusion, the state is propagated in time according to the following rules:

$$|\Psi(t+\Delta t)\rangle = \begin{cases} \sigma_-|\Psi(t)\rangle & \text{with probability } p_\sigma \\ a|\Psi(t)\rangle & \text{with probability } p_a \\ (1 - i\frac{H'\Delta t}{\hbar})|\Psi(t)\rangle & \text{otherwise} \end{cases} \tag{2.21}$$

As it turns out, a non-detection event also provides some information about the systems state. Therefore, a modified non-Hermitian Hamiltonian H' has to be used (cf. [25] and references therein):

$$H' = H - \frac{i\hbar\gamma}{2}\sigma_+\sigma_- - \frac{i\hbar\kappa}{2}a^\dagger a \tag{2.22}$$

We thus obtain a non-deterministic quantum trajectory of the wave function, which can be used to evaluate the time evolution of arbitrary expectation values.

For pedagogical reasons, it is often instructive to analyze and discuss individual trajectories. However, for a quantitative comparison with the experiment one has to rely on ensemble averages over many trajectories, which, in the limit of a very large number of trajectories, give equivalent results to the master equation approach. As the latter is not sensitive to statistical fluctuations, it is usually the method of choice. However, since it relies on the density matrix, whose size increases with the square of the dimensions of the Hilbert space, it scales less favorable with an increasing size of the Hilbert space. Therefore, for calculations with large driving strengths, where a large number of Fock states has to be taken into account, it can be advantageous to use quantum trajectory calculations.

As for the numerical solutions of the master equation, we use the routines implemented in the quantum optics toolbox [18] to calculate quantum trajectories of the atom-cavity system.

Bibliography

[1] I. Schuster, *Nonlinear spectroscopy of a single-atom-cavity system*, PhD thesis, Technische Universität München (2008).

[2] P. Berman, editor, *Cavity Quantum Electrodynamics*, volume 2 of *Advances in Atomic, Molecular, and Optical Physics*, Academic Press (1994).

[3] A. M. Dutra, *Cavity Quantum Electrodynamics: The Strange Theory of Light in a Box*, John Wiley & Sons, Hoboken (2005).

[4] H. Carmichael, R. Brecha, and P. Rice, *Opt. Comm.* **82**, 73 (1991).

[5] D. F. Walls and G. J. Milburn, *Quantum Optics*, Springer, Berlin (1994).

[6] H. Carmichael, *Statistical Methods in Quantum Optics 2: Non-Classical Fields*, Springer-Verlag, Berlin (2007).

[7] E. T. Jaynes and F. W. Cummings, *Proc. IEEE* **51**, 89 (1963).

[8] P. Maunz, T. Puppe, I. Schuster, N. Syassen, P. W. H. Pinkse, and G. Rempe, *Phys. Rev. Lett.* **94**, 033002 (2005).

[9] D. I. Schuster, A. A. Houck, J. A. Schreier, A. Wallraff, J. M. Gambetta, A. Blais, L. Frunzio, J. Majer, B. Johnson, M. H. Devoret, S. M. Girvin, and R. J. Schoelkopf, *Nature* **445**, 515 (2007).

[10] M. Brune, F. Schmidt-Kaler, A. Maali, J. Dreyer, E. Hagley, J.-M. Raimond, and S. Haroche, *Phys. Rev. Lett.* **76**, 1800 (1996).

[11] K. M. Birnbaum, A. Boca, R. Miller, A. D. Boozer, T. E. Northup, and H. J. Kimble, *Nature* **436**, 87 (2005).

[12] L. Tian and H. Carmichael, *Phys. Rev. A* **46**, R6801 (1992).

[13] L. S. Bishop, J. M. Chow, J. Koch, A. A. Houck, M. H. Devoret, E. Thuneberg, S. M. Girvin, and R. J. Schoelkopf, *Nature Phys.* **5**, 105 (2009).

[14] M. A. Armen, A. E. Miller, and H. Mabuchi, *Phys. Rev. Lett.* **103**, 173601 (2009).

[15] J. Claudon, A. Zazunov, F. W. J. Hekking, and O. Buisson, *Phys. Rev. B* **78**, 184503 (2008).

[16] H. Carmichael, *An Open Systems Approach to Quantum Optics*, Springer-Verlag, Berlin (1993).

[17] I. Schuster, A. Kubanek, A. Fuhrmanek, T. Puppe, P. W. H. Pinkse, K. Murr, and G. Rempe, *Nature Phys.* **4**, 382 (2008).

[18] S. M. Tan, *Journal of Optics B: Quantum and Semiclassical Optics* **1**, 424 (1999).

[19] A. Boca, R. Miller, K. M. Birnbaum, A. D. Boozer, J. McKeever, and H. J. Kimble, *Phys. Rev. Lett.* **93**, 233603 (2004).

[20] A. Kubanek, A. Ourjoumtsev, I. Schuster, M. Koch, P. W. H. Pinkse, K. Murr, and G. Rempe, *Phys. Rev. Lett.* **101**, 203602 (2008).

[21] A. Faraon, I. Fushman, D. Englund, N. Stoltz, P. Petroff, J. Vuckovic, A. Faraon, I. Fushman, D. Englund, N. Stoltz, P. Petroff, and J. Vučković, *Nature Physics* **4**, 859 (2008).

[22] L. Mandel and E. Wolf, *Optical coherence and quantum optics*, Cambridge University Press (1995).

[23] R. J. Glauber, *Phys. Rev. Lett.* **10**, 84 (1963).

[24] M. Lax, *Phys. Rev.* **129**, 2342 (1963).
[25] K. Molmer, Y. Castin, and J. Dalibard, *J. Opt. Soc. Am. B* **10**, 524 (1993).

Chapter 3

Experimental Setup

Contents

In the course of this thesis, a new experimental apparatus to achieve strong coupling between individual rubidium atoms and a high-finesse optical Fabry-Pérot cavity has been planned and set up. The main improvements compared to the predecessor experiment [1] are the length adjustability of the cavity, a higher detection efficiency and better optical access. It is the aim of this chapter to describe and characterize the main

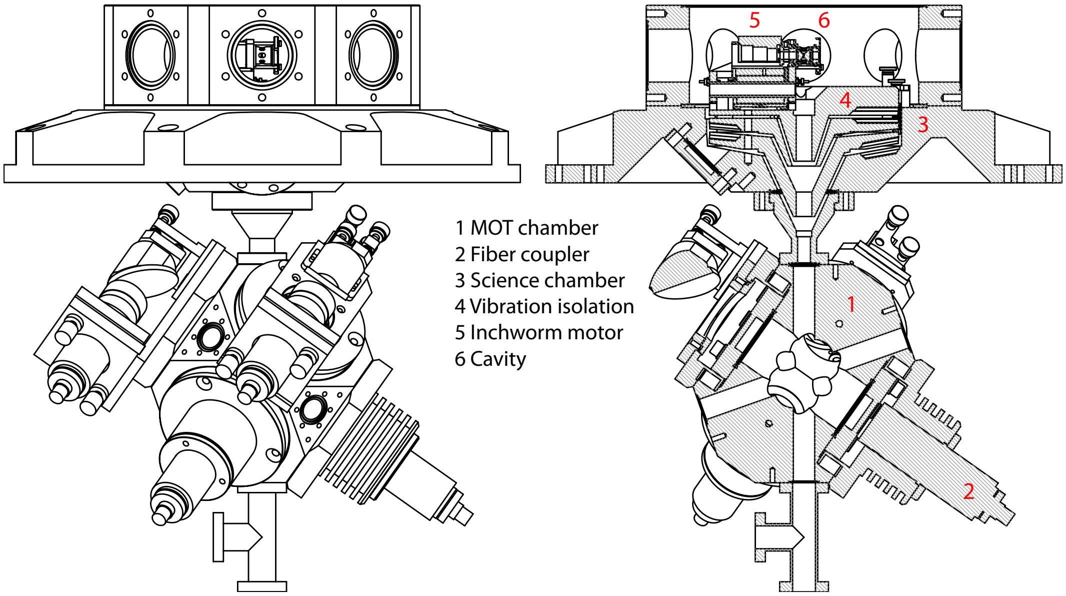

Figure 3.1: Overview of the vacuum chamber. Vacuum pumps and viewports are omitted for clarity. Atoms are first loaded in a fiber-coupled MOT in the lower chamber (1) and then transferred to the upper science chamber (3) by means of an atomic fountain. A cut through the chamber reveals the cavity (6), the inchworm motor (5) for the length adjustment of the cavity and the vibration isolation system (4).

components of the experimental setup. We will start our discussion with an overview of the vacuum chamber. Then, we will describe the magneto-optical trap (MOT) and the atomic fountain, which are used to inject ultra-cold atoms into the cavity. Successively, the cavity is introduced, we characterize the mirrors, and we describe the length adjustability and the passive and active length stabilization of the cavity. We conclude with a summary of the detection setup and the experimental control.

3.1 Vacuum System

As shown in Fig. 3.1, the vacuum system consists of two main parts. The upper science chamber, in which the cavity is installed, has the shape of a horizontally oriented octagon with eight CF-40 flanges on the sides. It houses the cavity mount and the vibration isolation system. Viewports provide optical access along as well as perpendicular to the cavity axis. Moreover, a large sunk-in CF-150 viewport above the cavity allows for optical access with a high-numerical aperture. A titan-sublimation pump, an all-metal valve, an ion gauge (UHV-25p, Varian) and a 55 l/s ion-getter pump (Mecca 2000) are also connected to the main vacuum chamber but are not shown in the figure.

The MOT chamber, a cube with CF-40 flanges at the faces and CF-16 flanges at each of the eight corners, is installed underneath the main chamber. Viewports, connected to the CF-40 flanges, provide the optical access required for the six collimated MOT beams that are irradiated via optical fibers (cf. Section 3.2.2). Two rubidium dispensers (SAES getters) are installed in two opposite corners of the MOT cube. At the bottom of the cube, a T-piece connects the cube to an all-metal valve and an 8 l/s ion-getter pump (Varian).

All vacuum components are made of non-magnetic VA4 steel. The viewports are broadband anti-reflection coated and have a non-magnetic seal. The ion-getter pumps are oriented to minimize the magnetic-field gradients at the position of the MOT and the cavity.

The vacuum system was baked out in three steps. First, the empty upper and lower chamber were baked out separately for one week at 350 °C. During this period, the magnets were removed from the ion-getter pumps and blind flanges were installed instead of the viewports. After installing the magnets and viewports, another bakeout at 200 °C with a duration of one week was performed. The rubidium dispensers were activated, and the titan-sublimator was flashed for the first time. A pressure of $3 \cdot 10^{-11}$ mbar was measured after cool down. Finally, the vibration isolation system and the cavity were installed, and the two chambers were connected. After another bakeout at 140 $°C$ for two weeks, we achieve a pressure of $1 \cdot 10^{-9}$ mbar before and $3 \cdot 10^{-10}$ mbar after flashing the titan-sublimation pump.

A 1 m^2 breadboard is installed on rigid steel pillars on a level with the science chamber to carry the optical components needed to couple light into the cavity and detect the transmitted light (cf. Section 3.4.2 and 3.5). Six large square coils (60 windings, edge length 1 m), forming three Helmholtz pairs, are installed symmetrically around the vacuum chamber to compensate the earth magnetic field.

3.2 Atomic Fountain

We load atoms in the cavity by means of an atomic fountain as it has been described in [2]. Compared to almost deterministic loading schemes via a transverse optical dipole trap [3, 4, 5], this scheme does not require transverse optical access to the cavity and can therefore also be applied to very short cavity lengths. Moreover, it allows for experiments with atoms passing through the cavity mode at a well-defined velocity. The main difference with respect to the forerunner experiment [2] is the use of a fiber-coupled MOT [6] making our setup very robust and simplifying the alignment. In addition, the frequency difference of the upper and lower beams is controlled by a home-made direct digital synthesizer (DDS) [7] improving the reproducibility of the fountain and eliminating problems due to thermal drifts and the limited accuracy of the voltage controlled oscillators (VCOs) previously employed.

3.2.1 Laser System

The operation of a rubidium MOT and an atomic fountain requires two lasers running on two different hyperfine transitions of the D_2 line of ^{85}Rb as depicted in Fig. 3.2. The atoms are laser-cooled on the F=3 to F'=4 transition by the so-called cooling laser. As this closed transition is also used for the cavity QED experiments, the very same laser can be used as a probe laser to drive the atom-cavity system. To compensate for off-resonant scattering to the dark F=2 hyperfine ground state, a repumping laser on

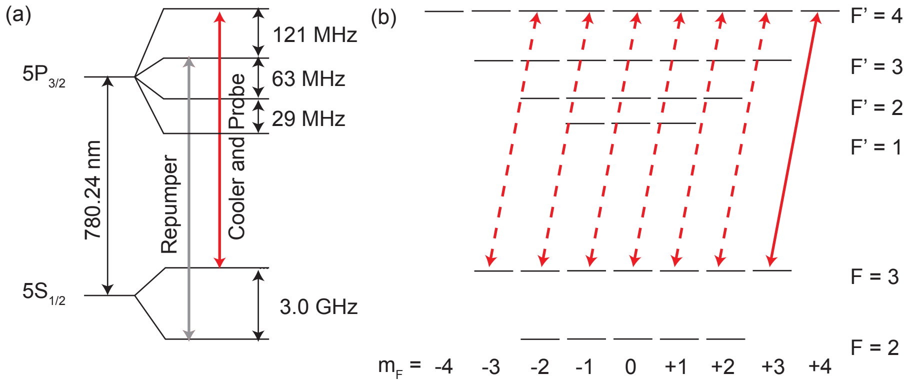

Figure 3.2: (a) Relevant hyperfine transitions of the D2 line of ^{85}Rb. For the operation of the magneto-optical trap, two lasers, a cooler and a repumper, are needed. (b) In the cavity, the probe laser drives the closed $F = 3, m_F = +3$ to $F = 4, m_F = +4$ transition justifying the two-level approximation for the atom.

resonance with the $F{=}2$ to $F'{=}3$ transition of the D_2 line is needed for the operation of the MOT. A brief overview of the laser system will be given in the following. Further details can be found in [8].

Cooling and Probe Laser

The optical setup of the cooling and probe laser is shown in Fig. 3.3 (a). The light is generated by a commercial tapered amplifier seeded by a grating-stabilized diode laser (TA100, Toptica) that provides several hundred milliwatts of power at a wavelength of 780 nm.

A small part of the power of the seeding laser is extracted to stabilize the frequency of the laser with respect to a rubidium transition using the Pound-Drever-Hall (PDH) locking technique [9]. This light passes through a double-pass acousto-optic modulator (AOM) operating at 85 MHz and an electro-optical-modulator (EOM) modulating the phase at a frequency of 8 MHz. The Doppler-free spectroscopy signal from a rubidium vapor cell is then demodulated to obtain a dispersive error signal, which is fed back via a proportional-integral-derivative (PID) controller to the optical-feedback grating of the seeding laser as well as to its current.

We lock the laser to the crossover line of the $F{=}3$ to $F'{=}3/4$ transition. In total, including the detuning of the crossover resonance and the double-pass AOM, the main output of the tapered amplifier is thus red-detuned by 230 MHz with respect to the $F{=}3$ to $F'{=}4$ transition. It is split into three parts. The first two parts are used for the three upper and lower beams of the MOT, whose frequencies have to be tunable separately for the atomic fountain. To this end, each of the beams passes through an AOM in a double-pass configuration used to tune the frequency and to stabilize the intensity of the respective beams. Afterwards, the two beams are coupled into optical fibers. They are connected to the fiber-port clusters, which will be described in the next section, distributing the light equally among the six MOT beams. The third beam, generated from the main output of the laser, also passes through a double-pass AOM. It is then

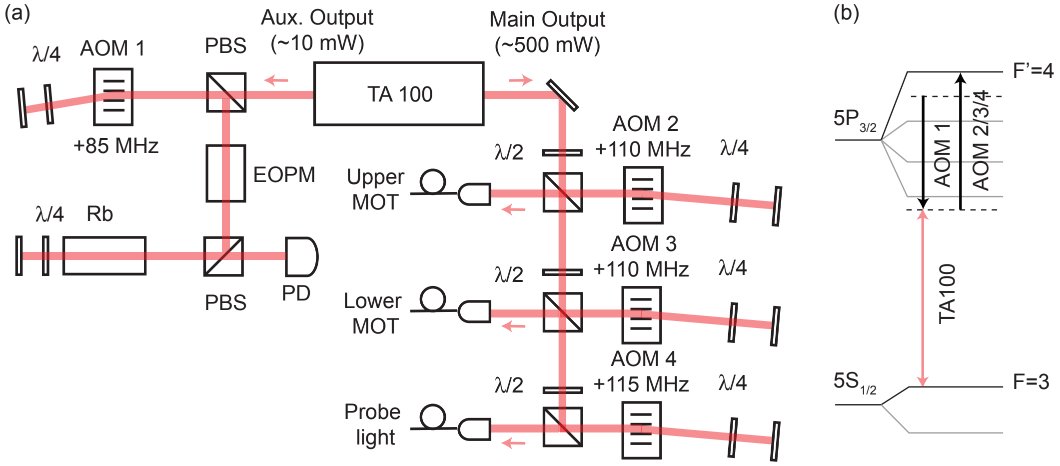

Figure 3.3: (a) Optical setup of the cooling and probe laser. The auxillary output (left part of the figure) of the tapered amplifier laser system (TA100) is used to stabilize the frequency of the laser to a crossover line of a Doppler-free rubidium spectroscopy (cf. text for details). The main output of the tapered amplifier (right-hand side) is divided into three parts. Two parts provide the light for the upper and lower beams of the MOT, whose frequencies can be tuned independently to allow for an atomic fountain. The last part is the probe light that drives the atom-cavity system. All three beams are coupled into optical fibers to deliver the light to the respective parts of the experiment. (b) The laser is locked to a Rb crossover resonance. Because of the detuning of the crossover resonance of 60 MHz and an additional shift of 170 MHz due to the passage through AOM 1 in a double-pass configuration, the output of the laser is red-detuned by 230 MHz with respect to the F=3 to F'=4 transition of the D2 line of ^{85}Rb. Three AOMs in double-pass configuration (AOM 2, 3, 4) shift the MOT and probe light back on, or close to, resonance.

coupled into a polarization-maintaining single-mode fiber delivering the light to the main experimental setup, where it is used to probe the atom-cavity system.

Repumping Laser

For the repumping, another grating-stabilized diode laser (DL100, Toptica) is locked to the crossover resonance of the F=2 to F'=2/3 transition of a rubidium spectroscopy via a Pound-Drever-Hall locking scheme. The optical setup is shown in Fig. 3.4 (a). The detuning of the crossover resonance and an additional shift by an AOM in a double-pass configuration (AOM 1) causes an effective detuning of the output of the laser of 192 MHz with respect to the desired atomic transition. A second AOM in a double-pass configuration (AOM 2) shifts the frequency by this amount and allows to adjust the power. The light is then split into two parts. Most of the power is superimposed with the MOT beams in one of the fiber-port cluster described below. A small fraction of the repumping light (typically a few μW) is coupled into a second fiber whose output is focused onto the cavity from a direction perpendicular to the cavity axis. It serves

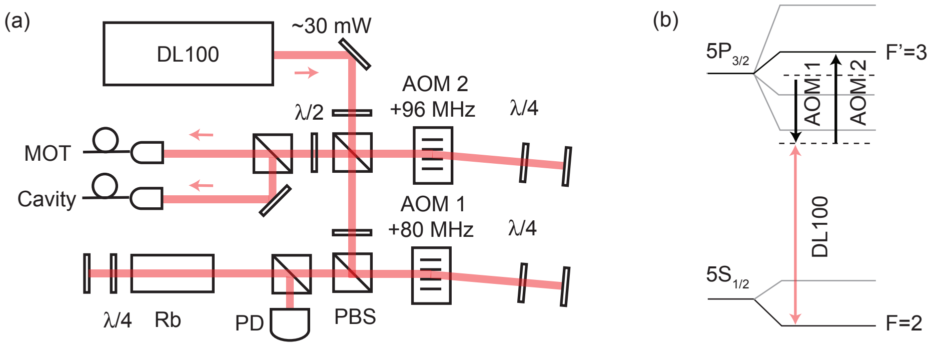

Figure 3.4: (a) The repumping light is generated by a commercial diode laser system (DL100). The light is split in two parts. After passage through an AOM in a double-pass configuration (AOM 1) the first part is directed to a Doppler-free spectroscopy, which is used to stabilize the laser to the F=2 to F'=2/3 crossover resonance. The other part of the light is shifted to the desired F=2 to F'=3 transition by means of another double-pass AOM. Then, it is coupled into two fibers guiding the light to the magneto-optical trap and the cavity . (b) Relevant transitions in rubidium.

as a repumper for the atoms in the intracavity dipole trap.

3.2.2 Fiber-Coupled Magneto-Optical Trap

The fiber-coupled MOT and fountain that we use is similar to what has been described in [6]. The light for the upper and lower MOT beams is coupled into two single-mode polarization-maintaining fibers that are connected to two fiber-port clusters shown in Fig. 3.5 (Schäfter-Kirchhoff). Each of them distributes the power equally among three fibers guiding the light to the vacuum chamber. In addition, a small fraction of the light is directed onto a photo-diode built into the fiber-port cluster to stabilize the intensity. One of the fiber-port clusters has an additional input port that is used to introduce the repumping light.

The six outgoing fibers are connected to fiber couplers with built-in quarter-wave plates that collimate the light to a waist of 12 mm. The three lower fiber couplers are fixed to the vacuum chambers. The upper couplers are installed in adjustable mounts. The light coming from these couplers is reflected from silver mirrors (to maintain the circular polarization) through the viewports of the vacuum chamber (cf. Fig. 3.1). We align the beams by coupling light from the upper beams into the lower fiber couplers.

Two coils in an anti-Helmholtz configuration are incorporated in two opposing fiber coupler mounts. Each coil has 100 windings with an average radius of 4 cm. To ensure good thermal conductivity, these mounts are made of copper and they are equipped with cooling fins. The coils are separated by 10.5 cm and create a magnetic field gradient of 2.5 $\frac{\mathrm{G}}{\mathrm{cmA}}$ along the axis of the coils.

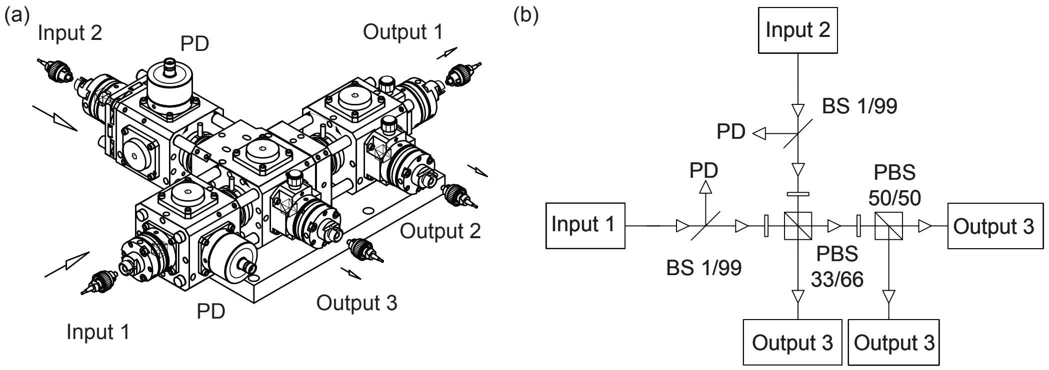

Figure 3.5: Technical (a) and schematic (b) drawing of the fiber-port cluster used to distribute the cooling (Input 1) and repumping (Input 2) light to three fibers. Photodiodes (PD) allow to monitor and stabilizes the light intensity. All input and output ports are connected to polarization-maintaining fibers (drawings courtesy of Schäfter-Kirchhoff).

3.2.3 Experimental Sequence

Launching a cloud of ultra-cold atoms towards the cavity requires three steps: collection of cold atoms in a magneto-optical trap, molasses cooling and finally the atomic fountain.

In the first step, the magneto-optical trap is loaded. During the loading phase a current of 2.9 – 3.0 A runs through one of the dispensers to set free rubidium vapor. A current of 4 A in the MOT coils causes a magnetic field gradient of 10 G/cm along the coil axis. The total power of the cooling light is set to 60 mW red-detuned by 14 MHz with respect to the atomic transition. In addition, we shine in 4 mW of repumping light.

After loading the MOT for 1-1.5 s depending on the desired number of atoms, we start the molasses phase by ramping up the detuning of the cooling light to 42 MHz within 50 ms. In parallel, we decrease the power to 5 mW. At the end of the ramp, the magnetic coils are switched off. After 5 ms of molasses cooling, a temperature of about 4 μK is achieved as we determine from a time of flight measurement (cf. Fig. 3.6 (a) and (b)). We adjust the current through the compensation coils to minimize the temperature after the molasses.

Finally, we launch the fountain by detuning the upper beams with respect to the lower beams within 5 ms. To accelerate all of the atoms, the power of the beams has to be reraised to 18 mW. This causes an increase of the temperature to about 14 μK (cf. Fig. 3.6 (b)). The velocity of the atoms at the cavity can be adjusted by changing the final detuning. We determine the center of mass velocity as a function of the detuning via a time-of-flight measurement. The results are plotted in Fig. 3.6 (c) showing nicely the expected linear dependence of the velocity upon the detuning.

For a detuning of -3 MHz, the turning point of the trajectory of the atomic cloud is approximately located on the cavity axis. The atomic cloud can be detected in the cavity by monitoring the transmission of a resonant probe laser through the cavity. By adjusting the horizontal magnetic field during the acceleration phase, the horizontal

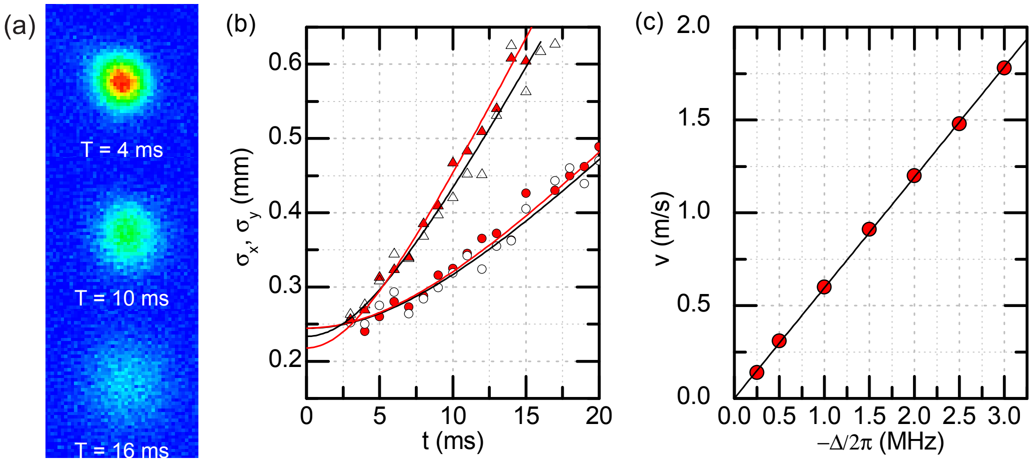

Figure 3.6: (a) Time-of-flight fluorescence image of the expanding atom cloud after the optical molasses. (b) The temperature is extracted from the time dependence of the expansion of the cloud ($\sigma(t) = \sqrt{\sigma_0 + \frac{k_B T t^2}{m}}$). We obtain temperature of $4 \pm 1\ \mu$K after the molasses (○ horizontal width, ● vertical width). To accelerate all the atoms during the fountain phase, the power has to be increased heating the atoms to a temperature of $14 \pm 1\ \mu$K (△ horizontal width, ▲ vertical width). (c) The center of mass velocity of the atomic cloud is proportional to the detuning between the upper and the lower beams, Δ.

velocity of the atomic cloud can be fine tuned. We adjust it by maximizing the number of atoms arriving at the cavity. During the time of flight of the atoms to the cavity, we change the current in the compensation coils to minimize the magnetic field in the science chamber.

3.3 Fabry-Pérot Cavity

The optical cavity is located 23 cm above the MOT. It consists of two spherical mirrors with high-reflectivity dielectric coatings made by Research Electro-Optics forming a Fabry-Pérot resonator (cf. Fig. 3.7 (a)).

We start with some general definitions. The modes of the cavity are determined by the mirror spacing, l, and the radii of curvature of the two mirrors, R_1 and R_2. In the following, we are only interested in the TEM_{00} modes with a Gaussian intensity profile with the waist w_0. The coupling of an individual atom with the transition dipole moment μ to one mode of the resonator is determined by the electric field per photon in the cavity. Obviously, the field and thus the coupling increases when the mode volume of the cavity, in which the photon is confined, is reduced. Quantitatively, the coupling constant at an anti-node of the cavity mode is given by

$$g_0 = \sqrt{\frac{\mu^2 \omega_c}{2\hbar \epsilon_0 V}}. \tag{3.1}$$

Here, $V = \frac{\pi l w_0^2}{4}$ designates the volume of the cavity mode, and ϵ_0 is the vacuum per-

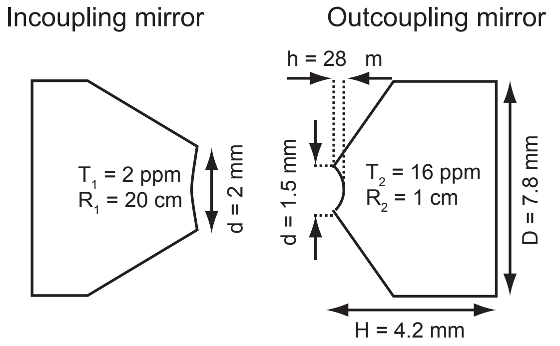

Figure 3.7: Geometry of the cavity mirrors (drawing not to scale). The asymmetry of the transmittance (T_1, T_2) leads to a high outcoupling efficiency. The asymmetry of the radii of curvatures (R_1, R_2) has two effects: First, the position of the waist of the cavity mode hardly changes with the cavity length. It is always located close to the fixed, weakly curved mirror. This is important because of the lengths adjustability of our cavity. Second, the small radius of curvature of one of the mirrors reduces the size of the waist, increasing the coupling constant. The sag height, h, of 28 μm of the strongly curved mirror sets a lower limit for the cavity length. Both mirrors are coned down to improve the transverse optical access to the cavity mode and reduce the sag height.

mittivity. Due to the non-zero transmittances of the cavity mirrors (T_1 and T_2) and optical losses in the substrate (L_1 and L_2), the electric field amplitude in the cavity decays with the field decay rate

$$\kappa = \frac{c\pi}{2l\mathcal{F}}. \tag{3.2}$$

$\mathcal{F}$ is the finesse of the optical cavity, which is related to the transmittances, T_1 and T_2, and losses, L_1 and L_2, of the two mirrors via

$$\mathcal{F} = \frac{2\pi}{T_1 + T_2 + L_1 + L_2}. \tag{3.3}$$

When designing a new cavity, the transmittances and curvatures of the two mirrors have to be chosen. In the following, we will discuss our respective choice of parameters for the two mirrors and characterize the resonator.

3.3.1 Curvature

The smaller the radius of curvature the smaller the waist and the higher the atom-cavity coupling. However, the sag height, h (cf. Fig. 3.7), sets a technical lower limit on the cavity length that can be achieved. It turns out that choosing two different radii of curvature, one strongly curved with R_1 = 1 cm and one only weakly curved with R_2 = 20 cm, is a good compromise. First, the waist is reduced compared to our previous setup [1] leading to an increased coupling strength at the same cavity length. Second, only one mirror has a significant sag height of approximately 28 μm that limits the minimum length of our cavity. Third, the longitudinal position of the waist, which determines the position of maximum coupling, is always located close to the weakly curved mirror. When altering the length by moving the strongly curved mirror, the longitudinal position of the waist, where we want to inject the atoms, does only change marginally (cf. [10] for a detailed discussion).

3.3.2 Finesse, Transmittance and Losses

To meet the strong-coupling condition, $g \gg \kappa$, a high finesse of the resonator (cf. Eq. 3.2) is required. In the past, most strong-coupling cavity-QED experiments have tried to maximize the finesse of their system by using mirrors with the lowest transmittance available [1, 11, 12, 13], which is on the order of a few ppm. However, one pays for this with a low detection efficiency. To understand this, we recall that, for a given average photon number, $\langle a^\dagger a \rangle$, in the cavity, the photon flux at the output mirror with transmittance T_2 is given by

$$\frac{I}{\hbar\omega} = 2\kappa \frac{T_2}{T_1 + T_2 + L_1 + L_2} \langle a^\dagger a \rangle. \tag{3.4}$$

The outcoupling efficiency $\eta_{\text{out}} = \frac{T_2}{T_1+T_2+L_1+L_2}$ takes into account that a certain fraction of photons is either lost in the mirror substrates or is transmitted through the *wrong* mirror and therefore cannot be detected. For a symmetric cavity with equal transmittances for both mirrors, the outcoupling efficiency is always smaller than 0.5. It is reduced further when the losses are on the order of the transmittances as it is case in the experiments mentioned before. To increase the outcoupling efficiency, we have chosen an asymmetric cavity with different transmittances of the two mirrors. The weakly curved incoupling mirror has a specified transmittance of 4 ppm and the strongly curved outcoupling mirror has a specified transmittance of 25 ppm.

As, in practice, the transmittance and the losses vary for each individual mirror, we have first characterized these parameters for our cavity mirrors. The finesse is determined by a ring-down measurement (cf. Fig. 3.8 (a)). By measuring the impinging light power, the reflected power and the transmitted power on resonance with the cavity the transmittance and losses of the mirrors can be determined [14]. This characterization was carried out before installing the cavity in the vacuum chamber. At a wavelength of 772 nm, obtained a finesse of $\mathcal{F} = 170000 \pm 5000$, a transmittance of $T_1 = 4.0 \pm 0.5$ ppm and $T_2 = 21.0 \pm 0.5$ ppm, respectively, and losses of $L = (L_1 + L_2)/2 = 5.5 \pm 0.5$ ppm. After installing the cavity in the vacuum chamber, we have found that the finesse is more sensitive to the wavelength than expected. In fact, at the probe wavelength of 780 nm the finesse was measured to be $\mathcal{F} = 195000 \pm 5000$. Assuming that this increase of the finesse is only due to a lower transmission at this wavelength, we estimate the transmittances to be $T_1 = 2.5 \pm 0.5$ ppm and $T_2 = 17.8 \pm 0.5$ ppm, respectively. This amounts to an outcoupling efficiency of $\eta_{\text{out}} = 0.57$. For comparison, the forerunner experiment [1] used a symmetric cavity with $T = 2.8$ ppm and $L = 4.5$ ppm resulting in an outcoupling efficiency of only $\eta_{\text{out}} = 0.19$.

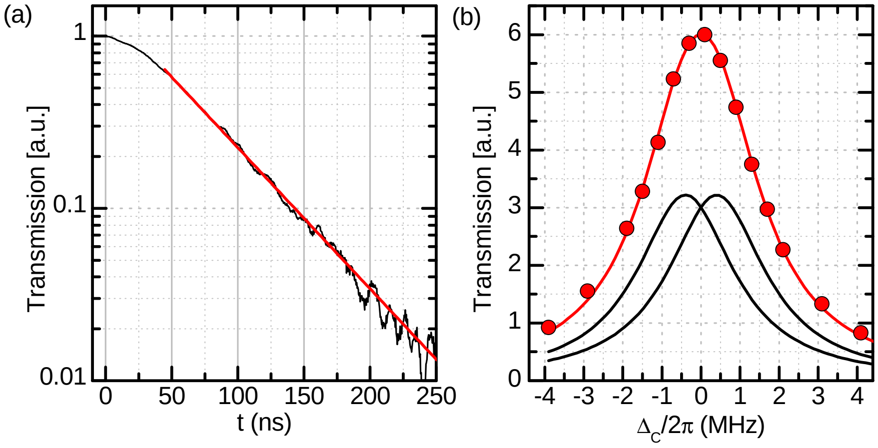

Figure 3.8: (a) Ring-down measurement of the cavity finesse. The decay of the transmission (black) is monitored after a resonant probe laser is rapidly switched off. For a length of 258 μm, an exponential fit (red line) yields a decay rate of $\kappa/\pi = 3.0 \pm 0.1$ MHz corresponding to a finesse of $\mathcal{F} = 2\pi c\tau/l = 195000$. (b) Empty-cavity transmission spectrum for circularly polarized input light (●). A fit of two Lorentzians (red line) with linewidth κ each (black lines) yields an upper limit of the birefringent splitting of 800 kHz.

3.3.3 Birefringence

The stress induced by the mirror mounts can cause birefringence in the mirror coatings. As the light undergoes many reflections (on the order of the finesse) when it propagates in the cavity, this small effect can add up to a significant optical path difference for the two main polarization axis. In the worst case, a splitting of the cavity resonances for the two polarization modes by as much as several cavity linewidths can be observed [12, 13, 15, 16]. This would cause serious trouble for our experiments where a well-defined mode with circular polarization is required to treat the atom as a simple two-level system.

Fig. 3.8 (b) shows a measured empty-cavity spectrum for circularly polarized input light. As no splitting of the resonance is visible by bare eye, the residual splitting has to be smaller than the cavity linewidth. Fitting a single Lorentzian to the measured spectrum yields a full width at half-maximum (FWHM) of 3.3 MHz, which is 10 % larger than the value of $2\kappa/2\pi = 3.0$ MHz expected from the ring-down measurement. This broadening can have two origins: First, a birefringent splitting smaller than the cavity linewidth. Second, frequency fluctuations of the probe laser (a diode laser locked to a rubidium spectroscopy) and of the cavity resonance due to mechanical vibrations. These fluctuations cause a convolution of the Lorentzian spectrum of the cavity with the distributions of the respective fluctuations. To give an upper bound for the birefringent splitting, we assume that the broadening is solely due to the birefringent splitting and fit two Lorentzians with a fixed width of 3.0 MHz to the data (red line). We obtain a splitting of 800 kHz corresponding to an upper limit of the birefringent splitting of 27 % of the cavity linewdith. This is compatible with the splittings observed in other

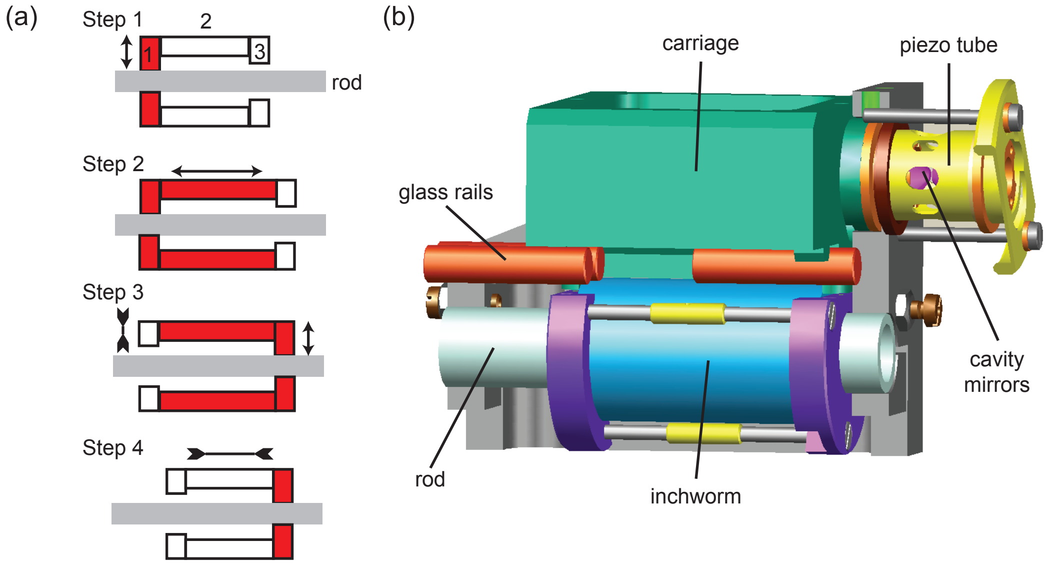

Figure 3.9: (a) Sketch of the working principle of the inchworm motor used to macroscopically change the cavity length. It conistst of three separate piezo elements (1,2 and 3). By repeating the four depicted steps, the inchworm motor crawls along a rod. (b) In doing so, it pushes or pulls a carriage on which one of the cavity mirrors is mounted. Length changes of up to several millimeters are possible. For the fine adjustement and stabilization of the cavity length, a piezo tube is used, which houses the second cavity mirror.

cavities in our group [17, 18, 19, 20].

3.3.4 Length Adjustment

In the past, the length of the cavity was chosen before putting it into the vacuum and it could not be modified later on. Only a fine tuning of the length on the order of a few wavelengths was possible by means of a piezo element. In this thesis, a new cavity design is introduced that allows to change the cavity length macroscopically while remaining in vacuum. This increases the versatility of the setup significantly as it allows to chose the length most appropriate for the experiment one wants to perform. In particular, the coupling constant, g_0, the decay rate, κ, and the cavity resonances can be tuned. These advantages come at the expense of an increased sensitivity to mechanical vibrations, which has to be counteracted by a good passive vibration isolation system and an active stabilization of the cavity length.

An *inchworm* motor (Burleigh) is used for the macroscopic length adjustment. The working principle of this piezo based motor is illustrated in Fig. 3.9 (a). It crawls along a rod with individual steps of less than 1 nm. When moving along the rod, the inchworm motor pushes a carriage, which is placed on three, parallel, polished rods made of ultra low expansion (ULE) glass acting as a rail for the motion of the carriage (cf. 3.9 (b)). The outcoupling mirror of the cavity is mounted at one end of the carriage. The other mirror is installed in a piezo tube (Ferroperm) that is directly connected to

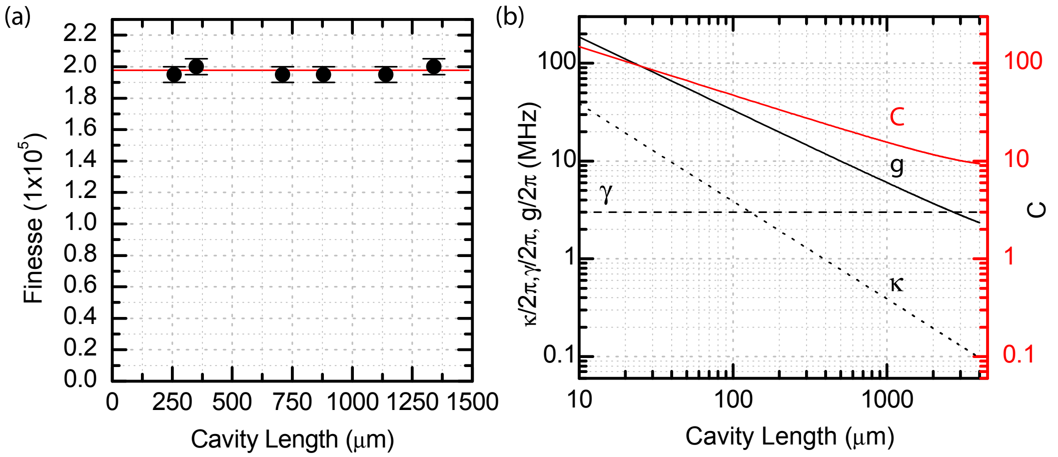

Figure 3.10: (a) Cavity finesse, $\mathcal{F}$, measured via cavity ring-down as a function of the cavity length. The finesse is constant with an average of 195000±5000. (b) Coupling constant, g_0 (solid black line), cavity field decay rate, κ (dotted line), polarization decay rate, γ (dashed line) and cooperativity, $C = \frac{g_0^2}{2\gamma\kappa}$ (solid red line), as a function of the cavity length. The variation of the cooperativity is a consequence of the change in the mode waist. Strong coupling is achieved for lengths up to about 1 mm.

the base of the assembly such that it stays fixed when the inchworm moves. This piezo tube is used for the active stabilization of the cavity length described in Section 3.4. Eight holes are drilled through the side walls of the tube to provide horizontal, vertical and diagonal transverse optical access to the atom in the cavity. The carriage as well as the mount are made of titan, which was chosen for its non-magnetic properties [10]. To stabilize the cavity length, the inchworm motor has to be disconnected from the power supply. Otherwise, it produces significant mechanical vibrations. Fig. 3.10 (a) shows the measured finesse of our cavity versus its length. Within the measurement uncertainties, the finesse does not vary for the evaluated lengths between 250 μm and 1250 μm. All experiments described in this thesis were performed with a cavity length of 258 μm.

To summarize the parameter space available with the length variable cavity, we have plotted the expected maximum coupling constant, g_0 (solid black line), the field decay rate, κ (dotted black line), the atomic polarization decay rate, γ (dashed black line), and the cooperativity, $C = \frac{g^2}{2\kappa\gamma}$, in Fig. 3.10 (b) as a function of the cavity length. The strong-coupling condition, $g_0 > \kappa, \gamma$, is fulfilled for lengths up to 1 mm. Note that we can operate in the bad cavity limit, $\kappa \gg \gamma$, the good cavity limit, $\kappa \ll \gamma$, as well as an intermediate regime, $\kappa \approx \gamma$. Further details on the performance of the inchworm can be found in [10, 20].

3.3.5 Vibration Isolation and Cavity Mount

The high finesse of our cavity makes it very sensitive to length fluctuations, which change its optical resonance frequency. To be more precise, the relative change of the cavity resonance frequency, ν, is equal to the relative change of the cavity length, $\Delta\nu/\nu = \Delta l/l$. Assuming that we want the frequency fluctuations to be much smaller than one cavity linewidth, $\Delta\nu \ll 2\kappa/2\pi$, which is a very pessimistic goal, we obtain $\Delta l \ll \frac{c}{2\nu\mathcal{F}} \approx 2$ pm. Achieving such a stability for a cavity with a rigid cavity is already challenging and requires a very good passive mechanical stability as well as an active stabilization of the cavity length. In our case, where one of the mirrors is movable, this becomes even more difficult. In fact, the first prototype of the length adjustable cavity described in [10] suffered from low mechanical stability. To overcome these limitations, a new vibration isolation system has been developed [20].

Its design, which is shown in Fig. 3.11, is inspired by the previous apparatus [1] and a system designed in Zürich [21] based on ideas developed for atomic force microscopes [22]. Several layers of heavy masses connected by springs and damping elements isolate the uppermost layer from vibrations. High masses and soft springs are desirable to keep the resonance frequency as low as possible.

Our system consists of three layers, stacked on top of each other. Each layer is made of a cylindrical copper block with masses between 1 and 2 kg. The lowest stack is placed on three, radially aligned rubber tubes made of Kalrez. We have chosen this material because it has slightly better outgasing properties than Viton, the most commonly used ultra-high-vacuum-compatible elastomer [23, 24]. The other two stacks are connected by a combination of metal springs and Kalrez tubes. The metal springs alone have a much lower resonance frequency than the Kalrez tubes. However, their damping constant is also very small. This makes the system very sensitive to oscillations at the resonance frequency as it has been observed in [25] where a vibration isolation system suspended only from metal springs was used. We find a good compromise by placing the stacks on Kalrez tubes but releasing the weight on the tubes by three vertical metal springs. In this way, the total spring constant and damping constant can be adjusted. In practice, this allow to reduce the resonance frequencies of the system from 50-100 Hz, for the rubber tubes only, down to about 10 Hz [20].

3.4 Cavity Stabilization and Dipole Trap

In addition to the passive vibration isolation, an active stabilization of the cavity length via a piezo tube is indispensable. It compensates for slow vibrations below the resonance frequency of the vibration isolation system as well as for residual higher frequency vibrations that pass through the isolation.

The conventional active stabilization scheme used in many experiments with optical cavities is depicted in Fig. 3.12 (a). The science cavity is locked to a stabilization laser using the Pound-Drever-Hall techinque [9]. The stabilization laser itself is usually stabilized with respect to a narrow linewidth transfer cavity. However, as this cavity also has to be stabilized, the resulting locking chain is quite complicated and involves a lot of technical overhead. To simplify the locking scheme, one can replace the transfer cavity by a frequency comb as a stable frequency reference (cf. Fig. 3.12 (b)). The stabilization laser is phase locked to the frequency comb. Most of the experiments described in this thesis were performed using this locking scheme that was introduced

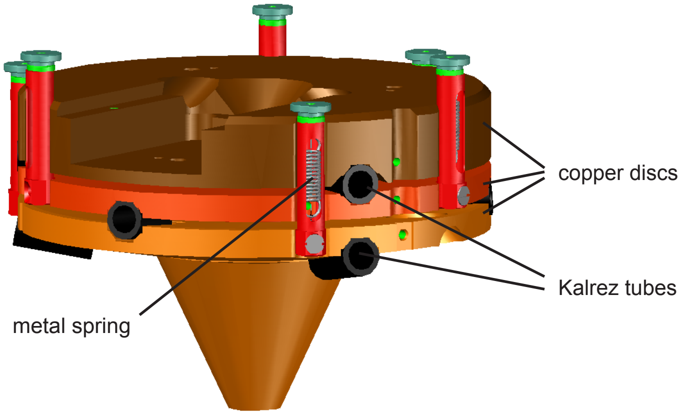

Figure 3.11: 3D drawing of the vibration isolation system. It consists of three layers of copper discs. The lowest layer sits on three, radially aligned rubber tubes made of Kalrez. The other two layers are suspended from metal springs with additional rubber tubes acting as an additional damping element. The cavity mount, which is not shown here, is installed in the pit on the uppermost layer.

in our group in [26, 27] and whose adaption to our setup is described in [8].

Even though this new scheme simplifies the setup considerably, it does not really improve the quality of the cavity lock, whose main bottleneck is the finite bandwidth of several kHz of the piezo tube which is used to stabilize the cavity length. As a result, high-frequency fluctuations of the stabilization-laser frequency which are too fast to be followed by the cavity lock result in intensity fluctuations of the intracavity power. When the stabilization laser is also used as a dipole trap, this causes significant parametric heating of the trapped atoms [28]. To solve this problem, a new locking scheme, described in the following section, was implemented towards the end of this thesis. The basic idea is to lock the stabilization laser directly to the high-finesse science cavity. This can be achieved with a high bandwidth thus minimizing the intensity fluctuations of the stabilization laser. The cavity is locked with respect to the frequency comb with the moderate bandwidth limited by the piezo tube. Even though this scheme does not reduce the absolute stability of the cavity length, it reduces significantly the intensity fluctuations of the stabilization light and therefore reduces parametric heating in the dipole trap.

3.4.1 Trapping and Stabilization Laser

One and the same laser is used to stabilize the cavity length and to serve as an intracavity dipole trap. The light is provided by a commercial tapered amplifier (TA100, Toptica) running at 785 nm. This wavelength was chosen because it has proven in the past to offer a good compromise between sufficiently far detuning from the atomic resonance and thus low scattering rates on the one hand, and good axial overlap between the modes of the probe and stabilization laser on the other hand. Moreover, it is sufficiently far detuned from the probe light to efficiently separate the two wavelengths

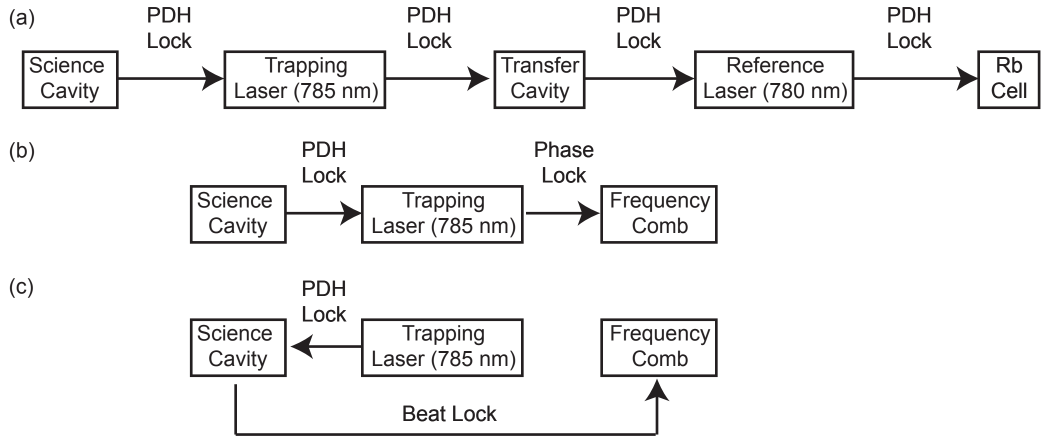

Figure 3.12: (a) Conventional locking chain with transfer cavity used in many previous cavity QED experiments [1, 13, 25, 29] making extensive use of the Pound-Drever-Hall (PDH) technique. (b) In the simplified locking chain introduced in [26], the transfer cavity is replaced by a frequency comb as a frequency reference. (c) Modified locking scheme used in this work. The dipole-trap laser can be locked onto the science cavity with a high servo bandwidth reducing intensity fluctuations of the dipole trap. An error signal for the science cavity lock is generated from the beat signal between the dipole-trap laser and the frequency comb (cf. text for details).

spectrally by means of interference filters. The high power generated by the tapered amplifier is sufficient to be used as a transverse dipole trap in the future. Details on the laser setup can be found in [8].

For the experiments described in this thesis, we only used the low power output of the grating stabilized seeding laser of the tapered amplifier. The optical setup is depicted in Fig. 3.13. The light is split into two parts. Each one passes through an AOM in double-pass configuration. The first part with a power of a few hundred μW is coupled into a fiber beam-splitter where it is overlapped with the light from the frequency comb. One output of the beam splitter is used to monitor the power, the second beam is focused through a 785 nm interference filter onto a fast, AC-coupled photodiode (FPD510, Menlo Systems). This beat signal is used for the cavity lock, which is described in the next section. The output of the second double-pass AOM is coupled into a fiber delivering the light to the breadboard mounted around the vacuum chamber. A 785 nm interference in front of the fiber eliminates residual light at 780 nm always present in the output of the laser diode.

3.4.2 Cavity Incoupling Setup

The stabilization light is superimposed with the probe light and coupled into the cavity. The corresponding optical setup is shown in Fig. 3.14. The stabilization light passes through an electro-optical phase modulator (EOPM) that generates sidebands at 15 MHz needed for the Pound-Drever-Hall lock to the cavity. After the EOPM a part of the light is reflected onto a photo-diode to stabilize its power. The rest of the beam

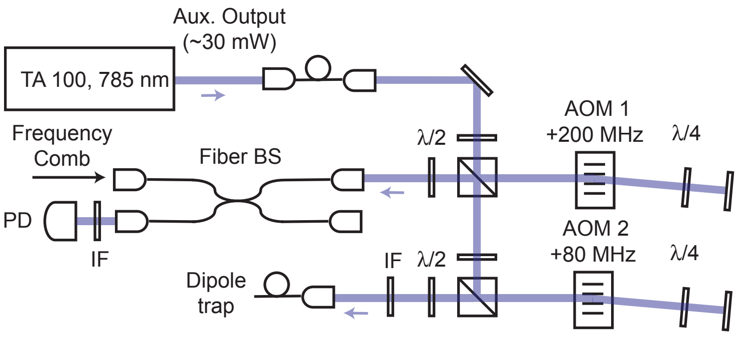

Figure 3.13: Optical setup of the stabilization and trapping laser. The auxilary output of a tapered amplifier (TA100) is split into two parts. The first part passes through an AOM in double-pass configuration (AOM 1) and is superimposed with a frequency comb in a fiber beamsplitter (BS). The beat signal is recorded with a photodiode (PD) whose signal is used to stabilize the cavity length (cf. text). The second part of the light also passes through an AOM in double-pass configuration (AOM 2). Then, it is coupled into a fiber that guides the light to the experiment.

passes through a polarizing beam splitter (PBS). The stabilization light is then superimposed with the probe light on a 99:1 beamsplitter. For the experiments described here, both beams are polarized linearly in the same direction. The combined beam is expanded by an adjustable beam expander and then focused through a $f = 50$ cm lens to achieve good mode matching with the cavity mode. Before entering the cavity, a quarter-wave plate turns the linear polarization into circular polarization, which is needed to drive the closed cycling transition in ^{85}Rb (cf. Fig. 3.2).

The back-reflected light from the cavity, which, after passing again through the quarter-wave plate, is polarized perpendicular to the incoming light, is separated from the incoming light at the PBS. It passes through an electro-optical amplitude modulator (EOAM) and is focused onto a fast photo-diode. The signal from the photo-diode is demodulated to generate a Pound-Drever-Hall error signal, which is fed-back onto the grating and the current of the stabilization laser to stabilize its frequency with respect to the science cavity. The EOAM is used to keep the amplitude of the error signal constant when we change the intensity of the stabilization laser [30], e.g., to trap atoms in the cavity.

3.4.3 Cavity Lock

Having the stabilization laser locked to the cavity is not sufficient, since its length can still drift. To counteract these drifts, we also have to stabilize the cavity to some fixed frequency reference. We use the beat signal between a frequency comb and the stabilization laser for this purpose. As the stabilization laser is locked to the cavity, a drift of the cavity length causes a drift of this beat frequency.

An error signal for this lock is generated using a technique that was originally introduced for a frequency-offset lock of two lasers [31]. The basic idea is to pass the

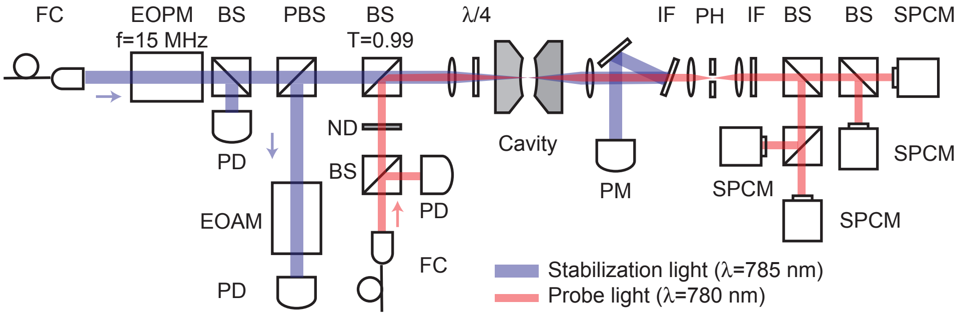

Figure 3.14: Optical setup at the experiment. The probe (red) and stabilization (blue) light arrive through polarization-maintaining optical fibers at two fiber couplers (FC). A part of each beam is separated by a beam-splitter (BS) and directed onto photodiodes (PD) to stabilize the intensities. The stabilization light is phase modulated by an electro-optical phase modulator (EOPM) at 15 MHz. The probe light is attenuated by a neutral density filter (ND). The two beams are overlapped at a 99:1 beam-splitter and enter the optical cavity in the vacuum chamber after beeing polarized circularly by a quarter-wave plate. The trap light which is back-reflected from the cavity is directed to a fast photodiode to generate a Pound-Drever-Hall error signal. Its amplitude can be adjusted by an electro-optical amplitude modulator (EOAM). The light which is transmitted through the cavity is spectrally separated by an interference filters (IF). The power of the stabilization light is monitored by a photomultiplier (PM), whereas the transmitted probe light is filtered spatially through a pinhole (PH) and passes through another interference filter. Finally, it is divided into four equal parts by three consecutive, non-polarizing beam-splitter (BS), and it is detected by four single-photon counting modules (SPCM).

beat signal between the frequency comb and the dipole-trap laser through an electronic low-pass filter (cut-off frequency 36 MHz). The power of the transmitted signal follows the transfer function of the low-pass filter with a steep slope at the cutoff frequency. This slope is used as an error signal for a feedback loop. To avoid mechanical resonances of the piezo tube, the output of the PID controller passes through a notch filter at 6 kHz and a low pass filter at 10 kHz before it is fed back to the piezo tube. In addition, it was found useful to introduce a variable resistor in series with the capacity of the piezo tube acting as an additional tunable low-pass filter to get rid of high-frequency electronic noise. Details on these and further measures to reduce mechanical and electronic noise can be found in [8]. The spectral width of the beat signal between the stabilization laser and the frequency comb acts as a measure of the absolute stability of the cavity length. Averaged over several seconds the FWHM is typically 300-400 kHz corresponding to about one tenth of the cavity linewidth or length fluctuations on the order of 200 fm.

3.5 Detection

The light which leaves the cavity through the mirror with the higher transmittance passes through a lens that collimates the beam. A slightly tilted 780 nm interference filter (MaxLine, Semrock), reflects the 785 nm stabilization light, which is then reflected onto a photomultiplier to monitor the transmitted power. The probe light at 780 nm that passes through the interference filter is focused through a 150 μm pinhole to eliminate stray light. After re-collimation of the beam, a second 780 nm interference filter eliminates residual light from the dipole trap. Finally, consecutive beam splitters divide the light into four beams, each of which is focused onto a single-photon counting module (SPCM, Perkin Elmer). Their transistor-transistor-logic (TTL) signals whose rising edges signal the detection of a photon are processed by a field-programmable gate array (FPGA), which saves a timestamp for each photon click with a temporal resolution of 1 ns [32].

The total detection efficiency, i.e., the probability for a photon that is lost from the cavity mode to be detected by one of the detectors, is given by $\eta_{\text{tot}} = \eta_{\text{out}} T^2 \eta_{\text{det}}$, where η_{out} is the outcoupling efficiency of the cavity, T the transmitivity of the interference filters at 780 nm and η_{det} the quantum efficiency of the single-photon counting modules. Putting in the numbers, $\eta_{out} = 0.57$ (cf. Section 3.3.2), $\eta_{\text{det}} \approx 0.55$ and $T \approx 0.95$, we obtain a total detection efficiency of 0.28. Compared to a value of 0.06 in the previous experiment [30], this means an improvement by almost a factor of 5.

3.6 Experimental Control and Data Evaluation

To perform the experiments described in this thesis, a number of analog and digital channels, controlling laser frequencies, intensities, magnetic fields, etc., have to be switched in a well-defined, programmable order. The experimental sequence is programmed in a home-made Labview program. It is transferred via local area network to an Adwin real-time system (Adwin Pro, T9) that executes the sequence. For future reference, the settings are saved to a database (PostgreSQL) running on a separate server. The timestamped photon clicks recorded by the detectors are saved onto an AFS-network volume. These experimental traces are analyzed by various Python scripts.

Curvatures	$R_1 = 20$ cm, $R_2 = 1$ cm
Transmittances	$T_1 = 2.5 \pm 0.5$ ppm, $T_2 = 17.8 \pm 0.5$ ppm
Losses	$L_1 + L_2 = 11.0 \pm 0.5$ ppm
Mirror spacing	l=258 μm (variable)
Finesse	$F = 195000 \pm 2000$ (variable)
Cavity decay rate	$2\kappa = 2\pi \cdot 3.0$ MHz (variable)
Mode waist	$w_0 = 19$ μm (variable)
Coupling constant	$g_0 = 2\pi \cdot 16$ MHz (variable)

Table 3.1: Summary of the most important cavity parameters.

3.7 Summary Cavity Parameters

We conclude with a summary of the most important cavity parameters. For those parameters that vary with the length of the cavity, we list the value used for the experiments described in this thesis. In Fig. 3.10 (b), the cavity decay rate, the coupling constant and the cooperativity are plotted as function of the cavity length.

Bibliography

[1] P. Münstermann, *Dynamik einzelner Atome in einem optischen Resonator höchster Finesse*, PhD thesis, Universität Konstanz (1999).

[2] P. Münstermann, T. Fischer, P. W. H. Pinkse, and G. Rempe, *Opt. Comm.* **159**, 63 (1999).

[3] S. Nussmann, M. Hijlkema, B. Weber, F. Rohde, G. Rempe, and A. Kuhn, *Phys. Rev. Lett.* **95**, 173602 (2005).

[4] K. M. Fortier, S. Y. Kim, M. J. Gibbons, P. Ahmadi, and M. S. Chapman, *Phys. Rev. Lett.* **98**, 233601 (2007).

[5] M. Khudaverdyan, W. Alt, I. Dotsenko, T. Kampschulte, K. Lenhard, A. Rauschenbeutel, S. Reick, K. Schärner, A. Widera, and D. Meschede, *New Journal of Physics* **10**, 073023 (2008).

[6] G. Lamporesi, *Determination of the gravitational constant by atom interferometry*, PhD thesis, Universita degli Studi di Firenze (2006).

[7] M. Balbach, *Characterization of Quantum States via Photon-Correlation and Field Measurements*, Diplomarbeit, Technische Universität München (2010).

[8] M. Apel, *Aufbau eines Cavity-QED-Experiments der nächsten Generation*, Diplomarbeit, Ludwig-Maximilians-Universität München (2009).

[9] R. Drever, J. Hall, F. Kowalski, J. Hough, G. Ford, A. Munley, and H. Ward, *Appl. Phys. B* **31**, 97 (1983).

[10] J. Almer, *Aufbau und Charakterisierung eines längenveränderbaren optischen Hoch-Finesse-Resonators*, Diplomarbeit, Technische Universität München (2006).

[11] C. J. Hood, *Real-time Measurement and Trapping of Single Atoms by Single Photons*, PhD thesis, California Institute of Technology (2000).

[12] J. A. Sauer, K. M. Fortier, M. S. Chang, C. D. Hamley, and M. S. Chapman, *Phys. Rev. A* **69**, 051804(R) (2004).

[13] I. Dotsenko, *Single atoms on demand for cavity QED experiments*, PhD thesis, Rheinische Friedrich-Wilhelms-Universität Bonn (2007).

[14] C. J. Hood and H. J. Kimble, *Phys. Rev. A* **64**, 033804 (2001).

[15] T. W. Lynn, *Measurement and Control of Individual Quanta in Cavity QED*, PhD thesis, California Institute of Technology (2003).

[16] R. Gehr, J. Volz, G. Dubois, T. Steinmetz, Y. Colombe, B. L. Lev, R. Long, J. Estève, and J. Reichel, *Phys. Rev. Lett.* **104**, 203602 (2010).

[17] H. Specht, *Einzelatom-Quantenspeicher für Polarisations-Qubits*, PhD thesis, Technische Universität München (2010).

[18] F. Rohde, *Ein optischer Resonator hoher Finesse als Atomdetektor*, Diplomarbeit, Max-Planck-Institut für Quantenoptik und Technische Universität München (2003).

[19] I. Schuster, A. Kubanek, A. Fuhrmanek, T. Puppe, P. W. H. Pinkse, K. Murr, and G. Rempe, *Nature Phys.* **4**, 382 (2008).

[20] B. Hagemann, *Vibration isolation and spectroscopy of a high-finesse optical resonator*, Diplomarbeit, Technische Universität München (2008).

[21] A. Öttl, S. Ritter, M. Kohl, and T. Esslinger, *Rev. Sci. Instr.* **77** (2006).

[22] M. Okano, K. Kajimura, S. Wakiyama, F. Sakai, W. Mizutani, and M. Ono, *Journal of Vacuum Science and Technology A* **5** (1987).

[23] L. de Chernatony, *Vacuum* **27**, 605 (1977).

[24] T. E. Northup, *Coherent Control in Cavity QED*, PhD thesis, California Institute of Technology (2008).

[25] K. M. Fortier, *Individual Trapped Atoms for Cavity QED Quantum Information Applications*, PhD thesis, Georgia Institute of Technology (2007).

[26] J. Bochmann, M. Mücke, G. Langfahl-Klabes, C. Erbel, B. Weber, H. P. Specht, D. L. Moehring, and G. Rempe, *Phys. Rev. Lett.* **101**, 223601 (2008).

[27] J. Bochmann, *Coherent dynamics and state detection of single atoms in a cavity*, PhD thesis, Technische Universität München (2010).

[28] T. A. Savard, K. M. O'Hara, and J. E. Thomas, *Phys. Rev. A* **56**, 1095 (1997).

[29] D. Boozer, *Raman Transition in Cavity QED*, PhD thesis, California Institute of Technology (2005).

[30] P. Maunz, *Cavity cooling and spectroscopy of a bound atom-cavity system*, PhD thesis, Max-Planck-Institut für Quantenoptik und Technische Universität München (2004).

[31] N. Strauss, I. Ernsting, S. Schiller, A. Wicht, P. Huke, and R.-H. Rinkleff, *Appl. Phys. B* **88**, 21 (2007).

[32] C. Sames, M. Balbach, M. Koch, A. Kubanek, P. Pinkse, and G. Rempe, FPGA-based Feedback Control of a Single Atom Trajectory, in *Virtuelle Instrumente in der Praxis 2010*, edited by R. Jamal and R. Heinze, pp. 315–320, VDE Verlag, Berlin (2010).

Chapter 4

Fine Structure of a Fabry-Pérot Resonator

The content of this chapter has partially been submitted for publication in:
M. Zeppenfeld, M. Koch, B. Hagemann, M. Motsch, P. W. H. Pinkse, and G. Rempe, *"Spin-Orbit Coupling in a Fabry-Perot Resonator via Berry's Geometric Phase"*.

Contents

In free space, Maxwell's equations can be written as a set of vectorial wave equations. The spherical mirror surfaces of the Fabry-Pérot cavity impose additional boundary conditions. Solutions to Maxwell's equations with a well-defined frequency which satisfy these boundary conditions are called the eigenmodes of the cavity. The corresponding discrete resonance frequencies form the spectrum of the resonator. Its calculation is relatively straightforward in the paraxial approximation when the light propagates almost parallel to the optical axis of the resonator.

In this chapter, we present spectroscopic measurements of the mode structure of our cavity. Due to its narrow linewidth, even small deviations from the paraxial approximation can be observed. We find a frequency splitting of higher-order transverse modes that is not predicted by the paraxial approximation. It can be explained quantitatively by recent theoretical calculations of higher-order corrections to the paraxial approximation [2, 3]. The splitting bears a formal resemblance to the fine structure observed in atomic spectra, which is a consequence of corrections to the bare, non-relativistic Schrödinger equation. In particular, a polarization-dependent splitting occurs as a consequence of the coupling between the intrinsic, i.e., polarization, and orbital angular momentum of the circulating light field. This effect is in close analogy to the spin-orbit coupling in atomic systems.

4.1 Empty-Cavity Spectrum in the Paraxial Approximation

The eigenmodes of an empty Fabry-Pérot cavity in the paraxial approximation are given by the Laguerre-Gaussian modes [1]. Two global parameters, the Rayleigh length, z_R, and the position of the mode waist are fixed by the curvature of the cavity mirrors and the length of the cavity, L. Each individual mode is characterized by a longitudinal index, n, and two integer mode indices, ν and L_z. The index, ν, determines the number of radial nodes of the mode profile. L_z reflects the orbital angular momentum of the mode [4]. The resonance frequencies can be calculated by requiring that the round trip phase shift in the resonator must be a multiple of 2π such that the circulating waves interfere to a standing wave. In the case of a symmetric cavity with equal radii of curvature for both mirrors, this condition can be written in terms of the dimensionless parameter $\bar{c} = kz_R$ (with the wave vector $k = 2\pi/\lambda$) as:

$$\underbrace{\frac{2\bar{c}L}{z_R}}_{O(\bar{c})} \underbrace{-4(2\nu + L_z + 1)\arctan(\frac{L}{2z_R})}_{O(1)} = 2\pi n. \tag{4.1}$$

The longitudinal mode index n determines the number of anti-nodes of the standing wave in the cavity. The parameter $\bar{c}$ can be considered as a measure for the validity of the paraxial approximation. The larger it is, i.e., the larger the Rayleigh length is compared to the wavelength, the better the paraxial approximation is justified.

Most important for the following discussion is that all transverse modes with constant $2\nu + L_z$ are degenerate. Moreover, in the paraxial approximation, the polarization is treated independently of the transverse mode structure. In other words, each transverse mode with fixed n, ν and L_z has the same resonance frequency for the two circular polarization modes, which we denote by $\sigma = \pm 1$.

4.2 Beyond the Paraxial Approximation - the Resonator Fine Structure

The left hand side of Eq. 4.1 can be considered as the first two terms of a power series expansion in terms of the small parameter $\frac{1}{\bar{c}}$. The calculation of next-order ($O(\frac{1}{\bar{c}})$) correction terms has been achieved recently [2, 3] by expressing the vectorial wave equation in terms of a different coordinate system, namely spheroidal coordinates [5]. After a lengthy calculation, one obtains the following resonance condition:

$$\underbrace{\frac{2\bar{c}L}{z_R}}_{O(\bar{c})} \underbrace{-4(2\nu + L_z + 1)\arctan(\frac{L}{2z_R})}_{O(1)} \underbrace{-\frac{1}{\bar{c}}\left(\frac{3L_z^2}{8} + \sigma L_z - M\right)\left(\frac{L}{2z_R} + \frac{2z_R}{L}\right)^{-1}}_{O(\frac{1}{\bar{c}})} = 2\pi n. \tag{4.2}$$

The correction term contains three summands: The last one, proportional to $M = \frac{1}{8}((2\nu + L_z)^2) + 2(2\nu + L_z) - 4)$, only depends on $2\nu + L_z$ and, therefore, only causes a

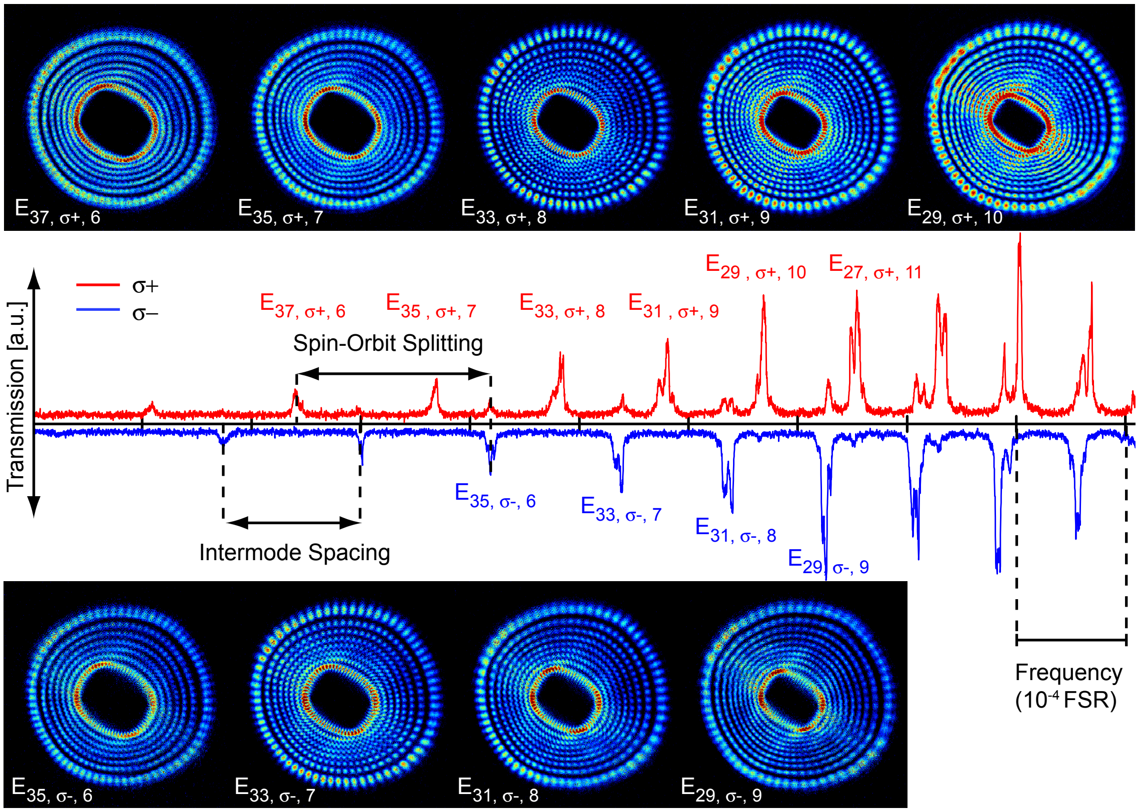

Figure 4.1: Zoom into the empty-cavity spectrum. Two series of Laguerre-Gaussian modes ($E_{J,\sigma,\nu}$ with $J = L_z + \sigma$) are observed for the two different input polarizations σ. In contradiction with the paraxial approximation, Laguerre-Gaussian modes with constant $2\nu + L_z$ are not degenerate. The intermode spacing between adjacent transverse modes and the spin-orbit splitting between modes with equal orbital angular momentum but opposite polarization are extracted for further analysis.

small spectral shift of all degenerate modes with constant $2\nu + L_z$. However, the first two summands have striking consequences: First, a frequency shift that scales quadratically with L_z is predicted. As a consequence, the degeneracy of different Laguerre-Gaussian modes with constant $2\nu + L_z$ is expected to be lifted, and a splitting that increases linearly with L_z is expected. Second, the additional coupling term, $\propto \sigma L_z$, predicts a polarization and orbital-angular-momentum-dependent splitting like the spin-orbit coupling term in atomic physics. In direct analogy to the situation in atomic physics, we therefore introduce the total angular momentum, $J = L_z + \sigma$, as a new mode index to describe the coupled modes.

4.3 Experimental Procedure

For our cavity parameters, the correction terms are on the order of $\frac{1}{\tilde{c}} \approx 5 \cdot 10^{-5}$ compared to the free spectral range. Therefore, a high-finesse resonator with a small cavity linewidth is necessary to observe them. One experimental difficulty lies in the discrim-

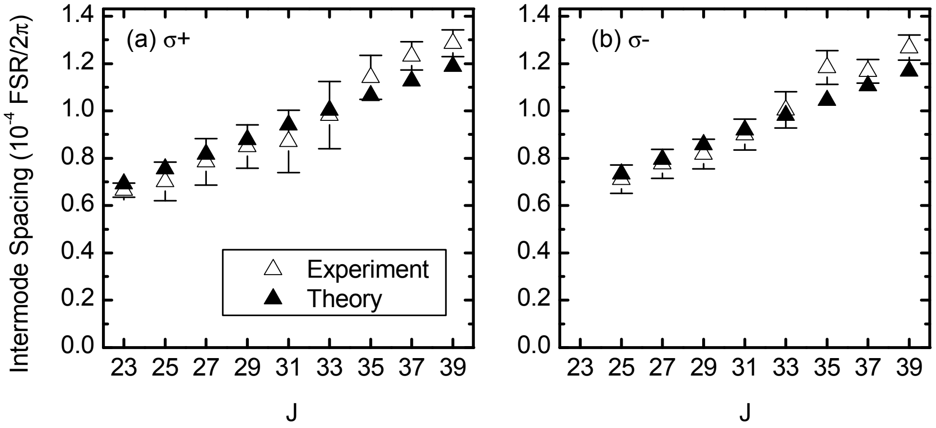

Figure 4.2: The experimentally observed (△) intermode spacings for σ_+ (a) and σ_- (b) polarized input light are in excellent agreement with the theoretically predicted corrections (▲) to the paraxial approximation without any additional fit parameters.

ination of these systematic splittings from unsystematic splittings of transverse modes due to mirror imperfections that are present in most high-finesse cavities, e.g., [6]. To avoid this problem, we study modes with a very large mode index L_z. As the predicted shift scales quadratically with L_z, the resulting splitting increases linearly with L_z and, therefore, can become much larger than the cavity linewidth and residual shifts due to mirror imperfections. To excite these higher-order modes, the probe beam is misaligned from the cavity axis and tilted. A quarter-wave plate in front of the cavity allows to switch between σ^+ and σ^- polarized input light. The light which is transmitted through the cavity is split by a non-polarizing beam splitter. One arm is directed onto a photo-multiplier. In the other arm, a camera records the beam profile. The spectrum of the cavity is measured by scanning the cavity length via the piezo tube and simultaneously recording the transmission spectrum and mode profile with the photo-multiplier and camera, respectively.

4.4 Experimental Results

Fig. 4.1 shows a zoom into a single spectral line of a higher-order transverse mode of the empty cavity. We plot the transmission of the cavity as a function of the frequency in units of the free spectral range (FSR). Two spectra have been recorded for σ^+- and σ^--polarized input light. Instead of a single line, as expected by the paraxial approximation, two series of spectral lines can be observed that do not overlap for the two different input polarizations. For some of the spectral lines, the corresponding mode profiles are also displayed showing the annular structure typical for the Laguerre-Gaussian modes.

We determine the total angular momentum, J, and the mode index ν, by counting the number of azimuthal and radial nodes in the mode profiles, respectively. The mode profiles in Fig. 4.1 are designated with their corresponding indices. We find that, as expected, $2\nu + L_z = 48$ is a constant for all the modes in these series.

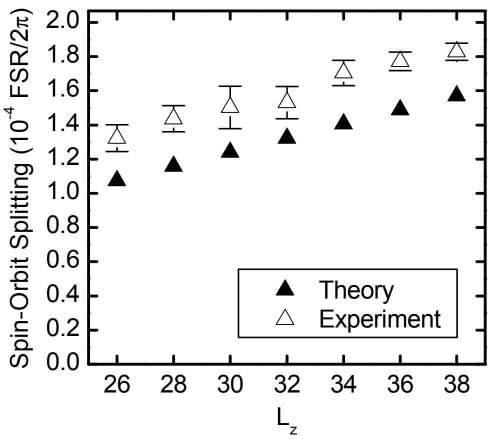

Figure 4.3: The spin-orbit splitting (△) is a consquence of a coupling between the intrinsic (polarization, σ) and the orbital angular momentum L_z of the light beam. As predicted by theory (▲), it scales linearly with L_z. However, a systematic discrepancy of about 20 % between theory and experiment is found.

For a quantitative analysis of the fine structure, we extract the *intermode spacing* between adjacent spectral lines with the same polarization, i.e., $E_{J,\sigma^+,\nu} - E_{J+2,\sigma^+,\nu-1}$ (cf. Fig. 4.1 for the definition). The results are plotted in Fig. 4.2. The splitting is in excellent agreement with the theoretical predictions without any free fit parameter.

We also observe the expected splitting between the different polarization modes. We extract the *spin-orbit splitting* between modes with equal orbital angular momentum, i.e., $E_{L_z+1,\sigma^+,6} - E_{L_z-1,\sigma^-,6}$ (cf. Fig. 4.1 for the definition). Plotting the spin-orbit splitting as a function of the orbital angular momentum L_z, we find a linear dependence (cf. Fig. 4.3). This confirms the predicted spin-orbit-coupling term proportional to $L_z\sigma$. Unfortunately, the quantitative agreement of the spin-orbit splitting with theory is not very good. A systematic deviation of about 20 % is found. Some potential explanations for this discrepancy are discussed in [7].

A detailed discussion of this topic, in particular, a detailed explanation of the theoretical calculations, an alternative explanation of the spin-orbit coupling in terms of a geometric phase and an extended discussion of these and further experimental results, will be a subject of the thesis of my colleague Martin Zeppenfeld.

Bibliography

[1] B. Saleh and M.C.Teich, *Fundamentals of photonics*, Wiley (1991).
[2] M. Zeppenfeld, *New Journal of Physics* **11**, 073007 (2009).
[3] M. Zeppenfeld and P. W. H. Pinkse, *Optics Express* **18**, 9580 (2010).
[4] L. Allen, M. W. Beijersbergen, R. J. C. Spreeuw, and J. P. Woerdman, *Phys. Rev. A* **45**, 8185 (1992).
[5] C. Flammer, *Spheroidal Wave Functions*, Stanford University Press (1957).

[6] T. A. Puppe, *Trapping and observing single atoms in the dark*, PhD thesis, Technische Universtität München (2007).

[7] B. Hagemann, *Vibration isolation and spectroscopy of a high-finesse optical resonator*, Diplomarbeit, Technische Universität München (2008).

Chapter 5

Classical Dynamics - Feedback Cooling

The content of this chapter has partially been published in:
M. Koch, C. Sames, A. Kubanek, M. Apel, M. Balbach, A. Ourjoumtsev, P. W. H. Pinkse, and G. Rempe, *"Feedback Cooling of a Single Neutral Atom"*, Physical Review Letters **105**, 173003 (2010).

Contents

Over the last decades, the invention of a variety of cooling schemes for atoms, ions and elementary particles has been essential for the experimental progress in particle physics, precision spectroscopy, quantum information processing and quantum optics. One scheme that is particularly suited for individual particles is feedback cooling. The underlying principle is extremely simple: If the motion of the particle can be observed, one can, using a fast feedback loop, engineer a suitable dissipative force that slows down the particle. The performance is mainly limited by the accuracy with which the particle trajectory can be measured. Feedback cooling has been implemented very successfully for anti-protons under the name of stochastic cooling [1], for electrons and protons in Penning traps [2, 3] and for ions in Paul traps [4]. It is not a coincidence that all these implementations involved charged particles, for which the detection of the motion by induced currents and the actuation of the motion by static electric and magnetic fields is relatively straightforward.

An implementation of feedback cooling for neutral particles (i.e. atoms) has been challenging because of the lack of an efficient method to observe the particle motion in real time. Such a method is provided by cavity QED. Already the first strong-coupling cavity QED experiments with cold atoms showed that, due to the position dependence of the coupling constant, the transmitted light field carries information about the position of the atom [5, 6]. This was used shortly afterwards in the first experiments with trapped atoms to observe the atomic trajectories in real time [7, 8]. The latter of these experiments already made use of a very simple feedback scheme to trap the atom, switching on an intracavity dipole trap conditioned upon the detection of the arrival of an atom. The obvious next step was to use the information about the position of the atom to reduce its kinetic energy. The first experiment going in this direction showed an increase of the average storage time of up to 30% by applying a simple feedback strategy [9]. However, in this experiment one and the same laser was used to probe, trap and actuate the atomic motion. This has several disadvantages. First, as the laser is almost on resonance with the atom, strong heating effects limit the average storage times to only a few hundred microseconds. Second, there is a strong backaction between observation and actuation disturbing the position measurement. Third, the heating rates depend crucially on the power of the probe laser, which made it impossible to demonstrate cooling of the atom.

Even though simulations showed that these problems can be overcome by using separate lasers to probe and trap the atom [10], it took several years until this was realized in an experiment [11]. Three different lasers were used to probe, trap and actuate the atomic motion. An increase of the storage time from 6 ms without feedback up to 24 ms with feedback was reported. The performance was mainly limited by two technical constraints: First, the low detection efficiency required the measurements to be performed at high probe powers where strong radial momentum diffusion occurs. Second, the limited transverse optical access to the cavity caused a significant increase of stray light when a transverse repumping beam was added to compensate for off-resonant scattering to the dark $F=2$ hyperfine ground state. This stray light reduced the performance of the feedback as confirmed by Monte-Carlo simulations [12].

The higher detection efficiency and the better optical access of our new setup allow to overcome these limitations. After explaining in detail the principle of feedback cooling and how it was implemented in the current setup, we will show in the following that we are now able to achieve average storage times exceeding one second corresponding to a 30-fold increase compared to the storage time without feedback. In addition, we measure the temperature of the atom and observe its improved localization. Most of the experimental results are in qualitative agreement with a simple theoretical model.

5.1 The Principle of Feedback Cooling

As illustrated in Fig. 5.1 (a), feedback cooling involves three steps: a measurement of the atomic motion, processing of this measurement based on some feedback algorithm and, finally, the feedback on the atomic motion. In the following, we will quickly review the concrete implementations of these steps in our system.

5.1.1 Atomic Motion in the Intracavity Dipole Trap

The atom oscillates in a red-detuned intracavity dipole trap. The strong confinement to half a wavelength in the axial direction leads to high trapping frequencies on the order of several hundred kHz in this direction. The radial confinement is much weaker resulting in radial trapping frequencies on the order of only several kHz. Currently, we are only able to track the much slower radial motion in real time. The Gaussian shape of the potential leads to an anharmonic oscillation of the atom.

To observe the atomic motion, a weak probe beam close to the atomic and cavity resonance is used, which, in addition, introduces dissipative cooling and heating forces to the atomic motion. For the detuning used in these experiments, the probe light cools the atomic motion along the cavity axis. However, axial cavity cooling is always accompanied by momentum diffusion, i.e., heating in the radial direction limiting the storage time without feedback cooling [13].

5.1.2 Observation of the Atomic Motion

Strong coupling of the atom to the cavity mode leads to a dramatic change of the spectrum of the system as it has been observed in [14, 15]. The Lorentzian transmission spectrum of the empty cavity is replaced by two normal modes separated by the position-dependent coupling constant, $g(r,z)$. As shown in the theoretical transmission spectra in Fig. 5.1 (b), the normal-mode splitting varies with the radial position of the atom. This implies that, for a fixed detuning of the probe light with respect to the cavity, the transmitted light intensity carries information about the position of the atom.

To achieve a maximum modulation of the transmitted intensity and to avoid axial losses by cavity cooling, we tune the probe laser on resonance with the empty cavity ($\Delta_c = 0$). Plotting the transmission as a function of the radial position 5.1 (c), we see that the transmission decreases when an atom approaches the cavity center because the probe laser is now off resonance with the normal modes. A detailed discussion on this and other potential choices of the probe-laser detuning can be found in [12, 16]. In principle, the average transmission depends also on the axial position of the atom. However, as discussed in the next section, we integrate the transmission signal typically over several microseconds. This corresponds to an averaging over the faster axial motion.

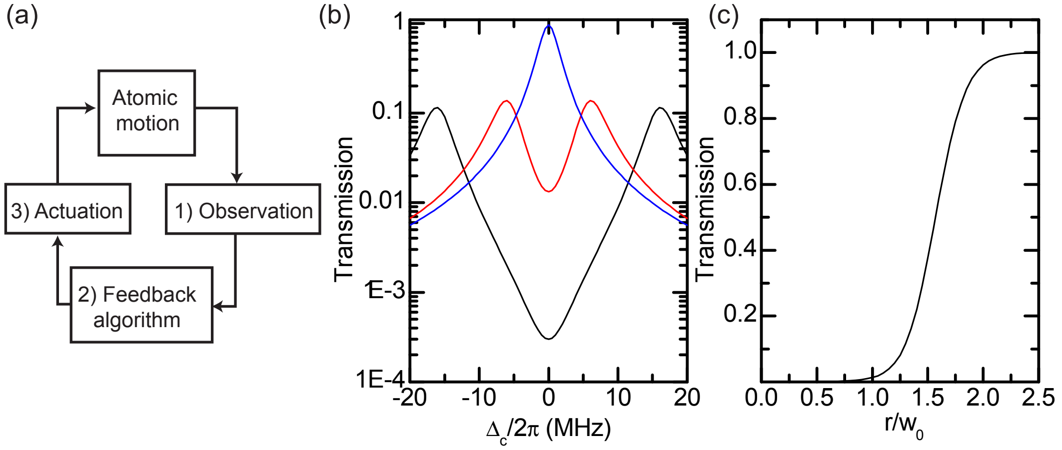

Figure 5.1: (a) Feedback cooling involves three steps: The atomic motion is observed, the outcome of this measurement is processed by some feedback algorithm, and the feedback loop is closed by an actuation of the atomic motion. (b) To observe the atom motion, we make use of the position dependence of the coupling constant, g. As a consequence the spectrum of the system changes with the position of the atom. This is illustrated by plotting the cavity transmission as a function of the probe-laser detuning from the cavity resonance, Δ_c, for different radial positions of the atom, r=0 (black), r=w_0 (red), r=$2w_0$ (blue). For simplicity, the atom-cavity detuning was set to zero, and the position-dependent Stark shift due to the dipole trap was neglected. (c) On resonance with the cavity, $\Delta_c = 0$, the transmission increases with the radial distance of the atom from the cavity center.

5.1.3 Feedback Algorithm

We use the same red-detuned laser to trap and actuate the atomic motion. If we had perfect knowledge about the atomic trajectory, the optimal feedback strategy would be to switch the potential to a low value, U_{min}, when the atom arrives at an outer turning point of its trajectory, i.e., when the reduction of the potential energy is maximized. It has to be switched back to a high value, U_{max}, when the atom passes through the center of the cavity mode. To avoid axial losses, we cannot switch off the dipole trap completely, but we always need some finite depth U_{min}. Moreover, the maximum potential depth is also limited to some finite value U_{max}, which is determined by the bare atom-cavity detuning. If the AC-Stark shift due to the dipole trap becomes larger than the atom-cavity detuning, the probe laser becomes red-detuned with respect to the atomic transition, which leads to heating in the axial direction [15].

In the experiment, we identify the turning points of the atomic trajectory by comparing the number of detected photons, N_1 and N_2, in two successive intervals with a duration Δt, the integration time. If the count rate is increasing, $N_2 \geq N_1$, the atom is supposedly moving outwards. If it is decreasing, $N_2 < N_1$, we estimate the atom to be moving inwards. This feedback strategy is illustrated in Fig. 5.2 (a). In practice, it has been found that an even better performance can be achieved by introducing a small threshold, N_{th}. We switch to the high potential for $N_2 \geq N_1 + N_{th}$ and to the low

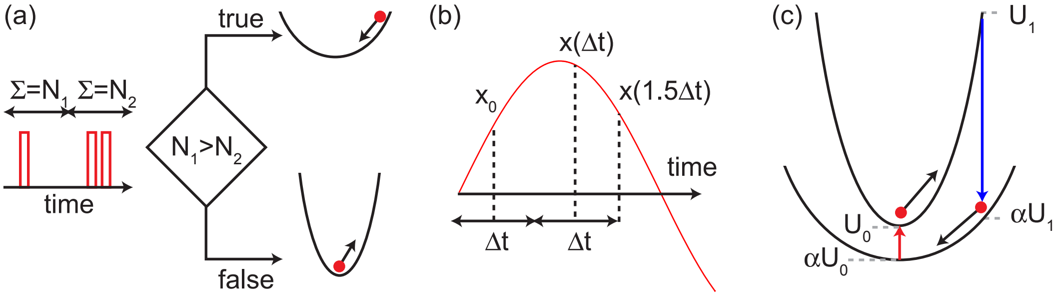

Figure 5.2: (a) The feedback algorithm is very simple: The number of detected photons, N_1 and N_2, in two successive intervals with a certain duration (the integration time Δt) are compared. If the transmission is decreasing, the atom is most likely moving radially inwards. The dipole potential is therefore switched to a low value. Otherwise, it is switched to a high value. (b) To quantify the quality of our velocity estimation, a simple theoretical model is introduced. The transmission for an atom at the position $x(0)$ and $x(\Delta t)$ is evaluated and compared with the radial direction of the velocity at the end of the integration time, $\mathrm{sign}(v(1.5\Delta t)x(1.5\Delta t))$. This enables us to calculate the probability to estimate the direction of the velocity correctly. (c) The net amount of energy lost per feedback cycle (corresponding to half an oscillation period) is given by the difference between the energy loss at the outer turning point and the energy gain at the inner turning point of the atom trajectory. For the simple one-dimensional model considered here, the energy reduction per half oscillation period is $1-\alpha$ times the original energy, $U_1 - U_0$, where α is the ratio between the low and high dipole potential.

potential otherwise. The optimal choice of this threshold will be discussed later on.

5.2 Theoretical Models

5.2.1 Fidelity of the Velocity Measurement

It is obvious that the performance of the feedback algorithm depends critically on the quality of our information about the atomic trajectory. To quantify this information, we introduce the fidelity, $F = 2p - 1$, of our measurement. Here, p designates the averaged probability to correctly estimate the direction of the radial motion, i.e., whether the atom is moving inwards or outwards. To be more precise, it is the probability to observe an increasing number of photon counts ($N_2 \geq N_1$) and have the atom moving outward plus the probability to observe a decreasing number of photon counts ($N_2 < N_1$) and have the atom moving inward. This probability has to be averaged over all possible initial positions and velocities of the atom. The fidelity takes values between -1 and 1. The larger it is, the better our velocity estimation, whereas a value of 0 means that the measurement and the atomic trajectory are uncorrelated, and the feedback is not expected to work. Negative values imply an anti-correlation between the trajectory and the measurement. The feedback strategy is then inverted and thus expectedly heats the atom.

1-D Model

In the following, we will introduce a very simple model, for which we can calculate the fidelity numerically. First, we only consider the motion of the atom in one dimension. For an atom at a certain radial position, x_0, we can calculate the average number of photon clicks, $\bar{N}(x_0) = 2\kappa\eta_{\text{tot}}\Delta t\langle a^\dagger a\rangle_{x_0}$, during the integration time, Δt, for a total detection efficiency η_{tot}, cavity field decay rate κ and the position-dependent average intracavity photon number $\langle a^\dagger a\rangle_{x_0}$. The conditional probability to detect N_1 photons for an atom at the position x_0 is then given by a Poisson distribution with the mean value $\bar{N}(x_0)$:

$$P(N_1|x_0) = \frac{\bar{N}(x_0)^{N_1}\exp\left(-\bar{N}(x_0)\right)}{N_1!}. \tag{5.1}$$

For an initial velocity v_0 and a harmonic potential with oscillation frequency ω, the position after the time t is

$$x(t) = x_0 cos(\omega t) + v_0 sin(\omega t)/\omega. \tag{5.2}$$

During the first integration interval, the atom moves to the position $x(\Delta t)$. The probability to detect N_2 photons during the second interval also follows a Poisson distribution with the mean value $\bar{N}(x(\Delta t))$. Multiplying the two Poisson distributions, we obtain the conditional probability $P(N_1, N_2|x_0, v_0)$ to detect N_1 photons during the first interval and N_2 photons during the second interval, given an atom with an initial position x_0 and velocity v_0. We use Bayes' theorem to calculate the mutual probability to detect N_1 and N_2 photons during the successive intervals and to have the initial position and velocity x_0 and v_0, respectively:

$$P(N_1, N_2, x_0, v_0) = P(N_1, N_2|x_0, v_0)P(x_0, v_0) \tag{5.3}$$

Using the Gaussian position and velocity distribution, $P(x_0, v_0)$, of an atom in thermal equilibrium in an harmonic potential, we can now calculate the probability, p, to estimate the radial direction of the velocity correctly. For this purpose, we integrate the mutual probability, $P(N_1, N_2, x_0, v_0)$, over those values of x_0, v_0, N_1 and N_2 for which the count rate is increasing ($N_2 \geq N_1$) and the atom is moving outwards at the end of the second time bin ($x(1.5\Delta t)\cdot v(1.5\Delta t) > 0$), or the count rate is decreasing and the atom is moving inwards ($x(1.5\Delta t)\cdot v(1.5\Delta t) < 0$). Note that we are only interested in the direction of the velocity after the end of the second interval (when the potential is switched) corresponding to the time $1.5\Delta t$ after the center of the first interval (cf. Fig. 5.2 (b)). In total, we thus find

$$\begin{aligned} p = &\underbrace{\sum_{N_1=0}^{\infty}\sum_{N_2=N_1}^{\infty}\int_{x_0}\int_{v_0\in x(1.5\Delta t)\cdot v(1.5\Delta t)\geq 0} P(N_1, N_2, x_0, v_0)\mathrm{d}x_0\mathrm{d}v_0}_{\text{atom is moving outwards, count rate is increasing}} \\ + &\underbrace{\sum_{N_2=0}^{\infty}\sum_{N_1=N_2+1}^{\infty}\int_{x_0}\int_{v_0\in x(1.5\Delta t)\cdot v(1.5\Delta t)<0} P(N_1, N_2, x_0, v_0)\mathrm{d}x_0\mathrm{d}v_0,}_{\text{atom is moving inwards, count rate is decreasing}} \end{aligned} \tag{5.4}$$

from which we directly get the fidelity, $F = 2p - 1$.

2-D Model

In reality, the atom moves of course in three dimensions. The axial oscillations happen on a much shorter timescale than the radial oscillations. We can take this motion into account simply by using a reduced maximal coupling constant g_{eff}. We are still left with the motion in the two radial dimensions. The generalization of our previous arguments to two dimensions is straightforward: The position and the velocities x_0 and v_0 are now two dimensional vectors $\vec{x}_0$ and $\vec{v}_0$. In the harmonic approximation, the oscillation in each spatial direction can be treated independently. Eq. 5.2 is thus applicable to calculate the respective positions and velocities. To calculate the fidelity (cf. Eq. 5.4), we have to integrate over both spatial and both momentum dimensions. The integration limits, which are set by the condition that the atom is moving outwards at the end of the second interval, are given by $\vec{x}(1.5\Delta t) \cdot \vec{v}(1.5\Delta t) \geq 0$.

We will show calculated fidelities in the next sections and compare them to experimental results. Two parameters have to be adjusted: The first is the effective coupling constant g_{eff}, which we set to $2\pi \cdot 13$ MHz. The second parameter is the temperature of the atom, i.e., the width of the Gaussian distribution. In principle, the temperature depends on the performance of the feedback and thus on the fidelity. For simplicity, we assume a fixed temperature of 200 μK - a little higher than the temperature that we determine later on for the optimal parameters. It should be mentioned that the qualitative dependence of the fidelity upon different parameters, such as the integration time, the probe power or the threshold, in which we are interested, is not very sensitive to the exact choice of the effective coupling strength and the temperature.

5.2.2 Time-Dependent Temperature

In this section, we would like to extend our simple model to describe how the feedback reduces the energy of the oscillating atom. This time, we consider only the motion in the radial direction. The potential energy of the atom at the center and at the turning point of the dipole potential is U_0 and U_1, respectively (cf. Fig. 5.2 (c)). If the feedback would work perfectly, the potential is reduced by a factor $\alpha < 1$ at the turning point of the trajectory reducing the energy by $U_1(1-\alpha)$. The potential is increased from αU_0 to U_0 at the bottom of the dipole potential raising the energy of the atom by $U_0(1-\alpha)$. In total, the atom looses an energy of $\Delta E = (1-\alpha)E$ per half oscillation period where E is the initial energy. In practice, we only estimate the velocity correctly with the probability p. If we estimate the velocity incorrectly, the switching of the dipole trap increases the energy of the atom. Thus, the average energy loss per half an oscillation period is expected to be

$$\begin{aligned} \Delta E &= -p(1-\alpha)E + (1-p)(1-\alpha)E \\ &= -F(1-\alpha)E \end{aligned} \tag{5.5}$$

with the fidelity $F = 2p-1$. We assume here for simplicity that we estimate the velocity only once per oscillation period, which is of course not really correct. In practice, the direction of the velocity is continuously evaluated.

Next, we consider an average over atoms with a thermal energy distribution. We assume that Eq. 5.5 is also valid for the change of the average energy and thus the temperature of the thermal distribution. This enables us to write down a differential equation for the time evolution of the temperature:

$$\frac{\partial T(t)}{\partial t} = \frac{2\Delta T\omega}{2\pi} + D = -\frac{2F(1-\alpha)\omega T(t)}{2\pi} + D = -\gamma T(t) + D \tag{5.6}$$

where $\omega/2\pi$ is the oscillation frequency of the atom in the trap. Furthermore we have introduced here some additional constant heating rate, D, independent of the energy (i.e., temperature) of the atom. This could be heating due to spontaneous emission, dipole force fluctuations, parametric heating or any other typical heating source. Note that in principle the fidelity, F, and thus the cooling rate, γ, is expected to depend on the temperature. However, if the temperature changes are not too big, we can assume that F is constant. In this case, we can directly give a solution for the time evolution starting from an initial temperature T_0:

$$T(t) = \exp(-\gamma t)\left(T_0 - \frac{D}{\gamma}\right) + \frac{D}{\gamma} \tag{5.7}$$

The temperature decreases exponentially with a decay rate $\gamma = 2F(1-\alpha)\omega/2\pi$. It approaches a temperature limit of D/γ.

5.3 Experimental Results

5.3.1 Experimental Implementation

A cloud of atoms is launched via the atomic fountain. Single atoms are trapped in the intracavity dipole trap by increasing the dipole trap depths from 100 μK to almost 1 mK when a drop in the probe-light transmission heralds the arrival of an atom from the atomic fountain. To avoid trapping multiple atoms, only a dilute atomic cloud is launched such that only in about every third launch an atom is detected. The transmitted light is registered by four single-photon counting modules. Upon the detection of a photon, they generate digital pulses that are processed by a FPGA (FlexRio, Natinal Instruments) [17]. It evaluates the number of photons during two successive intervals, N_1 and N_2, with a fixed duration δt with an update rate of a few tens of ns. Then, it compares the difference between the two count rates with the threshold, N_{th}, and outputs the result of the comparison to a digital channel. According to the value of this digital channel the power of the dipole trap is switched to the high or low value. As the dipole trap laser is also used to stabilize the cavity length, the attenuation of the back reflected light from the cavity by the electro-optical amplitude modulator in its path has to be adjusted synchronously to keep the amplitude of the Pound-Drever-Hall error signal that is used for the cavity lock constant (cf. Fig. 3.14). After the digital channel is switched, it takes approximately 10 μs until the power of the dipole trap has settled to its final value. This includes a 4 μs delay of the analog switching and 6 μs needed by the PID-controller to adjust the intensity to the desired value.

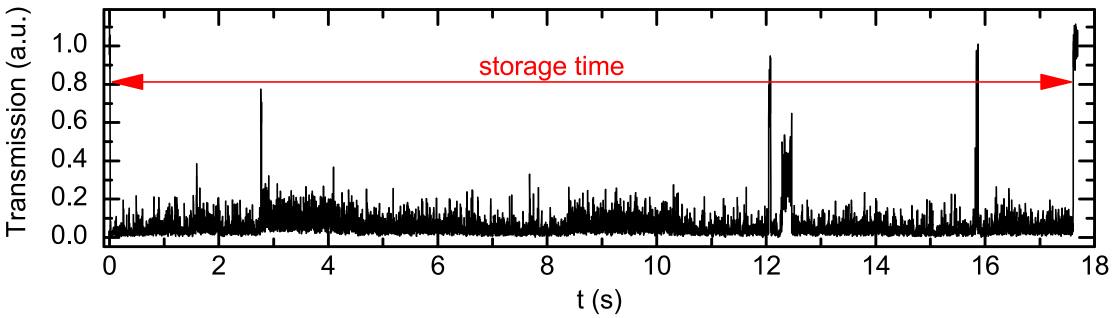

Figure 5.3: Sample transmission trace of a trapped atom. The atom is detected at t=0 by the drop in the transmission. The dipole trap is switched on, and the feedback is activated. The escape time of the atom is determined from the jump in the transmission back to the empty-cavity value.

To compensate for off-resonant scattering to the F=2 hyperfine ground state, which occurs at a small rate of about 12 Hz due to non-perfect circular polarizations and residual magnetic fields, we employ a weak re-pumping laser perpendicular to the cavity axis. This laser is not mandatory for feedback cooling, but it allows us to observe storage times exceeding 80 ms.

5.3.2 Storage Time

The simplest way to characterize the performance of the feedback is to analyze the storage time of the atoms in the dipole trap. The storage time of an individual atom is determined by evaluating when the transmission jumps back to the empty cavity value (cf. Fig. 5.3 for a sample trace).

For a given parameter set, the storage time of 200 individual atoms is evaluated and the fraction of atoms that has remained trapped until a time t is calculated (cf. Fig. 5.4). We fit an exponential $p(t) = Ae^{-t/\tau}$ to these curves with the amplitude, A, and the $1/e$ storage time, τ, as fit parameters. Some atoms (about 10-30%) leave the trap within the first time bin thereby reducing the amplitude to 0.7-0.9, likely because they are not trapped at all or they are trapped at a position where the trap and probe modes do not overlap and the feedback does not work properly.

In the following, we present measurements of the storage time as a function of different parameters, namely the detection efficiency, the probe power, the integration time and the threshold N_{th}. These measurements serve to optimize the feedback parameters and to understand its limitations. Moreover, comparison with our theoretical model confirms the importance of information for the performance of the feedback loop.

Storage Time versus Detection Efficiency

As illustrated in Fig. 5.4, feedback leads to a dramatic increase of the average storage time. At a probe power of P=0.1 (corresponding to 0.1 photons in the empty cavity), we determine a $1/e$ storage time of 35 ms without feedback. With feedback (integration

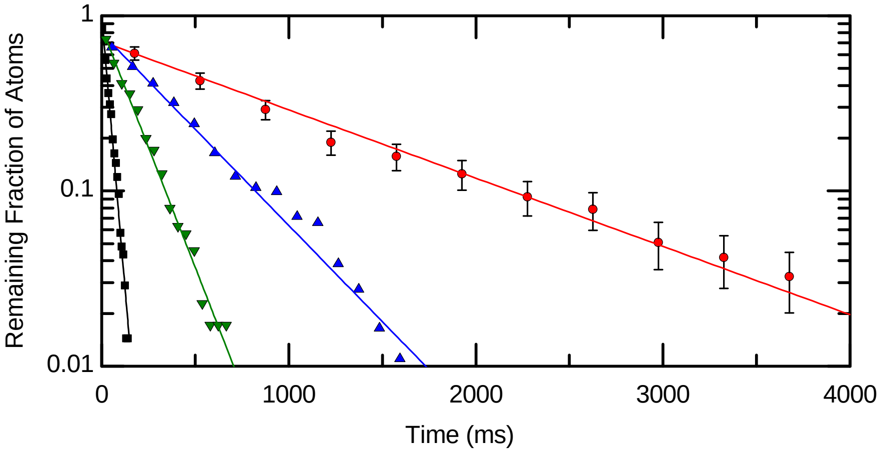

Figure 5.4: Evolution of the probability of an atom to remain trapped without feedback (■, black) and with feedback for 25 % (▼, green), 50 % (▲, blue) and 100 % (●, red) signal. The 1/e storage times are 35 ms, 160 ms, 400 ms and 1100 ms, respectively. For clarity, error bars are only shown for one curve.

time 13 μs), the $1/e$ storage time increases by a factor 30 to 1100 ms with individual atoms staying more than 17 s (cf. Fig. 5.3).

The significant improvement compared to our earlier work [11] is mainly a consequence of the higher detection efficiency of the new setup. It has been enhanced by almost a factor 5 due to the use of an asymmetric cavity and an improved detection setup. The better signal-to-noise ratio enables a more reliable position measurement at lower probe powers where less heating occurs.

The significance of a high detection efficiency is highlighted by two other measurements also shown in Fig. 5.4. When we artificially reduce the detection efficiency by attenuating the transmitted probe light by 50 % and 75 %, we observe a decrease of the storage time in proportion to the attenuation.

Storage Time versus Probe Power

Our previous observation seems to indicate that an even better performance can be achieved for a larger probe power. However, as this also leads to more heating of the atom, one has to find a compromise between a high signal and a low heating rate. This is shown in Fig. 5.5 where we have plotted the $1/e$ storage time versus the impinging probe power with and without feedback. The probe power is given in units of photons in the empty cavity. The integration time is fixed to 13 μs.

We first discuss the storage time dependence without feedback. In this case, we observe a decrease of the storage time with increasing probe power, P, which can be attributed to radial momentum diffusion. As the corresponding heating rate is determined by the atomic excitation, which is proportional to P, we can fit a $\frac{a}{P}$ function with the fit parameter a to the storage time for probe powers $P > 0.05$ photons (solid red line, cf. [13, 18]). The deviation of the storage times from this fit for very low probe powers is in agreement with previous studies. These have shown that, eventually, cavity cooling along the cavity axis can no longer compensate for axial parametric heating caused by intensity fluctuations of the dipole trap and other axial heating mechanisms.

By applying feedback, we observe an increase of the storage time by more than one order of magnitude over a broad range of powers with a peak at a probe power of P=0.1 photons where the improvement is 30-fold. At low powers, we observe a sharp increase in the storage time, which can be explained by the improved velocity estimation due to the stronger signal. For higher powers, the quality of the velocity estimation saturates and can no longer fully compensate for the increase in radial heating that causes a reduction of the average storage time.

This interplay between the improvement of the feedback performance due to the increase of the fidelity in the velocity estimation and the increasing heating rate is reflected by the temperature limit D/γ that was derived in Section 5.2.1. We recall that D is the heating rate of the trapped atom. For our parameters, it is expected to be dominated by radial momentum diffusion increasing linearly with the probe power. γ is the feedback cooling rate. In our simple model, it was found to be proportional to the fidelity, $F(P)$, of our velocity estimation, which also depends on the input power. In total, we thus expect that the temperature limit scales with $P/F(P)$. The exact relationship between the atomic temperature and the storage time is not trivial. However, it is reasonable to assume that an increasing storage time signals a lower temperature. This implies that the power dependence of the storage time can be qualitatively reproduced by the inverse temperature limit, i.e., $F(P)/P$. This quantity is plotted as a dotted blue line in Fig. 5.5 (note the different scaling of the axes) and does indeed reproduce qualitatively the most important features observed in the experiment, namely, the increase at low powers due to the better signal, the maximum at a position of about $P = 0.1$ and the decrease at higher powers due to the increase in the heating rate.

Storage Time versus Integration Time

In Fig. 5.6, we have plotted the storage time with feedback (•) as a function of the integration time, Δt, for a probe power of 0.08 photons. The storage times without feedback is plotted as a horizontal line. As one directly sees, the performance of the feedback depends critically on the integration time. We observe an increase of the storage time to a maximum at an integration time of about 15 μs and a decrease below the storage time without feedback (horizontal line) for integration times above 35 μs.

This behavior can be understood by considering the integration time dependence of the fidelity. The integration time influences the fidelity of the velocity estimation in two ways. On the one hand, a longer integration time increases the signal reducing the shot noise and thus increasing the fidelity. One the other, the time delay introduced by the integration time can cause an incorrect velocity estimation reducing the fidelity. We can expect that, for short integration times, the fidelity is dominated by shot noise and therefore increases with the integration time, whereas the delay becomes more and more important for longer integration times and, eventually, reduces the fidelity.

This assumption is confirmed by the dashed line in Fig. 5.6 (a) showing the calculated fidelity, F, versus the integration time, Δt. We find qualitative agreement with the experimental storage times. At first the fidelity increases due to the improved sig-

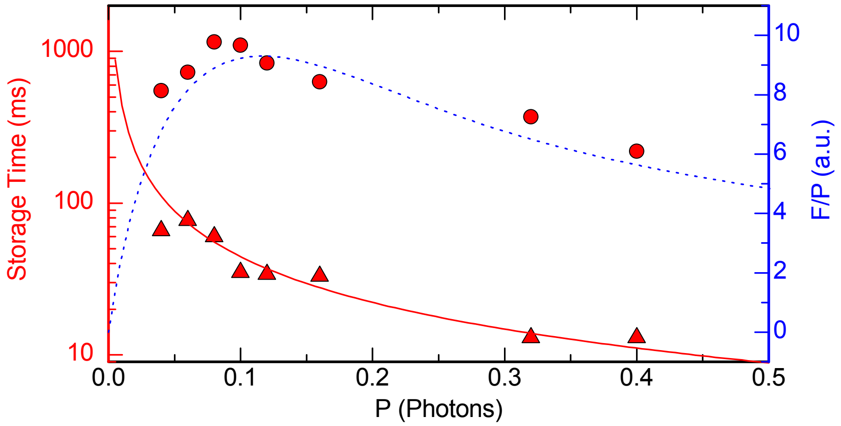

Figure 5.5: Storage time with (●, left axis) and without (▲, left axis) feedback versus probe power in units of photons in the empty cavity. The error bars are smaller than the symbols. Without feedback, the storage time is mostly limited by radial momentum diffusion as confirmed by the $T_{rad} = \frac{a}{P}$ fit (red line, left axis). With feedback, an increase of the storage time by more than one order of magnitude is observed for a broad range of probe powers. The maximum occurs as a compromise between a low radial heating rate and a good information rate. This is reflected by ratio of fidelity and heating rate, F/P (dashed blue line, right axis), which qualitatively reproduces the power dependence of the storage time.

nal, it reaches a maximum and then decreases because of the large delay introduced by the integration time. Eventually, it even becomes negative meaning that our feedback algorithm is expected to be inverted, that is to reduce the average storage times as it is confirmed in the experiment.

A detailed discussion of the dependence of the storage time upon the integration time can also be found in [11, 16].

Storage Time versus Feedback Threshold

It was already mentioned that the dipole potential is switched to a high value when the difference between the number of photons that is detected during the later time interval, N_2, and the number of photons that is detected during the earlier time interval, N_1, is greater or equal to some integer threshold N_{th}, i.e., when $N_2 \geq N_1 + N_{\text{th}}$. Monte-Carlo simulations have shown that, in particular, the choice between $N_{\text{th}} = 0$ and $N_{\text{th}} = -1$, is quite critical for the performance of the feedback [12].

This prediction is confirmed by Fig. 5.6 (b) showing the average storage time as a function of N_{th} (●, left axis). The most important conclusion is that the threshold should be zero or negative. In other words: if the transmission does not change, it is advisable to switch the potential to the high value. In fact, for positive thresholds, a reduction of the average storage time compared to the situation without feedback is observed. The longest storage time is found at a threshold of -1, which is the value used for all other experiments described in this chapter.

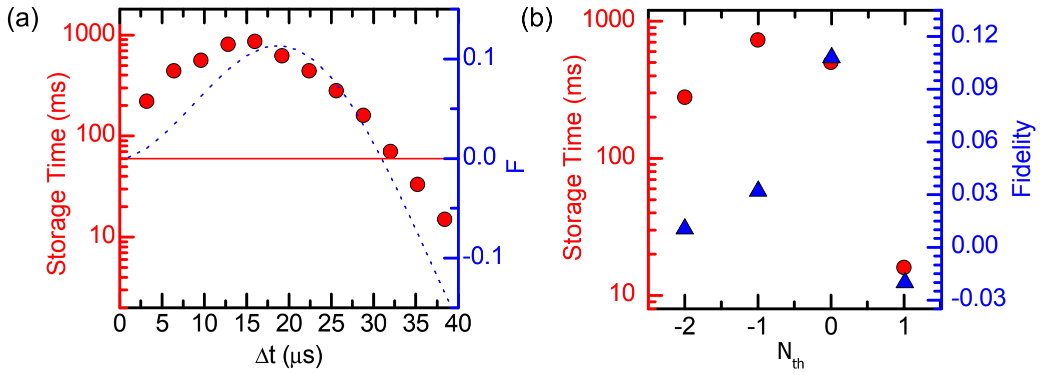

Figure 5.6: (a) Experimental storage time versus integration time, Δt (•, red, left axis). The horizontal line indicates the average storage time without feedback for the given parameters. The fidelity, F, calculated with the simple model introduced in Section 5.2.1 (dashed blue line, right axis), qualitatively reproduces the integration-time dependence of the storage time. (b) Storage time (•, left axis) and fidelity (▲, right axis) as a function of the feedback threshold which determines when the dipole potential is switched (high potential for $N_2 - N_1 \geq N_{\mathrm{th}}$). Feedback cooling only works for negative thresholds, whereas a reduction of the storage time and a negative fidelity is observed for positive thresholds. While the fidelity has a maximum at zero, in practice, an even better performance, in terms of the storage time, is achieved for a threshold of -1. A possible explanation is that one avoids heating due to frequent switching of the dipole potential.

For a better understanding, we incorporate the effect of this threshold into our calculations of the fidelity. To be more precise, we now calculate the probability that the atom is moving outwards and $N_2 \geq N_1 + N_{\mathrm{th}}$ and the probability that the atom is moving inwards and $N_2 < N_1 + N_{\mathrm{th}}$. Results are also shown in Fig. 5.6 (b) (∘, right axis). The reduced storage time at $N_{\mathrm{th}} = 0$ can be explained by the negative fidelity corresponding to an inverted feedback. However, in contrast to the storage time, the fidelity has a clear maximum at $N_{\mathrm{th}} = 0$ and drops quite significantly for smaller thresholds. A possible explanation for this discrepancy is that the frequent switching of the dipole potential that occurs for $N_{\mathrm{th}} = 0$ has additional harmful consequences independent of the fidelity. First, it causes additional parametric heating in the axial direction. Second, in the low trapping potential a loss of the atom is more likely. As a consequence, it is advantageous to keep the atom by default in the deep potential and only switch to the shallow potential when we are absolutely sure that the atom is moving inwards.

5.3.3 Temperature

We use a similar technique as in Ref. [19] to obtain a temperature estimate of the atom. The basic ideas is to lower the potential depth linearly and observe when the atom escapes (cf. Fig. 5.7 (a)). From the escape time one can reconstruct the initial energy of the atom. Repeating this measurement many times yields the energy distribution, which is expected to correspond to a Boltzmann distribution.

One has to take into account that the lowering process changes the energy of the trapped atom. It has been shown in [19] that, for an adiabatic lowering, the action of the atom, $S(E,U) = 4\int_0^{x_{max}} 2m\sqrt{E - V(x,U)}dx$, is conserved. Here, E designates the energy, x_{max} the oscillation amplitude and $V(x,U) = -Ue^{-x^2}$ a Gaussian potential with depth U. Solving numerically the equation $S(E_0, U_0) = S(U_{esc}, U_{esc})$ yields the initial energy, E_0, of an atom escaping at a potential depth of U_{esc}. Repeating this measurement for many atoms, we partly reconstruct the atomic energy distribution. In the experiment, the potential depth is lowered linearly from 950 μK to 100 μK within 4 ms. Fig. 5.7 (b) shows the reconstructed energy distribution for atoms that were trapped for 10 ms with the feedback enabled and disabled immediately before the potential was ramped down (probe power 0.1 photons, integration time 13 μs). It is clear from the figure that with feedback fewer atoms have a high energy, indicating a lower temperature. The low-energy part of the distribution was not observed because a further reduction of the final potential made our cavity lock unstable. For a more quantitative analysis, we fit the Boltzmann distribution of a 3D harmonic oscillator, $p(E)dE = N\frac{E^2}{2(k_BT)^3}e^{-\frac{E}{k_BT}}dE$, to the data. As only atoms with an energy smaller than the trap depth, U_0, are trapped, the energy distribution that we measure is normalized such that $\int_0^{U_0} p(E)dE = 1$. The only fit parameter is the temperature, T, which is found to be 160±5 μK with the feedback enabled and 400±50 μK without feedback where the errors are only due to the fit uncertainty. The observed temperature with feedback cooling is comparable to the radial temperature of $T \leq 200\mu K$ that has been observed using optical molasses cooling in a state-insensitive trap inside a high-finesse cavity [14, 20].

Note that our temperature measurements suffer from a few systematic uncertainties. First, the assumed distribution is strictly valid only in a harmonic potential. However, without feedback, the high temperature brings the atom into the anharmonic part of the potential. Second, heating effects during the ramp are neglected. Third, thermalization in three dimensions is assumed. This is not obvious as the cooling forces in the radial and axial direction are quite different.

5.3.4 Time-Dependent Temperature

In Section 5.2.2, we have made a prediction about the time evolution of the temperature and the temperature limit in the presence of feedback cooling that we would like to test. For this purpose, we trap an atom, and we disable and enable the feedback iteratively for 8 ms and 16 ms, respectively, switching to the deeper trapping potential of 950 μK when the feedback is disabled. The time-dependent transmission of the probe light in each of the two intervals is averaged over many intervals from hundreds of individually trapped atoms. To exclude intervals where the atom is leaving, we require the transmission during the two intervals and the following interval to be less than 90 % of the empty-cavity transmission. We convert the transmitted power to a temperature by assuming a thermal distribution of the atoms in the dipole trap and calculating the expected transmision as a function of the temperature (cf. Appendix B for details). We repeat the same measurement for three different attenuations of the transmitted light (probe

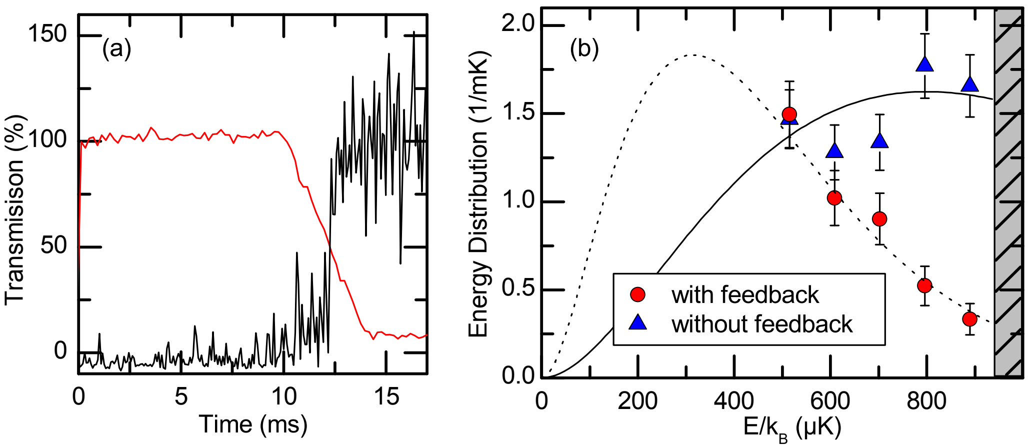

Figure 5.7: (a) Principle of the temperature measurement: Atoms are trapped for 10 ms while the feedback is either enabled or disabled. The dipole potential (red line) is ramped down within 4 ms. From the sudden jump of the probe light transmission (black line) the escape time and thus the initial energy of the atom can be reconstructed. (b) Repeating this for many atoms enables us to reconstruct a part of the atomic energy distribution. A fit of a three-dimensional Boltzmann distribution yields temperatures of 160±5 μK with the feedback enabled (•, red) and 400±50 μK without feedback (▲, blue).

power of 0.1 photons, integration time 13 μs).

Experimental results are shown in Fig. 5.8. The time dependence agrees qualitatively with our expectations. We see a linear increase in the temperature when the feedback is disabled. This observation supports our assumption that, in the absence of feedback, there is a constant heating mechanism. Moreover, the temperature decreases exponentially when the feedback is enabled as predicted by our simple model in Section 5.2.2. We determine the heating rate, D, and the cooling rate, γ, by applying a linear ($T(t) = T_0 + Dt$) and exponential fit ($T(t) = T_0 + A\exp(-\gamma t)$) to the first and second interval, respectively (solid lines).

We find an constant heating rate, almost independent of the detection efficiency, with an average of $D = (4.4 \pm 0.4)$ μK/ms. When the feedback is enabled, a sudden jump in the transmission is observed. It is caused by the changing AC-Stark shifts when the feedback is enabled. This results in a jump of the average atom cavity-detuning increasing the average transmission. Because of this effect, we systematically overestimate the temperature when the feedback is enabled. The magnitude of this systematic error can be estimated from the offset that occurs when the feedback is enabled.

From our model, we would expect that the cooling rate, γ, increases with higher detection efficiency. However, in practice, all three decay rates agree within the measurement uncertainties and we find an average cooling rate of ($\gamma = 0.55 \pm 0.05$) kHz. A possible explanation is that the increase of the fidelity due to the higher detection efficiency is counteracted by the better localization and thus lower transmission signal. As a check for consistency, we can use the equation $\gamma = 2F(1-\alpha)\omega/2\pi$ to estimate the experimental fidelity from the cooling rate that we find. Plugging in the numbers $\alpha \approx 0.5$ and $\omega/2\pi = 5$ kHz, we find $F = \frac{2\pi\gamma}{\omega} \approx 0.1$, which is consistent with the calculated fidelities from Section 5.3.2.

Next, we would like to discuss the temperatures. To avoid systematic errors from the fluctuating light shifts discussed before, it is advisable to evaluate the temperature at the beginning of the interval without feedback. Without attenuation, we find a temperature of 170 μK, which is in good agreement with the temperature of 160 μK that we have determined before using a completely different technique. As expected, the temperature increases when the detection efficiency decreases due to the poorer performance of the feedback. The temperatures for a detection efficiency of 50 % and 25 % are 200 μK and 230 μK, respectively.

So far, our simple model has been surprisingly successful in describing at least qualitatively most of the observations. A significant discrepancy occurs though when we calculate the expected temperature limit $T = D/\gamma$ that was derived in 5.2.2 and compare it to the observed temperature. Plugging in the heating rate, D, and the cooling rate, γ, we obtain a temperature limit of only 7 μK, which is much smaller than the value that we actually observe. This suggests that there is another limitation to the temperature that has so far not been considered. In fact, our theoretical model for the time dependence of the cooling process is restricted to one-dimensional motion only. In reality, the atom moves in three dimensions. We can decompose the motion into an axial, a radial and an azimuthal component. Cavity cooling of the probe laser acts in the axial direction. The radial motion is cooled by feedback cooling. The azimuthal motion is affected by neither of the two cooling forces, but it is also subject to momentum diffusion and therefore heating. This puts into question if the atom can really be assumed to be in thermal equilibrium. In any case, the azimuthal motion is expected to be another limiting factor for the temperature that can be achieved. In fact, this is supported by Monte-Carlo simulations that have shown that the average storage time with feedback can be increased even further by breaking the radial symmetry of the potential and thus mixing the radial and azimuthal motion [12].

5.3.5 Correlation Function

A complementary way to characterize how feedback cooling changes the atomic motion is to look at the intensity correlation function $\langle I(t)I(t+\tau)\rangle_t$ of the probe light as shown in Fig. 5.9 (probe power 0.2 photons, integration time 13 μs). To obtain these graphs we divide the experimental traces in intervals with a duration of $T = 2$ ms. For intervals with transmission below 80% of the empty-cavity transmission, we then evaluate $R(\tau) = \frac{1}{T-\tau}\int_0^{T-\tau} I(t)I(t+\tau)dt$ where $I(t)$ is the photon count rate averaged over 1 μs. We average over many intervals. The upper two curves show the average $R(\tau)$ for an atom trapped in the deep and the low trapping potential, respectively, when the feedback is disabled. Both curves have a characteristic maximum at $T_1 = 190$ μs for the deeper (b) and at $T_2 = 270$ μs for the shallower (a) potential. It is a consquence of the modulation of the transmission signal at the radial oscillation frequency [18]. The correlation function, $R(\tau)$, of atoms with enabled feedback is plotted in the lower part of the figure for integration times of the feedback algorithm of 16 μs (d) and 32

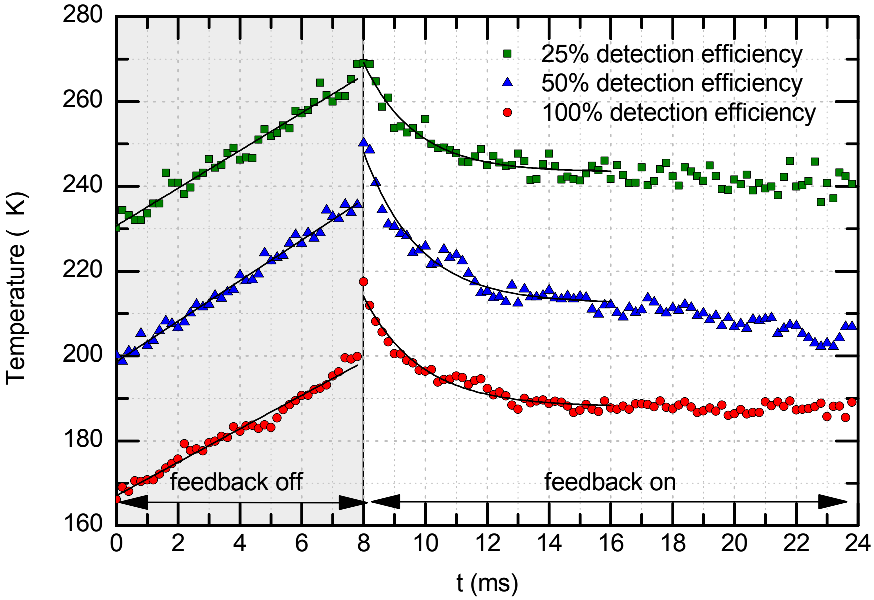

Figure 5.8: Time-dependent temperature in two successive intervals in which the feedback is disabled and enabled, respectively, for three different detection efficiencies. The temperature was calculated from a measurement of the average time-dependent transmission. Without feedback the temperature increases linearly due to radial heating. When the feedback is enabled, an exponential drop in the temperature with a $1/e$ time constant on the order of 2 ms is observed proving cooling of the atomic motion. The higher the detection efficiency the lower the steady-state temperature. The sudden jump in the temperature at the beginning of the feedback interval is an artifact due to the fluctuating Stark shift during the feedback intervals.

μs (c). Three points are noteworthy. First, the average transmission is reduced, which directly shows the better localization. Second, the radial oscillation bump is almost completely suppressed providing further evidence for a reduction of the radial oscillation amplitude due to feedback cooling. Third, an almost square-shaped feature is observed for short correlation times. Its rising edge and width are given by the integration time of the feedback algorithm. This feature is an artifact of our feedback algorithm that preferentially switches the dipole trap with a period given by the integration time. As mentioned before, the change in the light shift has an effect on the transmitted signal, which is therefore modulated at the same frequency.

5.4 Conclusion and Outlook

We have shown that feedback cooling can increase the average storage time by more than a factor of 30 and leads to an improved atomic localization of the atom in the cavity mode. These two results are of significant importance for future experiments because they imply a dramatic increase of the duty cycle of the experiment. Monte-Carlo simulations have shown that the use of a radially asymmetric potential [21] can

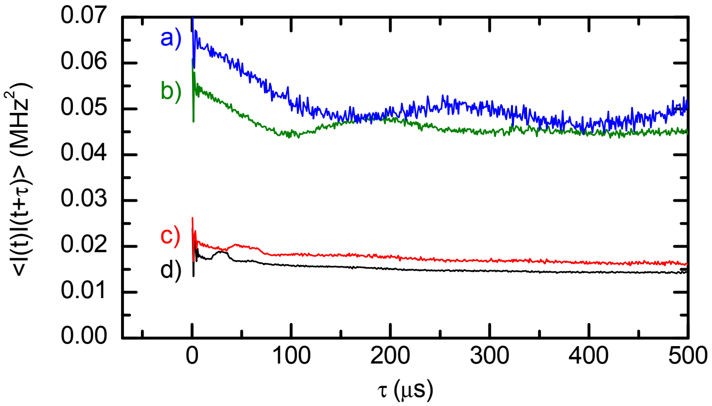

Figure 5.9: Time-dependent intensity-correlation function without feedback in the shallow (a) and deep (b) trap, and with feedback using an integration time of the feedback algorithm of 32 μs (c) and 16 μs (d). Without feedback the radial oscillations cause a characteristic bump at one-half of the oscillation period. This bump disappears when the feedback is enabled.

increase the storage time further [12] because it allows to change the angular momentum of the atom.

The temperature and storage time are comparable to what has been reported previously using conventional three-dimensional laser cooling in an intracavity dipole trap [14, 20]. Compared to experiments with atoms trapped in a transverse dipole trap [22], which have achieved longer storage times, our technique has the advantage that it does not require transverse optical access. Therefore, it can be implemented also for very short cavity lengths [7] or other resonator geometries with limited optical access, such as fiber-based cavities on atom-chips [23], bottle resonators [24] or micro-toroidal resonators [25]. Another advantage stems from the fact that, since no optical pumping transverse to the quantization (i.e., the cavity axis) is needed, the atom never leaves the closed $F = 3, m_F = +3$ to $F = 4, m_F = +4$ transition preserving its perfect two-level character. As feedback cooling does in principle not rely on photon scattering from the atom, it is particularly attractive for applications that require preservation of the atomic state.

Finally, we would like to point out that there is also a more fundamental motivation for further investigations. The behavior of thermodynamic systems in the presence of feedback has been an important question in theoretical thermodynamics for a long time. Maxwell's demon and the Szilard engine [26] are just two famous Gedankenexperiments that have been proposed in this context. Both examples are still the subject of intense theoretical [27, 28, 29, 30] but also experimental [31] investigations. In the future, our experiment might also enable us to address questions going in this direction.

Bibliography

[1] S. van der Meer, *Rev. Mod. Phys.* **57**, 689 (1985).

[2] B. D'Urso, B. Odom, and G. Gabrielse, *Phys. Rev. Lett.* **90**, 043001 (2003).

[3] N. Guise, J. DiSciacca, and G. Gabrielse, *Phys. Rev. Lett.* **104**, 143001 (2010).

[4] P. Bushev, D. Rotter, A. Wilson, F. Dubin, C. Becher, J. Eschner, R. Blatt, V. Steixner, P. Rabl, and P. Zoller, *Phys. Rev. Lett.* **96**, 043003 (2006).

[5] P. Münstermann, T. Fischer, P. W. H. Pinkse, and G. Rempe, *Opt. Comm.* **159**, 63 (1999).

[6] C. J. Hood, M. S. Chapman, T. W. Lynn, and H. J. Kimble, *Phys. Rev. Lett.* **80**, 4157 (1998).

[7] C. J. Hood, T. W. Lynn, A. C. Doherty, A. S. Parkins, and H. J. Kimble, *Science* **287**, 1447 (2000).

[8] P. W. H. Pinkse, T. Fischer, P. Maunz, and G. Rempe, *Nature* **404**, 365 (2000).

[9] T. Fischer, P. Maunz, P. W. H. Pinkse, T. Puppe, and G. Rempe, *Phys. Rev. Lett.* **88**, 163002 (2002).

[10] T. W. Lynn, K. Birnbaum, and H. J. Kimble, *J. Opt. B* **7**, 215 (2005).

[11] A. Kubanek, M. Koch, C. Sames, A. Ourjoumtsev, P. W. H. Pinkse, K. Murr, and G. Rempe, *Nature* **462**, 898 (2009).

[12] A. Kubanek, M. Koch, C. Sames, A. Ourjoumtsev, T. Wilk, P. Pinkse, and G. Rempe, *Applied Physics B: Lasers and Optics* **102**, 433 (2011):

[13] P. Maunz, T. Puppe, I. Schuster, N. Syassen, P. W. H. Pinkse, and G. Rempe, *Nature* **428**, 50 (2004).

[14] A. Boca, R. Miller, K. M. Birnbaum, A. D. Boozer, J. McKeever, and H. J. Kimble, *Phys. Rev. Lett.* **93**, 233603 (2004).

[15] P. Maunz, T. Puppe, I. Schuster, N. Syassen, P. W. H. Pinkse, and G. Rempe, *Phys. Rev. Lett.* **94**, 033002 (2005).

[16] A. Kubanek, *Two-photon gateway and feedback control of a single atom in a cavity*, PhD thesis, Technische Universität München (2010).

[17] C. Sames, M. Balbach, M. Koch, A. Kubanek, P. Pinkse, and G. Rempe, FPGA-based Feedback Control of a Single Atom Trajectory, in *Virtuelle Instrumente in der Praxis 2010*, edited by R. Jamal and R. Heinze, pp. 315–320, VDE Verlag, Berlin (2010).

[18] P. Maunz, *Cavity cooling and spectroscopy of a bound atom-cavity system*, PhD thesis, Max-Planck-Institut für Quantenoptik und Technische Universität München (2004).

[19] W. Alt, D. Schrader, S. Kuhr, M. Müller, V. Gomer, and D. Meschede, *Phys. Rev. A* **67**, 033403 (2003).

[20] A. D. Boozer, A. Boca, R. Miller, T. E. Northup, and H. J. Kimble, *Phys. Rev. Lett.* **97**, 083602 (2006).

[21] T. Puppe, I. Schuster, A. Grothe, A. Kubanek, K. Murr, P. W. H. Pinkse, and G. Rempe, *Phys. Rev. Lett.* **99**, 013002 (2007).

[22] S. Nussmann, K. Murr, M. Hijlkema, B. Weber, A. Kuhn, and G. Rempe, *Nature Physics* **1**, 122 (2005).

[23] R. Gehr, J. Volz, G. Dubois, T. Steinmetz, Y. Colombe, B. L. Lev, R. Long, J. Estève, and J. Reichel, *Phys. Rev. Lett.* **104**, 203602 (2010).

[24] M. Pöllinger, D. O'Shea, F. Warken, and A. Rauschenbeutel, *Phys. Rev. Lett.* **103**, 053901 (2009).

[25] T. Aoki, B. Dayan, E. Wilcut, W. P. Bowen, P. A. S., T. J. Kippenberg, K. J. Vahala, and H. J. Kimble, *Nature* **443**, 671 (2006).

[26] L. Szilard, *Z. Phys.* **53**, 840 (1929).

[27] K. Jacobs, *Phys. Rev. A* **80**, 012322 (2009).

[28] T. Sagawa and M. Ueda, *Phys. Rev. Lett.* **100**, 080403 (2008).

[29] K. Maruyama, F. Nori, and V. Vedral, *Rev. Mod. Phys.* **81**, 1 (2009).

[30] T. Sagawa and M. Ueda, *Phys. Rev. Lett.* **104**, 090602 (2010).

[31] S. Toyabe, T. Sagawa, M. Ueda, E. Muneyuki, and M. Sano, *Nature Phys.* **6**, 988 (2010).

Chapter 6

Quantum Dynamics - Correlation Functions

The content of this chapter has partially been published in:
M. Koch, C. Sames, B. Balbach, H. Chibani, A. Kubanek, K. Murr, T. Wilk, and G. Rempe, *"Three-Photon Correlations in a Strongly Driven Atom-Cavity System"*, Physical Review Letters **107**, 023601 (2011).

Contents

In the previous chapter, we have seen that the transmitted probe light carries information about the classical trajectory of the atom. We have used this information to control the motion of the atom by means of feedback. This naturally raises the question whether similar techniques can be employed to observe and eventually control the quantum trajectory of the internal degrees of freedom of the strongly coupled atom-cavity system.

Before going into details, we would like to remind the reader of the fundamental difference between the observation of the dynamics of a classical system and a quantum system. In the first case, the dynamics and its observation can be treated in principle completely independent. The trajectory can be determined with an accuracy which is only limited by technical constraints, such as noise in the detectors or thermal fluctuations. For a quantum system, the situation is quite different: The act of observing the system causes a collapse of the wavefunction and thus alters the dynamics of the system. Noise and fluctuations are not brought to the system by some external perturbation, but they are intrinsic to the observation process.

This is nicely illustrated in Fig. 6.1 (cf. [1] for similar calculations), which shows a sample quantum trajectory of the average photon number $\langle a^\dagger a \rangle$ in a strongly driven atom-cavity system. One observes the coherent, and therefore reversible, evolution of the system induced by the driving and the exchange of energy between the atom and the cavity. This evolution is interrupted by sudden quantum jumps when a photon is spontaneously emitted from the atom ($\triangledown$) or escapes from the cavity ($\blacktriangle$). The main purpose of this chapter is to investigate how the fundamental dynamical processes visible in such a caclulated quantum trajectory can be reconstructed from the seemingly random stream of photons ($\blacktriangle$) emitted from the cavity.

At first sight, this seems difficult, since, by the very definition of strong coupling, the rate at which photons are emitted is smaller than the typical timescales of the dynamics that we are interested in. The solution is the evaluation of time-dependent correlation functions of the emitted light field, such as the second-order correlation function $g^{(2)}(\tau)$ measuring the average time evolution of $\langle a^\dagger a \rangle$ conditioned upon a quantum jump due to cavity decay. In view of the prominent role the second-order correlation function plays in quantum optics, it is not surprising to find out that it has been studied before also in the field of cavity QED. However, compared to previous experiments [2, 3, 4, 5], we perform the experiments in the strong-driving regime. This gives rise to new dynamical effects due to the coherent coupling of the system with the probe laser. As another consequence of the strong driving, the quantum trajectory of the system also includes higher-order dressed states of the Jaynes-Cummings ladder, leading to the emission of characteristic patterns of multiple-photon emissions [6]. We characterize these via the third-order intensity correlation function. While the second-order correlation function is naturally symmetric in time, the third-order correlation function enables us also to address the simple but experimentally unexplored question whether the emitted photon stream is symmetric in time. In contrast to second-order correlation functions, time-dependent third-order correlation functions have hardly been studied at all. Notable exceptions are early investigations of laser light near threshold [7, 8] and non-Gaussian scattering processes in diffusive media [9].

6.1 Measurement Procedure

The strong driving leads to strong heating and therefore very short storage times and a low duty cycle of the experiment. Therefore, we perform the measurements with atoms passing through the cavity mode, launched via the atomic fountain from underneath

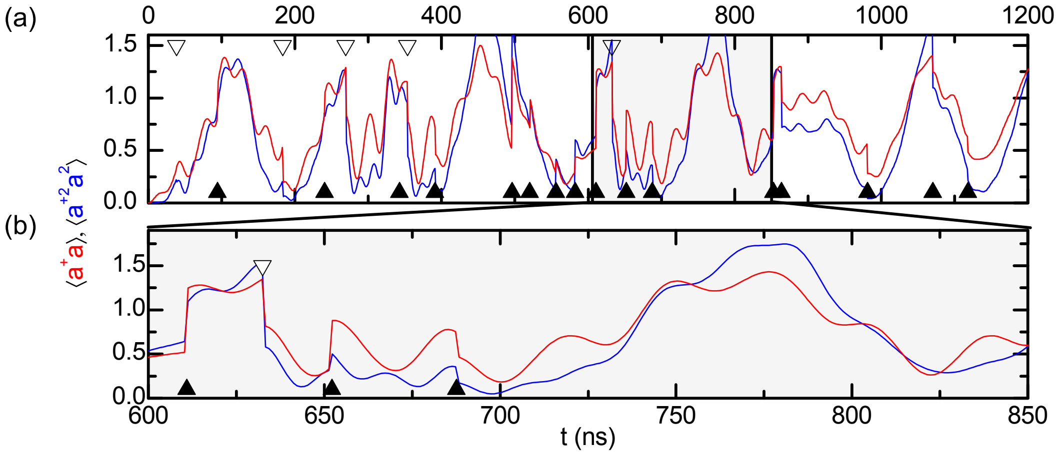

Figure 6.1: (a) Quantum trajectory of the average photon number $\langle a^\dagger a\rangle$ (red) and the two photon emission probability $\langle a^{\dagger 2}a^2\rangle$ (blue) for typical experimental parameters ($g/2\pi$ = 14.5 MHz, $\Delta_a/2\pi = \Delta_c/2\pi = -12$ MHz, $\eta = 3.5\kappa$). We observe coherent oscillations at different frequencies interrupted by unpredictable quantum jumps due to cavity decay (▲) or spontaneous emission (▽). (b) A zoom into a part of the trajectory shows fast oscillations at different timescales for the two observables. Note that the annihilation of a photon can increase or decrease the average photon number in the cavity depending on whether the photon distribution of the state at the given instant is super- or sub-Poissonian.

the cavity. The transit time of an individual atom is adjusted to be about 20 μs. The attractive potential induced by the weak stabilization laser at 785 nm guides the passing atoms towards regions of strong coupling. With a detuning of the probe laser with respect to the cavity of $\Delta_c/2\pi$ = -12 MHz, near resonant with the lower-frequency normal mode, a transient atom causes an increase of the probe light transmission, cf. Fig. 6.2 (a) and (b). We evaluate the recorded photon clicks only in those intervals where the transmission is increased by at least a factor of 1.6 compared to the empty-cavity value. In each launch about 25 atoms cause such an increase. In the presence of an atom, the probability of having a second atom in the cavity is less than 3 %.

6.2 Second-order Correlation Function

First, we consider the time evolution of the average photon number shown as a red line in the quantum trajectory in Fig. 6.1 (a) and (b). Two characteristic frequencies are visible, a slow oscillation with a period of about 150 ns and a fast oscillation with a period of about 30 ns. To observe these in the experiment, we evaluate the second-order correlation function,

$$g^{(2)}(\tau) = \frac{\langle a^\dagger a^\dagger(\tau)a(\tau)a\rangle}{\langle a^\dagger, a\rangle^2} \tag{6.1}$$

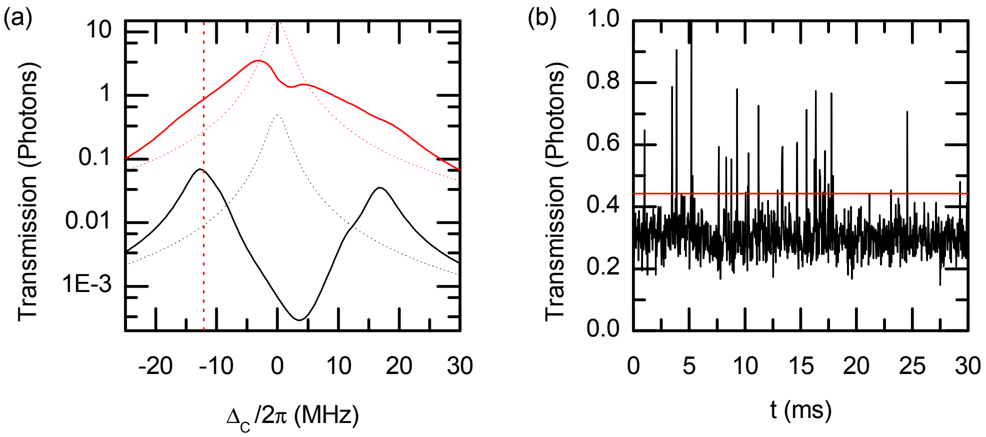

Figure 6.2: (a) Theoretical transmission spectrum for a fixed atom ($g/2\pi$ = 14.5 MHz, 4 MHz AC-Stark shift) for weak driving (η=0.7κ, solid black line) and the strong driving used in these experiments (η=3.9κ, solid red line). For comparison, the empty-cavity spectra (dashed lines) are also plotted. For most of the experiments described in this chapter, a detuning of $\Delta_c/2\pi = -12$ MHz (vertical dashed line), close to resonance with the $|1-\rangle$ state, was used. (b) Typical experimental trace of the cavity transmission when a dilute cloud of atoms is passing through the cavity (η=4.06κ, $\Delta_c/2\pi = -12$ MHz). The passage of a single atom causes an increase of the transmission. For the evaluation of the correlation functions, only those intervals where the average transmission exceeds a certain threshold (horizontal red line) are taken into account.

of the transmitted probe light, measuring the conditional evolution of the average photon number after the detection of a photon. Details on the evaluation and normalization of the correlation function can be found in Appendix C. Experimental results are plotted in Fig. 6.3 (a) for different driving strengths (black). Deviations of the asymptotic values from 1 result from the variation of the transmitted intensity during the passage of an atom through the cavity mode. This effect has been widely studied and is well understood [2, 3, 4, 10].

We observe a relaxation of the correlation function to the constant asymptotic value on a timescale determined by the dissipation rates of the system. Within this duration, oscillations at two very different timescales are visible. For a more quantitative analysis, we fit a phenomenological exponentially damped, oscillating function [1] to the data. It provides us with the two characteristic frequencies ω and Ω and the relaxation rate λ to be discussed in the next sections.

Theoretical calculations are shown in red in Fig. 6.3 (a). They are in excellent agreement with our experimental results. Since the atomic transit happens on a much longer timescale than the internal dynamics, we can account for it in the theory by averaging the correlation function over a proper atomic position distribution. Its shape (cf. Appendix B for details) and the maximum Stark shift induced by the stabilization laser (4 MHz) were adjusted for one set of parameters and then kept constant for all the

---

[1] $f(\tau) = e^{-\lambda\tau}(A_\omega \cos(\omega\tau) - A_\Omega \cos(\Omega\tau - \phi_\Omega)) + f_0$

measurements presented in this chapter. For each individual measurement, we use two fit parameters: First and most importantly, we adjust the size of the integration volume (cf. Appendix B) such that the asymptotic value of the correlation function matches with the experiment. Second, we have to adjust the atom-cavity detuning ($\Delta_{ac}/2\pi$) by up to 2.2 MHz (between 0 and -2.2 MHz) probably due to electronic offset drifts of the probe-laser frequency lock during the days or weeks that lay between these individual measurements.

In contrast to our first theoretical analysis in [11] and previous measurements of correlation functions with passing atoms [5, 10], no vertical scaling is required to match experimental data and theory. The reason for this improved agreement between theory and experiment is a careful recalibration of the probe power based on the measured empty-cavity transmission. With these corrected values of driving strength, η, which deviate by at most 5 % compared to the values cited in [11], and a reduction of the Stark-Shift from 5 MHz to 4 MHz, we are now able to reproduce also the absolute values of the measured correlation functions.

6.2.1 Vacuum Rabi Oscillations

The obtained frequencies ω and Ω are plotted in Fig. 6.3 (b) as a function of the driving strength η. The faster modulation of the correlation function at ω is a consequence of the vacuum Rabi oscillations, i.e., the coherent exchange of a single excitation between atom and cavity. For a qualitative understanding, we recall that we drive the system close to resonance with the lower-frequency normal mode $|1-\rangle$. Due to the anharmonicity of the Jaynes-Cummings ladder, we are thus detuned from the $|2-\rangle = (|2g\rangle - |1e\rangle)/\sqrt{2}$ state. However, there is alway some off-resonant excitation to this state as well. On short timescales where the effects of the driving can be neglected, only this state (and of course the even less occupied higher dressed-states) can give rise to the emission of two photons. It is therefore reasonable to assume that the time evolution of the average photon number on short timescales is dominated by the steady-state population of the $|2-\rangle$ state. The annihilation of the first photon that triggers the measurement projects this state onto $(\sqrt{2}|1g\rangle - |0e\rangle)/\sqrt{3}$, which is not an eigenstate of the system. As a consequence, the system oscillates between the two states with a single excitation at the vacuum Rabi frequency of $2g$. This is consistent with our observation of an almost constant frequency, ω, with an average of $\bar{\omega}/2\pi = 29\,\mathrm{MHz}$ (dashed blue line) close to the expected maximum value of $2g_0/2\pi = 32$ MHz. The reduction of 10% can be attributed to the averaging over different coupling strengths due to the atomic motion.

Even though vacuum Rabi oscillations have been observed directly in several microwave experiments before [12, 13, 14, 15], there is far less experimental evidence in the optical domain. In particular, past experiments have either worked with ensembles of a few atoms in the cavity [2] or operated in a dispersive regime [16] where the oscillation frequency is dominated by the large atom-cavity detuning and not by the atom-cavity coupling. An observation of vacuum Rabi oscillations of a single, strongly coupled atom in the optical domain has only been achieved recently [17].

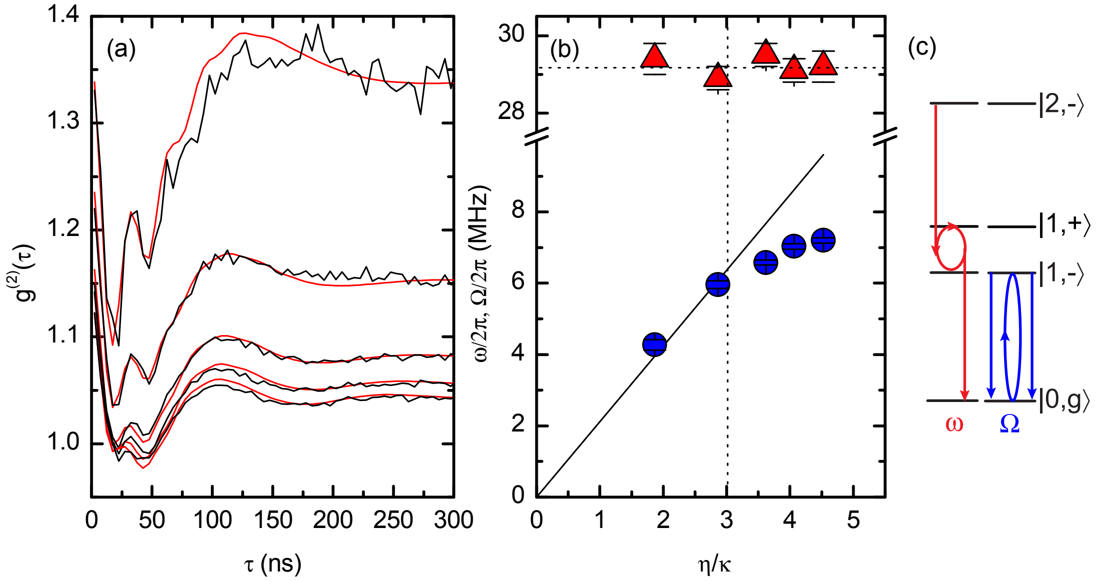

Figure 6.3: (a) Second-order intensity correlation function $g^{(2)}(\tau)$ for different driving strengths (from top to bottom η = 1.86κ, 2.86κ, 3.62κ, 4.06κ, 4.53κ) in the experiment (black) and theory (red). (b) The two oscillation frequencies ω (▲) and Ω (●) as a function of the driving strength, η. ω is constant with an average $\bar{\omega}/2\pi = 29\,\mathrm{MHz}$ (horizontal dashed line) close to the maximum vacuum Rabi frequency of $2g_0/2\pi = 32\,\mathrm{MHz}$. The super Rabi frequency Ω (cf. text for details) increases with η. Up to a driving strength of about 3κ (vertical dashed line), it can be described by a two-level model with $\Omega = \sqrt{2}\eta$ (black line). (c) The appearance of two frequencies can be understood by two different processes: Neglecting the driving on short timescales, the emission of a photon pair requires an initial occupation of the second-order dressed state. The detection of the first photon projects it onto a superposition of the first-order dressed states giving rise to vacuum Rabi oscillations in the subsequent time evolution. On longer timescales, the initial occupation of the first-order dressed state, which is projected onto the ground state, can be coherently re-excited leading to the observation of the super Rabi oscillations.

6.2.2 Super Rabi Oscillations

The strong driving gives rise to another coherent process, namely the exchange of energy between the atom-cavity system and the probe laser. This results in the second characteristic oscillation frequency Ω (● in Fig. 6.3 (b)), which depends on the driving strength. We refer to these oscillations as super Rabi oscillations. As we have discussed in detail in Section 2.2.3, due to its anharmonic energy-level structure (cf. Fig. 2.2 (c)), the system behaves at low excitation like a driven two-level system [1] when excited close to resonance with one of the normal modes. Neglecting the small atom-cavity detuning, we expect a Rabi frequency of $\Omega = \sqrt{2}\eta$ (cf. Section 2.2.3), which is plotted as a solid black line in Fig. 6.3 (b). Deviations from the two-level approximation occur when the transition to the second dressed state becomes important. This is expected for a driving strength of about 3κ, marked as a vertical dashed line. The reduction of

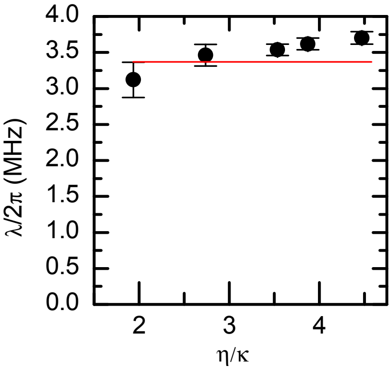

Figure 6.4: Measured relaxation rate of the second-order correlation function in comparison with the decay rate expected for a driven two-level system $\lambda = 3(\kappa + \gamma)/4$ (red line).

the oscillation frequency compared to the two-level approximation at higher powers is in agreement with previous studies of a driven anharmonic oscillator [18].

Investigations of the second-order correlation function close to resonance with the normal modes of a strongly coupled atom-cavity system have been performed before [3, 4, 5, 19]. However, the only purpose of these experiments was the observation of a photon blockade (i.e., anti-bunching) as a consequence of the anharmonic energy level structure of the coupled atom-cavity system. The driving strengths and temporal resolution were too low to observe super Rabi oscillations or vacuum Rabi oscillations in these experiments.

The name *super Rabi oscillations* that we have introduced here is motivated by the so-called *super splitting* of the normal modes observed in [20]. The magnitude of this super splitting equals twice the super Rabi frequency discussed here. The super Rabi oscillations can thus be considered as the dynamic manifestation of the super splitting. In parallel to this work, super Rabi oscillations have also been observed in another circuit QED experiment [21].

6.2.3 Dissipation

The damping of the correlation function to a constant asymptotic value reflects the relaxation of the system back to its steady-state. From the exponentially damped fit to the data, we obtain the relaxation rate λ which is plotted in Fig. 6.4 as a function of the driving strength. Of course the relaxation rate is expected to be related to the dissipation rates of the system κ and γ. However, as we cannot give an analytic expression for the correlation function, it is not straightforward to make a quantitative prediction. We have seen though that the super Rabi oscillation frequency is well explained by a two-level model at low powers. This suggests to make a comparison of the decay rate of the correlation function with the one expected for a driven two-level system. The latter can be calculated analytically [22]. For a two-level system with linewidth Λ (HWHM) driven strongly with a Rabi frequency Ω, the correlation

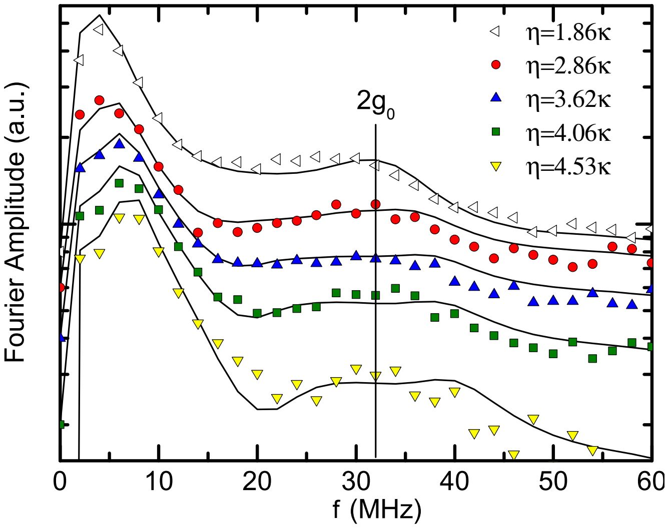

Figure 6.5: (a) Fourier spectrum of the second-order correlation function for five different driving strength (spectra are vertically offset with respect to each other for clarity) in the experiment and theory (solid lines). The super Rabi oscillations are visible as a pronounced peak at 5-10 MHz, whose maximum increases with the driving strength. Due to the position averaging, the contribution of the vacuum Rabi oscillations at about 30 MHz is significantly broadened. Nevertheless, one can identify a shift towards higher frequencies.

function is

$$g^{(2)}(\tau) = 1 - e^{-3\Lambda\tau/2}\cos\Omega\tau. \tag{6.2}$$

The relaxation rate is thus $3\Lambda/2$. In our case, the linewidth of the $|1-\rangle$ state is approximately $\Lambda = (\kappa+\gamma)/2$. The resulting decay rate of $3\Lambda/2 = 2\pi\cdot 3.4$ MHz (red line) is found to be in reasonable agreement with the measured values of λ as plotted in Fig. 6.4.

6.2.4 Fourier Spectrum

A complementary way to characterize the characteristic frequencies appearing in the second-order correlation function is to evaluate its Fourier spectrum. The result is plotted in Fig. 6.5 showing the Fourier amplitudes of the second-order correlation function (experiment and theory) at different probe powers. One can clearly identify the super Rabi oscillation frequency, Ω, at about 5-10 MHz. As discussed before, its frequency increases as the driving strength is increased.

The fast oscillation frequency, ω, is also visible as a broad spectral feature at about 30 MHz. The effect of the atomic motion, causing an averaging over different coupling constants and thus a broadening of the spectrum, is clearly visible. This makes an accurate determination of the characteristic frequency from the Fourier spectrum difficult. However, one can identify, at least qualitatively, an effect that we have overlooked in our previous discussion. In fact, the fast oscillation frequency due to the vacuum Rabi oscillations is not completely independent of the driving but also seems to shift to

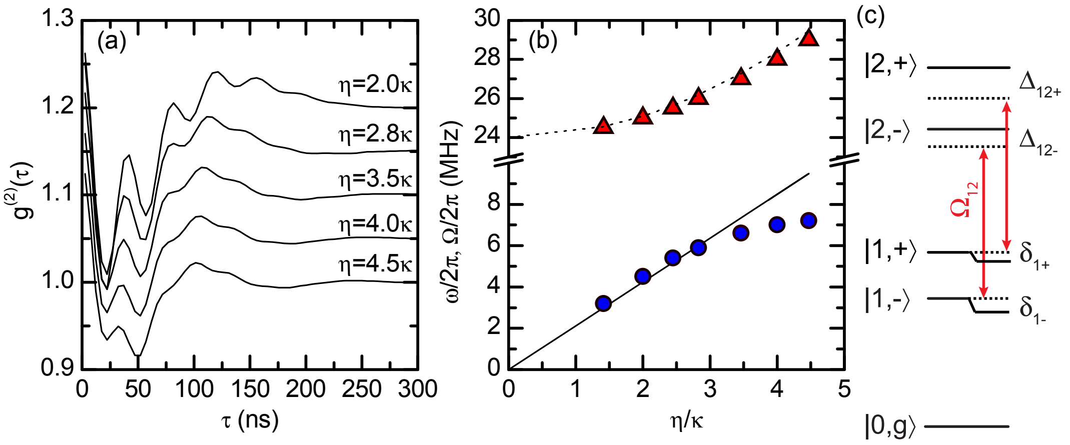

Figure 6.6: (a) Theoretical second-order correlation function for a fixed atom ($g/2\pi = 12$ MHz, $\Delta_c/2\pi = -12$ MHz) as a function of the driving strength. (b) The super Rabi oscillation frequency Ω (●) agrees nicely with the experimental results shown in Fig. 6.3 (b). The vacuum Rabi frequency (▲) experiences a quadratic shift well explained by standard perturbation theory (dashed line). It is not observed in the experiment because of the atomic motion. (c) The shift is caused by the off-resonant coupling of the normal modes to the higher-order dressed states induced by the probe laser.

higher frequencies with increasing driving strengths. This effect will be analyzed and discussed further in the next section.

6.2.5 Light Shift of the Normal Modes

For further analysis, we have calculated the second-order correlation functions for a fixed atom ($g/2\pi = 12$ MHz, $\Delta_{ac}/2\pi = 0$ MHz) driven on resonance with the normal modes ($\Delta_c/2\pi = -12$ MHz) for various driving strengths (cf. Fig. 6.6 (a)). We extract the two frequencies using the same fitting procedure as described in Section 6.2. The resulting frequencies, ω (▲) and Ω (●), are plotted in Fig. 6.6 (b). The power dependence of the super Rabi oscillation frequency matches nicely with the experimental results shown in Fig. 6.3 (b). However, in contrast to the results with position averaging, we clearly see that the fast oscillation frequency ω is not constant but increases with increasing driving strength.

This shift is caused by the off-resonant coupling between the normal modes and the higher-order dressed states induced by the probe light. As shown in Fig. 6.6 (c), the probe light, which is on resonance with $|1-\rangle$, also couples the states $|1-\rangle$ and $|2-\rangle$ with a Rabi frequency of $\Omega_{12} = (\sqrt{2}+1)\eta$ and a detuning of $\Delta_{12-} = (2-\sqrt{2})g$ (cf. Section 2.2.3). Calculating the resulting shift of the $|1-\rangle$ state using first-order perturbation theory yields a red shift of $\delta_{1-} = \frac{\Omega_{12}^2}{4\Delta_{12-}}$ in direct analogy to the AC-Stark shift of a two-level atom induced by an off-resonant laser [23]. The state $|1+\rangle$ is shifted in very much the same way due to the coupling between the $|1+\rangle$ and $|2+\rangle$ states with a Rabi frequency of $\Omega_{12} = (\sqrt{2}+1)\eta$ and a detuning of $\Delta_{12+} = \sqrt{2}g$. The coupling between the $|1+\rangle$ and the $|2-\rangle$ state ($\Omega'_{12} = (\sqrt{2}-1)\eta$) is much weaker and can be neglected (cf. also

Section 2.2.3). Since the probe laser is red detuned from the two respective transitions, both eigenstates, $|1-\rangle$ and $|1+\rangle$, are shifted towards lower frequencies. The effective shift of the frequency difference that appears in the correlation functions is then given by the difference of the individual shifts:

$$\delta_{1+} - \delta_{1-} = \frac{\Omega_{12}^2}{4}\left(\frac{1}{\Delta_{12+}} - \frac{1}{\Delta_{12-}}\right). \tag{6.3}$$

As one can see from Fig. 6.6 (b), this simple model (dashed black line) does indeed reproduce the frequency shift of the vacuum Rabi frequency observed in the theoretical correlation functions. When all the detunings are set to zero, an equivalent shift, called dynamical Stark effect, has been predicted from exact analytical calculations [24]. In the experiment, this effect is unfortunately counteracted by the averaging over different coupling strengths due to the atomic motion and could therefore not be observed conclusively.

6.3 Third-Order Correlation Function

The dynamics of the average photon number, $\langle a^\dagger a\rangle$, that we have considered so far is dominated by the coherent internal dynamics (vacuum Rabi oscillations) and driving (super Rabi oscillations) of the first-order dressed states only. The deviation from the two-level approximation of the super Rabi oscillation frequency and also the simple model that we have introduced to explain qualitatively the appearance of the vacuum Rabi oscillations require a non-negligible initial population of the second-order dressed states. However, their dynamics, in particular the quantum Rabi oscillation [12] at a frequency of $2\sqrt{2}g$, are not directly visible.

6.3.1 Dynamics of the Second-Order Dressed States

This motivates us to consider the dynamics of another observable, namely the probability for the detection of a photon pair, $\langle a^{\dagger 2}a^2\rangle$ (blue line in the quantum trajectory in Fig. 6.1 (a) and (b)). In contrast to the normal modes, the second-order dressed states emit photons in pairs [6]. Therefore, the probability to detect a photon pair is more sensitive to their occupation than the average photon number. This is supported by the corresponding quantum trajectory. The fast oscillations of $\langle a^{\dagger 2}a^2\rangle$, nicely visible in Fig. 6.1 (b), clearly deviate in frequency and visibility from the vacuum Rabi oscillations that appear for $\langle a^\dagger a\rangle$. In addition, the expectation value $\langle a^{\dagger 2}a^2\rangle$ also undergoes slow super Rabi oscillations at the same frequency as $\langle a^\dagger a\rangle$ but with a higher visibility.

To confirm this behavior experimentally, we evaluate the probability to detect a photon pair at a time τ before or after a single photon has been observed, corresponding to the third-order correlation function [25],

$$g^{(3)}(\tau,0) = \begin{cases} \langle a^\dagger a^\dagger(\tau)^2 a(\tau)^2 a\rangle / \langle a^\dagger a\rangle^3 & \tau>0 \\ \langle a^{\dagger 2} a^\dagger(-\tau) a(-\tau) a^2\rangle / \langle a^\dagger a\rangle^3 & \tau<0. \end{cases} \tag{6.4}$$

For $\tau > 0$, it measures the time dependence of $\langle a^{\dagger 2}a^2\rangle$ conditioned upon the detection of a single photon. For $\tau < 0$, it measures the time dependence of $\langle a^\dagger a\rangle$ conditioned upon the detection of a photon pair. A similar time dependence as for the second-order correlation function is expected in the latter case.

It is instructive to compare the correlation functions directly to a sample quantum trajectory as shown in Fig. 6.7 (a) where $\tau = 0$ is defined by the detection of a photon emitted from the cavity. Experimental and theoretical third-order correlation functions are plotted in Fig. 6.7 (b) ($\Delta_c/2\pi$ = −12 MHz, $\eta = 4.53\kappa$). Experiment and theory are in excellent agreement without any additional fit parameters (the integration volume and atom-cavity detuning are adjusted for the second-order correlation function and then kept constant). In analogy to the different time dependence of $\langle a^\dagger a\rangle$ and $\langle a^{\dagger 2}a^2\rangle$ in the quantum trajectory, the correlation function behaves differently for positive and negative times τ. On short timescales, a weak modulation at different frequencies is visible.

For $\tau < 0$, a local maximum at about 30 ns (red arrow) is observed. For a qualitative understanding, we introduce again a very simple model (cf. Fig. 6.7 (e)). On short timescales where the driving of the system can be neglected, the detection of three photons requires an initial population of the third-order dressed state $|3-\rangle$. The simultaneous detection of two photons at $\tau = 0$ (corresponding to two applications of the annihilation operator to the initial state $|3-\rangle$) causes a projection onto the non-stationary state $\frac{1}{2}(\sqrt{3}|1,g\rangle - |0,e\rangle)$. For $\tau < 0$, the third-order correlation function measures the successive vacuum Rabi oscillations of the average photon number $\langle a^\dagger a\rangle$ causing a local maximum after one oscillation period. Its position matches with the oscillation period of the average photon number in the quantum trajectory, which is also marked by a red arrow.

For $\tau > 0$, we find a *shoulder* at about 20 ns (blue arrow), which is in good agreement with the oscillation frequency of $\langle a^{\dagger 2}a^2\rangle$ in the quantum trajectory. In this case, a single photon is detected at $\tau = 0$ causing a projection onto the non-stationary state $\frac{1}{\sqrt{5}}(\sqrt{3}|2,g\rangle - \sqrt{2}|1,e\rangle)$. The subsequent measurement of the two-photon emission probability $\langle a^{\dagger 2}a^2\rangle$ then displays the quantum Rabi oscillations of the second-order dressed states with an expected period of about $2\pi/2\sqrt{2}g_0 = 22\,\text{ns}$ [12, 26]. Our simple model also explains the lower visibility of these quantum Rabi oscillations. It is a consequence of the fact that, after a single photon detection, the overlap of the projected state with the $|2-\rangle$ state is larger than the overlap between the $|1-\rangle$ state and the projected state after two photon detections.

As the mentioned *shoulder* is not very pronounced, we have plotted in Fig. 6.7 (c) and (d) the results of two other measurements ($\Delta_c/2\pi$ = −12 MHz, $\eta = 4.06\kappa$ and $\Delta_c/2\pi$ = −10 MHz, $\eta = 3.47\kappa$). They do not offer additional physical insights but demonstrate the reproducibility of this weak effect.

On longer timescales, the onset of super Rabi oscillations is also visible in $g^{(3)}(\tau, 0)$. While its frequency seems to be similar for positive and negative times, the amplitude is more pronounced in the first case. Both observations are in agreement with our previous statement, based on the sample quantum trajectory, that $\langle a^{\dagger 2}a^2\rangle$ and $\langle a^\dagger a\rangle$ oscillate slowly at a similar frequency but with different visibility.

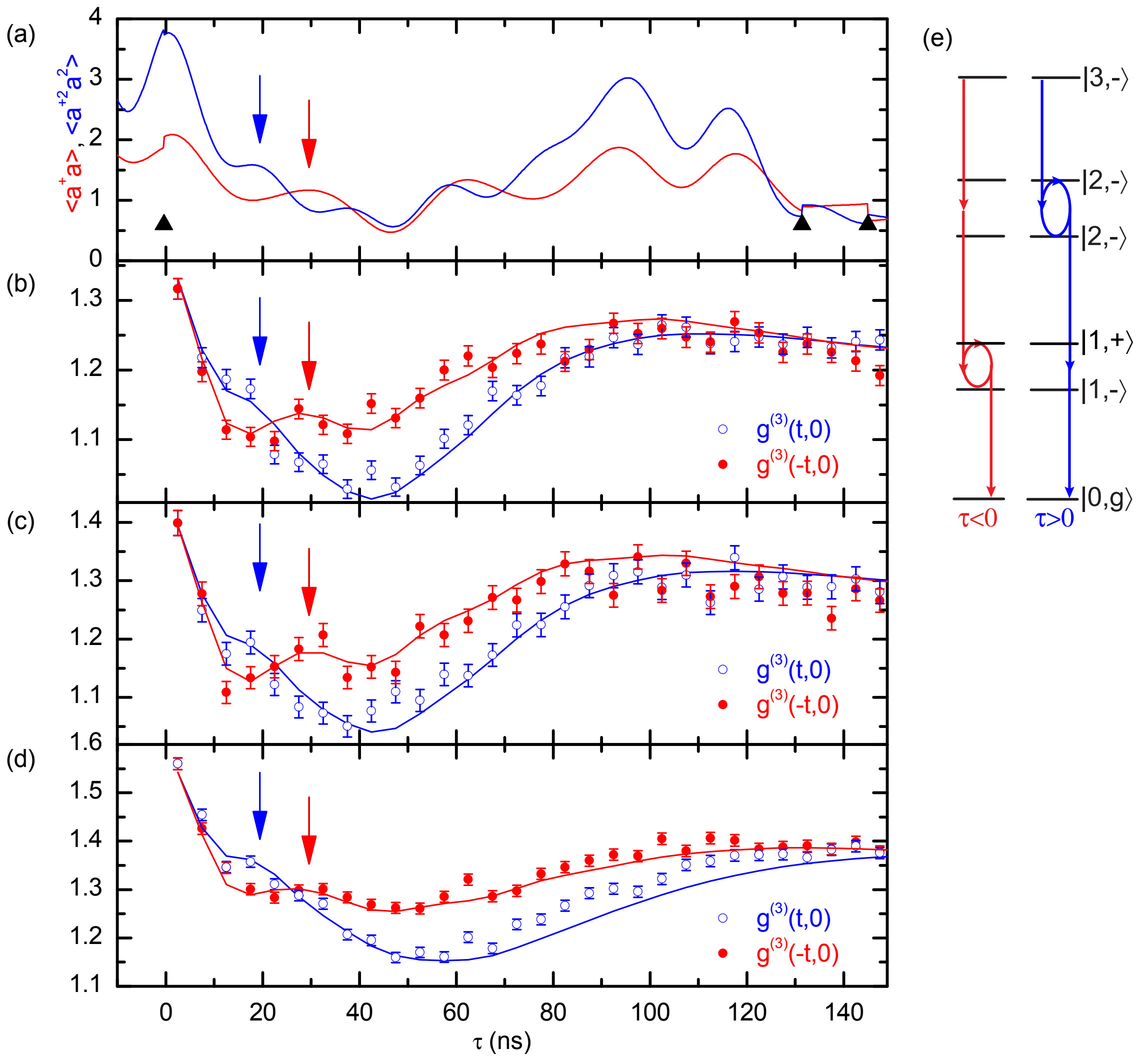

Figure 6.7: (a) A sample quantum trajectory ($g/2\pi$ = 14.5 MHz, $\Delta_a/2\pi = \Delta_c/2\pi$ = −12 MHz, η = 4.5κ) shows different oscillation frequencies for the observables $\langle a^\dagger a\rangle$ (red) and $\langle a^{\dagger 2}a^2\rangle$ (blue). (b) These frequencies are reproduced in the third-order intensity correlation function $g^{(3)}(\pm\tau, 0)$ ($\Delta_c/2\pi$ = −12 MHz, η=4.53 κ). The vacuum Rabi oscillations at a frequency of $2g_0$ are visible (red arrow) as a weak modulation for negative times (red, •), whereas the quantum Rabi oscillations at a frequency of $2\sqrt{2}g_0$ are visible (blue arrow) as a weak modulation for positive times (blue, ∘). (c-d) This weak modulation is also reproduced in measurements with different parameters ($\Delta_c/2\pi$ = −12 MHz, η = 4.06κ and $\Delta_c/2\pi$ = −10 MHz, η = 3.47κ). In general, they show the same characteristic features. The solid lines are theoretical calculations without any additional fit parameters. (d) A qualitative explanation is provided by a very simple model: Neglecting the driving, the detection of three photons requires an occupation of the third-order dressed state. For $\tau < 0$, a photon pair is emitted first. This projection onto a superposition of the normal modes gives rise to the vacuum Rabi oscillations causing a local maximum in the correlation function after one vacuum Rabi oscillation period. For $\tau > 0$, a single photon is detected first. The quantum Rabi oscillations of the second-order dressed states modulate the probability to detect a photon pair at a frequency of $2\sqrt{2}g_0$.

6.3.2 Three-Time Correlations

Next, we investigate how patterns of two successive photon detections determine the future trajectory of the system. As an example, consider the quantum trajectory shown in Fig. 6.1 (b), and here the two photons which are emitted at about 650 ns and 680 ns. How does the subsequent time evolution of the photon number depend on the separation between these two photon detections? To answer this question, we evaluate the general third-order correlation function,

$$g^{(3)}(\tau_1, \tau_2) = \frac{\langle a^\dagger a^\dagger(\tau_1) a^\dagger(\tau_1 + \tau_2) a(\tau_1 + \tau_2) a(\tau_1) a \rangle}{\langle a^\dagger a \rangle^3}. \tag{6.5}$$

It is proportional to the probability to detect three photons, with time separations τ_1 between first and second, and τ_2 between second and third photon. An example ($\Delta_c/2\pi = -12$ MHz, $\eta = 3.9\,\kappa$) is shown in Fig. 6.8 in the experiment (a) and theory (b). As before, no additional fit parameter is required to achieve good agreement between theory and experiment. The special case $g^{(3)}(\tau, 0)$ discussed previously can be found on the vertical (for $\tau{>}0$) and horizontal (for $\tau{<}0$) axis of this figure. Our question can now be answered by comparing different horizontal cuts through the figure. Each cut measures the time evolution of the average photon number after the detection of a photon pair separated by τ_1. We see immediately that there is a strong dependence on τ_1, that is on the previous measurement record, if this separation is shorter than the coherence time of the system.

The most interesting feature is the occurrence of a peak marked by two dashed lines at $\tau_1 \approx 2\pi/2g_0$ and $\tau_2 \approx 2\pi/2\Omega$, that is when the separation between the first two clicks is one period of a vacuum Rabi oscillation, whereas the separation between the second and the third click is half a period of the super Rabi oscillations. These timescales suggest that we observe an interplay between the vacuum Rabi oscillation and the super Rabi oscillation. We give an intuitive explanation in terms of the quantum measurement process: The detection of two photons separated by $\tau_1 \approx 2\pi/2g_0$ is a signature of the normal modes, which oscillate at this frequency. Between the two detection events, the state of the system therefore had a large contribution from the first-order dressed states. The detection of the second photon projects these states onto the ground state. Subsequently, the super Rabi oscillations cause a maximum of the excitation after half a super Rabi oscillation period (i.e., $\tau_2 \approx 2\pi/2\Omega$) leading to a high probability to detect a third photon after this time. The reverse process at $\tau_1 \approx 2\pi/2\Omega$ and $\tau_2 \approx 2\pi/2g_0$ is not particularly enhanced: the super Rabi frequency is not characteristic to any particular set of dressed states. Therefore, the detection of two photons separated by half a period of the super Rabi frequency does not change the subsequent time evolution much compared to the detection of just an individual photon. This explains the missing of a similar peak at $\tau_1 \approx 2\pi/2\Omega$ and $\tau_2 \approx 2\pi/2g_0$.

6.3.3 Intrinsic Third-Order Correlations

The third-order correlation function is proportional to the time evolution of the average photon number conditioned upon two previous detection events. We have argued

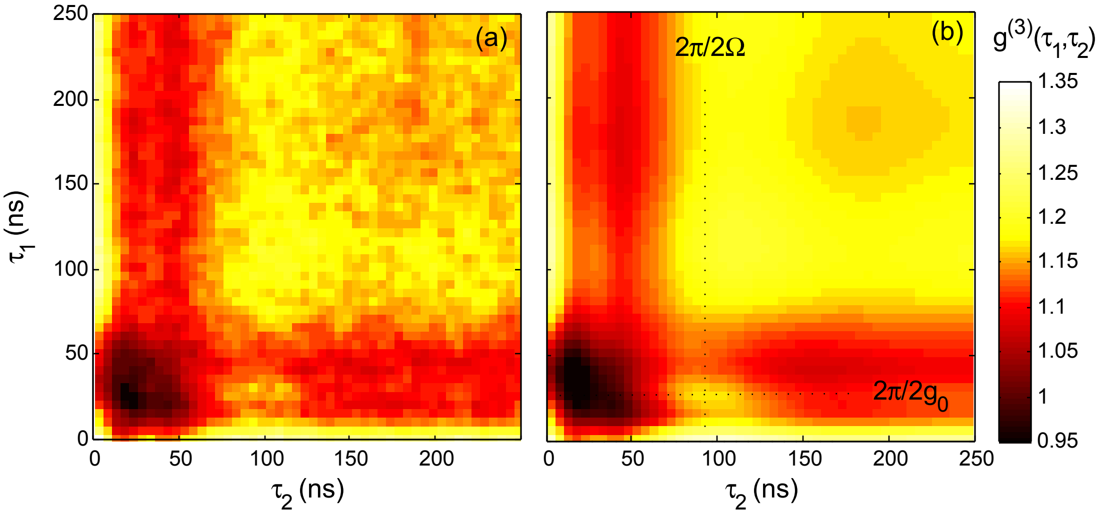

Figure 6.8: Third-order intensity correlation function $g^{(3)}(\tau_1, \tau_2)$ in the experiment (a) and theory (b) ($\eta = 4.06\,\kappa$). To reduce noise, it was convoluted with a two-dimensional Gaussian filter with a width (FWHM) of 7 ns. An explanation for the pronounced, time-asymmetric peak marked by the dashed lines is given in the text.

that the detection of two photons separated by some time τ_1 provides us with additional knowledge about the state of the system compared to just a single detection. Therefore, it alters the subsequent time evolution. However, the textbook example of a resonantly driven two-level atom in free space shows that this point requires further consideration. As this system can only scatter photons one-by-one the detection of a photon causes a projection onto the ground state of the atom and thus completely determines the state of the system. It is clear that, for this example, the detection of a photon pair does not convey additional information. Thus, we expect that the third-order correlation function is completely determined by the second-order correlation function. The intrinsic third-order correlations of a system are defined as the difference between the observed third-order correlations and the third-order correlations expected from lower-order correlations. Unfortunately, this definition is quite ambiguous since *what one expects from lower order correlations* can be (and has been) defined differently in literature, depending on whether one wants to make a comparison with a coherent [27] or a thermal [8] state. In the following, we will introduce yet another definition which we think is more suitable for our situation.

Intrinsic and Acquired Correlations

We define that a system does not possess intrinsic third-order correlations when the detection of a photon pair does not change our knowledge about the state of the system compared to just a single photon detection. Formally speaking, this is equivalent to assuming that the density matrix of the system after two detection events is equal to the density matrix after just a single photon detection, i.e.,

$$\begin{aligned}\overbrace{\frac{ae^{\mathcal{L}\tau}[a\rho_{\mathrm{s}}a^\dagger]a^\dagger}{\mathrm{tr}\,(ae^{\mathcal{L}\tau}[a\rho_{\mathrm{s}}a^\dagger]a^\dagger)}}^{\rho \text{ after the detection of a photon pair}} &= \overbrace{\frac{a\rho_{\mathrm{s}}a^\dagger}{\mathrm{tr}\,(a\rho_{\mathrm{s}}a^\dagger)}}^{\rho \text{ after the detection of a single photon}} \\ \Leftrightarrow ae^{\mathcal{L}\tau}[a\rho_{\mathrm{s}}a^\dagger]a^\dagger &= \frac{\langle a^\dagger a^\dagger(\tau)a(\tau)a\rangle}{\langle a^\dagger a\rangle}a\rho_{\mathrm{s}}a^\dagger = \frac{\gamma_2(\tau_1)}{\gamma_1}a\rho_{\mathrm{s}}a^\dagger.\end{aligned} \tag{6.6}$$

We have adopted the short-hand notation

$$\gamma_k(\tau_1 \ldots \tau_{\text{k-1}}) = \langle a^\dagger \ldots a^\dagger(\tau_1 + \ldots + \tau_{\text{k-1}})a(\tau_1 + \ldots + \tau_{\text{k-1}}) \ldots a\rangle \tag{6.7}$$

for the unnormalized correlation function. We now use Eq. 6.6 to rewrite the quantum regression theorem (cf. Section 2.3.3). The time-dependent third-order correlation function can be expressed in terms of the second-order correlation function only:

$$\begin{aligned}\gamma_3(\tau_1,\tau_2) &= \mathrm{tr}\{a^\dagger a e^{\mathcal{L}\tau_2}[ae^{\mathcal{L}\tau_1}\left[a\rho_{\mathrm{s}}a^\dagger\right]a^\dagger]\} \\ &= \frac{\gamma_2(\tau_1)}{\gamma_1}\mathrm{tr}\{a^\dagger a e^{\mathcal{L}\tau_2}[a\rho_{\mathrm{s}}a^\dagger]\} \\ &= \gamma_2(\tau_1)\gamma_2(\tau_2)/\gamma_1\end{aligned} \tag{6.8}$$

After proper normalization, we find $g^{(3)}(\tau_1,\tau_2) = g^{(2)}(\tau_1)g^{(2)}(\tau_2)$ for a system with no intrinsic third-order correlations. In the following, we will refer to this as the *acquired* third-order correlations as they are completely determined by lower-order correlations. The intrinsic third-order correlations, $k^{(3)}(\tau_1,\tau_2)$, of an arbitrary system are then defined as the difference between the total third-order correlations and the acquired third-order correlations:

$$k^{(3)}(\tau_1,\tau_2) := g^{(3)}(\tau_1,\tau_2) - g^{(2)}(\tau_1)g^{(2)}(\tau_2). \tag{6.9}$$

We would like to emphasize that, for a system without intrinsic third-order correlations, the third-order correlation function is alway symmetric in time. This is also true for the alternative definitions of the intrinsic correlations put forward in [8, 27]. The observation of a time asymmetry as discussed in the last sections is thus already a proof for the presence of intrinsic third-order correlations.

Intrinsic Correlations with Atomic Motion

In practice, the evaluation of the intrinsic correlation with position averaging is not as straightforward as Eq. 6.9 suggests. To understand this, we recall that the correlation function that we evaluate includes an averaging over different positions, i.e., coupling strengths and Stark shifts (cf. Appendix B for details). We write $\gamma_k(\tau_1 \ldots \tau_{\text{k-1}}, x)$ to denote the explicit dependence upon the position x. The position averaged expectations values are written as $\overline{\gamma_k(\tau_1 \ldots \tau_{\text{k-1}}, x)}_x$ where the position averaging comprises an

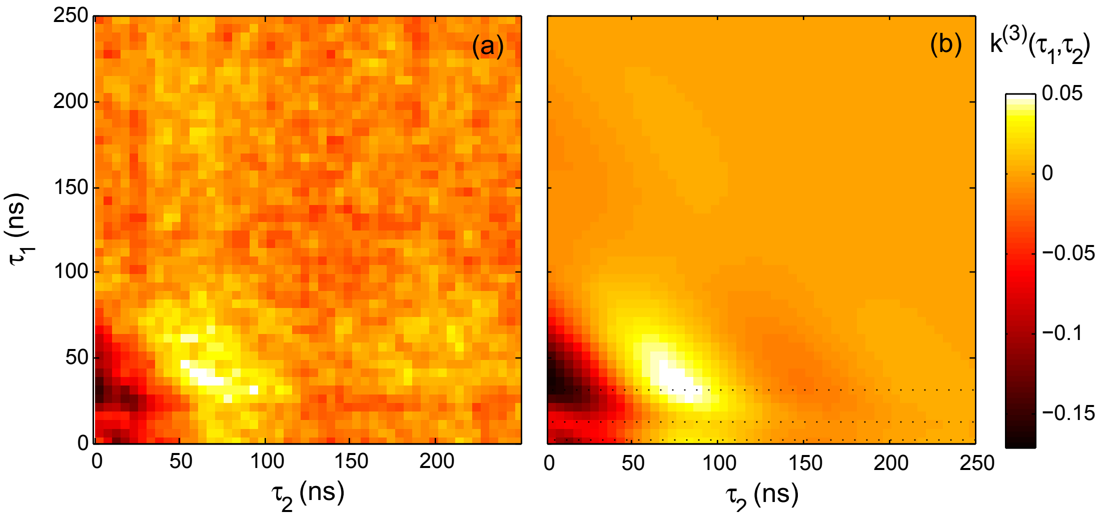

Figure 6.9: Intrinsic third-order correlations, $k^{(3)}(\tau_1,\tau_2)$, in the experiment (a) and theory (b) ($\Delta_c/2\pi$ =-12 MHz, η =4.06 κ). To reduce noise, it was convoluted with a two-dimensional Gaussian filter with a width (FWHM) of 7 ns. Three horizontal cuts marked by dashed lines are shown in Fig. 6.10 and discussed in the text.

integration over some atomic distribution function (cf. Appendix B). We would like to determine the position averaged intrinsic correlation function,

$$k^{(3)}(\tau_1,\tau_2) = \left(\overline{\gamma_3(\tau_1,\tau_2,x)}_x - \overline{\gamma_2(\tau_1,x)\gamma_2(\tau_2,x)/\gamma_1(x)}_x\right)/\overline{\gamma_1(x)}_x^3. \tag{6.10}$$

The difficulties arise from the fact that the position averaging does not factorize, that is the average over the acquired correlations (the second term on the right hand side) cannot be written as a product of lower order correlation functions, since

$$\overline{\gamma_2(\tau_1,x)\gamma_2(\tau_2,x)/\gamma_1(x)}_x \neq \overline{\gamma_2(\tau_1,x)}_x\overline{\gamma_2(\tau_2,x)}_x/\overline{\gamma_1(x)}_x. \tag{6.11}$$

Therefore, it is not possible to determine this term directly from a measurement. Instead, we have to rely on a theoretical calculation of the acquired correlation function with position averaging. In view of the good agreement that we have found between theoretical and experimental correlation functions, we can expect that our theoretical calculations yield reliable results for the acquired correlations as well. We then determine the intrinsic correlations by taking the difference between the measured third-order correlations and the (calculated) acquired correlations.

Results

Experimental and theoretical results of intrinsic third-order correlation function for the parameters discussed in Section 6.3.2 are shown in Fig. 6.9. In general, the intrinsic correlation function looks quite differently from the raw third-order correlation function. In particular, the time asymmetry is much more pronounced. The interplay between vacuum Rabi oscillations and super Rabi oscillations discussed before is reflected by the

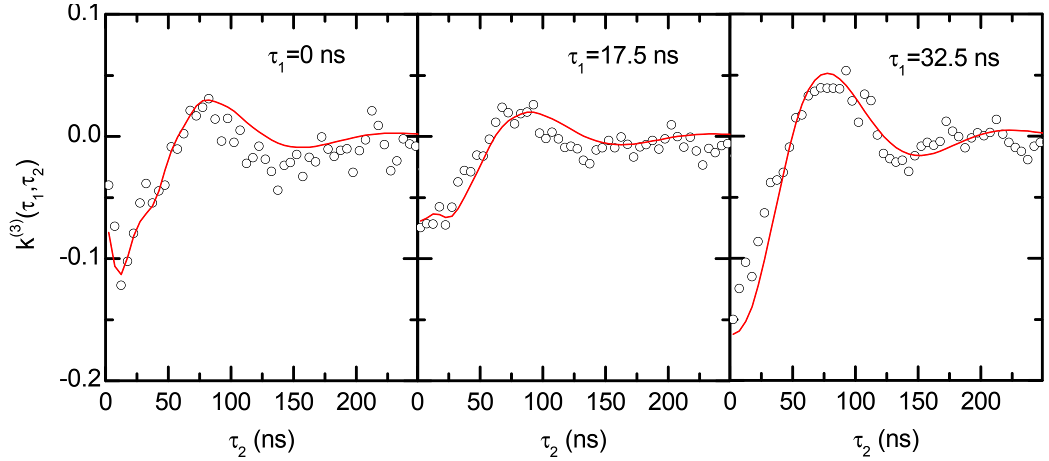

Figure 6.10: Intrinsic third-order correlations $k^{(3)}(\tau_1, \tau_2)$ for three fixed values of τ_1 in the experiment (∘) and theory (red line). A detailed discussion can be found in the text.

bright peak at $\tau_1 \approx 2\pi/2g_0$ and $\tau_2 \approx 2\pi/2\Omega$. For a better understanding, we fix the time separation between the first two photons τ_1 to zero, half a period of the vacuum Rabi oscillations and a full period of the vacuum Rabi oscillations. This corresponds to a discussion of the horizontal cuts in Fig. 6.9 (b) marked by dashed lines. The respective intrinsic correlations are plotted in Fig. 6.10 as a function of τ_2. In all three situations, the intrinsic correlations at $\tau_2 = 0$ are negative implying a reduced probability to detect a third photon directly after the detection of a photon pair. The time dependence of the intrinsic correlation is dominated by the super Rabi oscillations. We clearly see that the amplitude of these oscillations varies with the separation, τ_1, between the first two photon clicks.

The case $\tau_1 = 0$ serves as a reference. In contrast to just a single photon detection, the simultaneous detection of two photons projects also the steady-state population of the second-order dressed states onto the ground state, which, subsequently, undergoes super Rabi oscillations visible in the intrinsic correlation function.

The amplitude of the super Rabi oscillations decreases when the time separation between the first two-photons is half a period of the vacuum Rabi oscillations ($\tau_1 \approx$ 17.5 ns). For an intuitive explanation, we recall that, if the system is initially prepared in the second-dressed state $|2-\rangle$, the detection of a first photon projects it onto a superposition of the normal modes. Subsequently, the system undergoes vacuum Rabi oscillations and the probability for the emission a second photon is suppressed after half a period of the vacuum Rabi oscillations. The detection of two photons separated by this time thus indicates an initial population of the third- or even higher-order dressed states. After the arrival of the photon pair, the system is not well prepared in the ground state. The visibility of the super Rabi oscillations is reduced.

The opposite is true when the first two photons are separated by a full period of the vacuum Rabi oscillations. Such a photon pattern is most likely to occur from an initial population of the second-order dressed states. The detection projects it onto the ground state and the subsequent super Rabi oscillations are nicely visible.

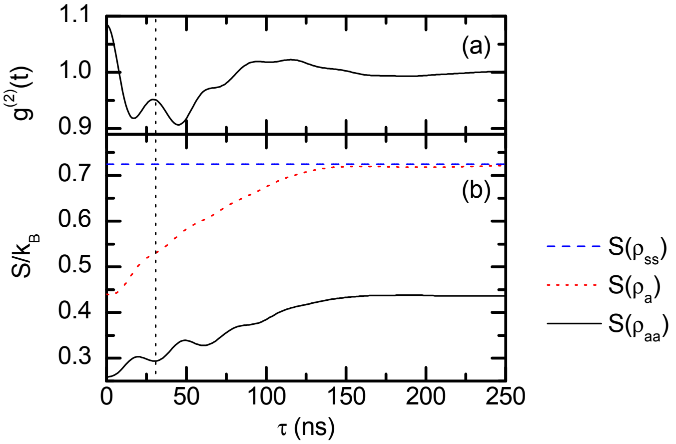

Figure 6.11: (a) Theoretical second-order correlation function for a fixed atom ($g/2\pi$ = 12 MHz, $\Delta_\mathrm{c}/2\pi = -12$ MHz, $\eta = 3.5\kappa$). (b) Entropy of the steady-state density matrix ($S(\rho_\mathrm{s})$, dashed blue line), time dependence of the entropy after the detection of a photon ($S(\rho_\mathrm{a}(\tau))$, dotted red line) and entropy after two photon detections separated by the time τ ($S(\rho_\mathrm{aa}(\tau))$, solid black line). The smaller the entropy, the larger our knowledge about the state of the system. The detection of two photons separated by one period of the vacuum Rabi oscillations (vertical dotted line) provides us with additional knowledge about the state of the system causing a local minimum of $S(\rho_\mathrm{aa}(\tau))$ at this time. This explains the interplay of vacuum Rabi oscillations and super Rabi oscillations discussed in the last section.

6.4 Correlation Functions and Entropy

In our previous discussion, we have argued that the detection of two photons with a certain time separation provides us with additional knowledge about the state of the system leading to a characteristic time evolution in the future. Before concluding this chapter, we would like to revisit this point from a slightly different perspective, namely in terms of the entropy of the system. It can be considered as a measure for how well the state of the system is known. We recall that the van Neumann entropy of a density matrix ρ is defined as [28]:

$$S(\rho) = -k_B\langle\log\rho\rangle = -k_B\mathrm{tr}(\rho\log\rho) \tag{6.12}$$

with the Boltzmann constant k_B. Perfect knowledge about the state of the system corresponds to a pure-state density matrix with an entropy of zero. For mixed states, the entropy takes positive values with a maximum value of $k_B\log N$ when the system is equally distributed among all N accessible states. We are interested in the entropy under three different conditions: First, the entropy of the steady-state density matrix $S(\rho_\mathrm{s})$, which serves as a reference. Second, the time evolution of the entropy after a photon has been detected $S(\rho_\mathrm{a}(\tau))$, with the collapsed density matrix $\rho_\mathrm{a} = a\rho_\mathrm{s}a^\dagger/\mathrm{tr}(a\rho_\mathrm{s}a^\dagger)$. Third, the entropy of the system after two photons separated by the time τ have been detected, $S(\rho_\mathrm{aa}(\tau))$ - an event which is described by the density matrix $\rho_\mathrm{aa}(\tau) = a\rho_\mathrm{a}(\tau)a^\dagger/\mathrm{tr}(a\rho_\mathrm{a}(\tau)a^\dagger)$.

Theoretical results for a fixed atom ($g/2\pi = 12$ MHz, $\Delta_c/2\pi = -12$ MHz, $\eta = 3.5\kappa$) are plotted in Fig. 6.11. For comparison, we have also plotted the second-order correlation function (Fig. 6.11 (a)) showing the timescales of the characteristic vacuum Rabi and super Rabi oscillations. The entropy of the steady state, $S(\rho_s)$, is plotted as a blue dashed line. As expected, the detection of a photon provides information about the state of the system causing a reduction of the entropy, $S(\rho_a(\tau))$ (dotted red line). Due to the presence of dissipation and driving the entropy then increases almost monotonously back to its steady state. Next, we consider the entropy when a second photon is detected at time τ after the first photon detection, $S(\rho_{aa}(\tau))$ (solid black line). It is clearly modulated at the vacuum Rabi frequency with local minima at multiples of the vacuum Rabi oscillation period and local maxima in-between. This underlines the validity of arguments given in the last sections to explain the time dependence of the intrinsic third-order correlations: The detection of a photon pair separated by one period of the vacuum Rabi oscillations yields more information about the state of the system than a photon pair that is separated by half a period. For larger separations between the two photon detections, the entropy increases to an asymptotic value, which is equal to the entropy after just a single detection event, $S(\rho_a(0))$. This simply reflects the fact that when the time separation between the first and second photon detection exceeds the coherence time of the system, the intrinsic correlations vanish, that is the detection of the photon pair projects the state of the system onto the same density matrix as just a single photon detection.

6.5 Time Asymmetry

Both discussed effects, the different dynamics of the first- and second-order dressed states as well as the interplay between vacuum and super Rabi oscillations, give rise to pronounced time-asymmetries of the third-order correlation function, i.e., $g^{(3)}(\tau_1, \tau_2) \neq g^{(3)}(\tau_2, \tau_1)$ demonstrating that the transmitted photon stream is asymmetric in time.

Our explanation for the asymmetry was based on the fact that the quantum jumps of the system on the Jaynes-Cummings ladder are accompanied by photon cascades with a specific directionality in time. For example, by comparing the time evolution of $g^{(3)}(\tau, 0)$ for positive and negative times, we have studied the time evolution of different observable, namely $\langle a^\dagger a \rangle$ and $\langle a^\dagger a^\dagger a a \rangle$, which differ due to the different dynamics of the first- and second-order dressed states.

In a way, this effect is directly related to the time asymmetries that have been observed in different physical systems as a consequence of the cascaded emission of photons at different colors. Two nice examples are the consecutive emission of two photons in the spectral sidebands of a strongly driven two-level system in free space [29] or the cascaded biexciton-exciton emission from a quantum dot [30]. Time asymmetries due to the consecutive emission of single photons and photon pairs, as we observe it, have, to our knowledge, not been investigated before.

In cavity QED, evidence for a time asymmetry has also been found in previous studies of intensity-field correlation functions [31]. However, the effect was hardly above the noise level and no quantitative comparison with theory could be made.

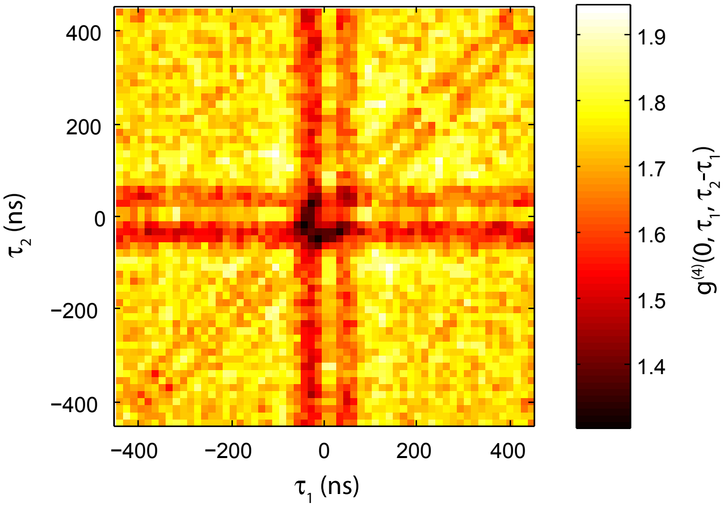

Figure 6.12: Experimental fourth-order intensity correlation function $g^{(4)}(0, \tau_1, \tau_2 - \tau_1)$. A discussion of the rich temporal structure will be the subject of future investigations.

In a more general context, it has been proposed that the occurrence of such time-asymmetric fluctuations in the output fields is a consequence of the breakdown of detailed balance in a driven system far away from thermal equilibrium [32]. We will review these arguments and point out some subtleties not discussed in [32] in Appendix D.

6.6 Conclusion and Outlook

In conclusion, using second- and third-order intensity correlations, we are able to probe the dynamics of the normal modes and the second rung of dressed states. All relevant dynamical processes - dissipation, driving and internal dynamics - have been observed. We have found good agreement with a theoretical model and could also provide intuitive explanations of the observed effects. Moreover, we introduced a new definition of the intrinsic third-order correlations that highlights how the detection of photon pairs influences the knowledge about the state of the system.

An appealing perspective is to use the information gained by the detection events to control the system by means of feedback. For example, an experiment by the Orozco group [33] has demonstrated that the fluctuations of the output field can be reduced by applying feedback conditioned upon single detection events. As we have seen multiple detection events can provide additional knowledge and thus might enable more sophisticated feedback schemes.

The strong-driving regime of cavity QED that we have just started to investigate here has so far attracted little experimental and theoretical attention. This is surprising in face of the fact that it offers very interesting perspectives such as single atom bistability due to the dynamical polarization of the dressed states [34, 35] or multi-photon blockade effects [36]. Moreover, we expect that these investigations will shed new light on the connection between quantum and semi-classical descriptions of the atom-cavity system. For example, there exists a close analogy between the super Rabi oscillations that we observe and the Rabi-like oscillations occurring in a driven anharmonic oscillator [18]. At high driving strenghts, the latter can be explained by a classical model. This raises the interesting question whether semi-classical non-linear oscillator models, like the ones put forward in [37, 38] in a quite different context of cavity QED, might also be applicable to our measurements at strong driving strengths.

Another obvious perspective is of course to investigate even higher-order correlation functions. The four detectors that we have available allow us to evaluate the fourth-order intensity correlation function. An example is shown in Fig. 6.12 showing $g^{(4)}(0, \tau_1, \tau_2 - \tau_1)$ ($\Delta_c/2\pi = -12$ MHz, $\eta = 3.9\kappa$), which is proportional to the probability to detect a photon pair followed or precedented by two other photons at times τ_1 and τ_2. To achieve a sufficient signal to noise ratio, the binning time was increased to 15 ns compared to our previous results. The most interesting part is the central region when all four photons arrive within the coherence time of the system. A detailed discussion of the temporal structure and measurements achieving a better temporal resolution will be an interesting subject for future investigations.

Our analysis of correlation functions has revealed patterns in a seemingly randomly fluctuating stream of photons. Correlation functions are also commonly used to study fluctuations of other observables in a variety of physical systems. While most experiments focus on second-order correlation functions, there are several examples where additional insight has been gained by investigating higher-order correlations. Some examples are lasers near threshold [7, 8], non-Gaussian scattering processes [9], ultra-cold atoms [39, 40] or the charge transfer through nano-electronic devices, such as quantum dots [41] or point contacts [42]. Our results, for example our new definition of the intrinsic correlation function, might also find applications for the study of these systems.

Bibliography

[1] L. Tian and H. Carmichael, *Phys. Rev. A* **46**, R6801 (1992).

[2] G. Rempe, R. J. Thompson, R. J. Brecha, W. D. Lee, and H. J. Kimble, *Phys. Rev. Lett.* **67**, 1727 (1991).

[3] K. M. Birnbaum, A. Boca, R. Miller, A. D. Boozer, T. E. Northup, and H. J. Kimble, *Nature* **436**, 87 (2005).

[4] B. Dayan, A. S. Parkins, T. Aoki, E. P. Ostby, K. J. Vahala, and H. J. Kimble, *Science* **319**, 1062 (2008).

[5] D. J. Alton, N. P. Stern, Takao, H. Lee, E. Ostby, K. J. Vahala, and H. J. Kimble, *Nature Phys.* **7**, 159 (2011).

[6] A. Kubanek, A. Ourjoumtsev, I. Schuster, M. Koch, P. W. H. Pinkse, K. Murr, and G. Rempe, *Phys. Rev. Lett.* **101**, 203602 (2008).

[7] S. Chopra and L. Mandel, *Phys. Rev. Lett.* **30**, 60 (1973).

[8] M. Corti and V. Degiorgio, *Phys. Rev. A* **14**, 1475 (1976).

[9] P.-A. Lemieux and D. J. Durian, *J. Opt. Soc. Am. A* **16**, 1651 (1999).

[10] P. Münstermann, T. Fischer, P. W. H. Pinkse, and G. Rempe, *Opt. Comm.* **159**, 63 (1999).

[11] M. Koch, C. Sames, M. Balbach, H. Chibani, A. Kubanek, K. Murr, T. Wilk, and G. Rempe, *Phys. Rev. Lett.* **107**, 023601 (2011).

[12] M. Brune, F. Schmidt-Kaler, A. Maali, J. Dreyer, E. Hagley, J.-M. Raimond, and S. Haroche, *Phys. Rev. Lett.* **76**, 1800 (1996).

[13] I. Chiorescu, P. Bertet, K. Semba, Y. Nakamura, C. J. P. M. Harmans, and J. E. Mooij, *Nature* **431**, 159 (2004).

[14] K. B. Cooper, M. Steffen, R. McDermott, R. W. Simmonds, S. Oh, D. A. Hite, D. P. Pappas, and J. M. Martinis, *Phys. Rev. Lett.* **93**, 180401 (2004).

[15] J. Johansson, S. Saito, T. Meno, H. Nakano, M. Ueda, K. Semba, and H. Takayanagi, *Phys. Rev. Lett.* **96**, 127006 (2006).

[16] J. Bochmann, M. Mücke, G. Langfahl-Klabes, C. Erbel, B. Weber, H. P. Specht, D. L. Moehring, and G. Rempe, *Phys. Rev. Lett.* **101**, 223601 (2008).

[17] A. Kubanek, *Two-photon gateway and feedback control of a single atom in a cavity*, PhD thesis, Technische Universität München (2010).

[18] J. Claudon, A. Zazunov, F. W. J. Hekking, and O. Buisson, *Phys. Rev. B* **78**, 184503 (2008).

[19] A. Faraon, I. Fushman, D. Englund, N. Stoltz, P. Petroff, J. Vuckovic, A. Faraon, I. Fushman, D. Englund, N. Stoltz, P. Petroff, and J. Vučković, *Nature Physics* **4**, 859 (2008).

[20] L. S. Bishop, J. M. Chow, J. Koch, A. A. Houck, M. H. Devoret, E. Thuneberg, S. M. Girvin, and R. J. Schoelkopf, *Nature Phys.* **5**, 105 (2009).

[21] C. Lang, D. Bozyigit, C. Eichler, L. Steffen, J. M. Fink, A. A. Abdumalikov, M. Baur, S. Filipp, M. P. da Silva, A. Blais, and A. Wallraff, *Phys. Rev. Lett.* **106**, 243601 (2011).

[22] D. F. Walls and G. J. Milburn, *Quantum Optics*, Springer, Berlin (1994).

[23] H. J. Metcalf and P. van der Straten, *Laser Cooling and Trapping*, Springer, Berlin (1999).

[24] P. Alsing, D.-S. Guo, and H. J. Carmichael, *Phys. Rev. A* **45**, 5135 (1992).

[25] R. J. Glauber, *Phys. Rev. Lett.* **10**, 84 (1963).

[26] M. Hofheinz, E. M. Weig, M. Ansmann, R. C. Bialczak, E. Lucero, M. Neeley, A. D. O'Connell, H. Wang, J. M. Martinis, and A. N. Cleland, *Nature* **454**, 310 (2008).

[27] C. D. Cantrell, M. Lax, and W. A. Smith, *Phys. Rev. A* **7**, 175 (1973).

[28] J. von Neumann, *Mathematische Grundlagen der Quantenmechanik*, Springer-Verlag Berlin (1932).

[29] A. Aspect, G. Roger, S. Reynaud, J. Dalibard, and C. Cohen-Tannoudji, *Phys. Rev. Lett.* **45**, 617 (1980).

[30] E. Moreau, I. Robert, L. Manin, V. Thierry-Mieg, J. M. Gérard, and I. Abram, *Phys. Rev. Lett.* **87**, 183601 (2001).

[31] G. T. Foster, L. A. Orozco, H. M. Castro-Beltran, and H. J.

Carmichael, *Phys. Rev. Lett.* **85**, 3149 (2000).
[32] A. Denisov, H. M. Castro-Beltran, and H. J. Carmichael, *Phys. Rev. Lett.* **88**, 243601 (2002).
[33] W. P. Smith, J. E. Reiner, L. A. Orozco, S. Kuhr, and H. M. Wiseman, *Phys. Rev. Lett.* **89**, 133601 (2002).
[34] P. Alsing and H. J. Carmichael, *Quantum Opt.* **3**, 13 (1991).
[35] M. A. Armen, A. E. Miller, and H. Mabuchi, *Phys. Rev. Lett.* **103**, 173601 (2009).
[36] S. Shamailov, A. Parkins, M. Collett, and H. Carmichael, *Optics Communications* **283**, 766 (2010).
[37] Y. T. Chough and H. J. Carmichael, *Phys. Rev. A* **54**, 1709 (1996).
[38] V. Peano and M. Thorwart, *Europhys. Lett.* **89**, 17008 (2010).
[39] S. S. Hodgman, R. G. Dall, A. G. Manning, K. G. H. Baldwin, and A. G. Truscott, *Science* **331**, 1046 (2011).
[40] V. Guarrera, P. Wuertz, A. Ewerbeck, A. Vogler, G. Barontini, and H. Ott, *Phys. Rev. Lett.* **16**, 160403 (2011).
[41] S. Gustavsson, R. Leturcq, B. Simoviccaron, R. Schleser, T. Ihn, P. Studerus, K. Ensslin, D. C. Driscoll, and A. C. Gossard, *Phys. Rev. Lett.* **96**, 076605 (2006).
[42] G. Gershon, Y. Bomze, E. V. Sukhorukov, and M. Reznikov, *Phys. Rev. Lett.* **101**, 016803 (2008).

Chapter 7

Correlation Functions and Photon Statistics

Contents

We have introduced measurements of time-dependent correlation functions to study the quantum dynamics of the atom-cavity system. It is well known that the second-order correlation function $g^{(2)}(0)$ carries information about the variance, i.e., the width of the photon-number distribution [1]. In this chapter, we show that measurements of the third-order correlation function $g^{(3)}(0,0)$ provide additional information about the photons statistics. This enables us to reconstruct the photon-number distribution of the driven atom-cavity system.

Our interest in the photon-number distribution is particularly motivated by the fact that cavity QED has proven to be a powerful tool to generate light states with unusual, i.e., non-Poissonian and non-Gaussian photon statistics. For example, Fock states [2, 3], superposition of Fock states [4] and Schrödinger cat states [5] have been generated in microwave cavity quantum electrodynamics. In the optical domain, very efficient single-photon sources based on single atoms in cavities have been demonstrated [6, 7, 8]. While in these examples the generated states were all but stationary, even the steady state of the continuously driven atom-cavity system shows unusual photon-number distributions. This is a consequence of the anharmonicity of the Jaynes-Cummings ladder that allows to drive selectively certain dressed states via multi-photon transitions [9]. On the one hand, on resonance with the normal modes, a photon blockade [10, 11] has been inferred from the observation of anti-bunching in the second-order correlation function. Resonant excitation of the second dressed states, on the other hand, leads to an enhanced emission of photon pairs as it was concluded from the observation of bunching

[12, 13]. This effect has been called a two-photon gateway. Both effects have been characterized exclusively by measurements of the second-order correlation function. A full reconstruction of the photon-number distribution has not been attempted.

Different techniques to measure photon-number distributions have been used in the past, such as photon-number resolving detectors [14], optical homodyne tomography [15] or techniques based on time multiplexing of light pulses [16, 17]. The reconstruction based on correlation functions that we employ here has the advantage that it uses standard, commercially available single-photon detectors and that it is not only applicable to pulses but also to steady-state photon-number distributions. It is closely related to a much more general theoretical proposal for quantum state reconstruction based on photon chopping and coincidence counting [18].

After introducing the principle of our reconstruction algorithm and characterizing its accuracy, we will reconstruct the photon-number distribution for the two scenarios discussed before, the photon blockade and the two-photon gateway, which is strictly speaking a multi-photon gateway in our case. Even though the blockade and gateway effects that we observe are rather weak, these results serve as a proof of principle experiment, highlighting the versatility of measurements of the third- and higher-order intensity correlation functions.

7.1 Reconstruction Algorithm

To understand how correlation functions can be used to reconstruct the photon-number distribution $p(n)$ inside the cavity, we note that the unnormalized k-th order intensity correlation function, $\gamma_k = \langle a^{\dagger k} a^k \rangle$, can be expressed in terms of the photon-number distribution as:

$$\gamma_k = \langle \hat{n}(\hat{n}-1)...(\hat{n}-k+1) \rangle = \sum_{n=k+1}^{\infty} p(n) \frac{n!}{(n-k)!} \tag{7.1}$$

A measurement of correlation functions up to the third-order accompanied by the normalization of the probability distribution ($\sum p(n) = 1$) provides us thus with four linear equations for an infinity of unknowns $p(n)$. It seems reasonable to neglect the occupation of the Fock states much higher than the average photon number. As we will see later on, setting the occupation above the four-photon Fock state equal to zero ($p(n \geq 5) = 0$) yields good results for our experimental parameters. However, for $n = 4$, this approximation is not valid.

A better approximation can be made by noting that the fourth-order correlation function can be rewritten as [19]

$$\gamma_4 = \langle : \Delta\hat{n}^4 : \rangle + 4\gamma_3\gamma_1 - 6\gamma_2\gamma_1^2 + 3\gamma_1^4 \tag{7.2}$$

with the fluctuation operator $\Delta\hat{n} = \hat{n} - \langle\hat{n}\rangle$. We emphasize that the term on the right hand side is a sum of two terms: the fourth-order cumulant $\langle : \Delta\hat{n}^4 : \rangle$ and a term that depends only on lower order correlations. Similar expressions can be found for arbitrary k-th order correlation functions. This has motivated the original definition of the intrinsic correlations [20] as the first term in Eq. 7.2. Note that this definition is different from the one we have introduced in Chapter 6. To estimate the fourth-order correlation function from lower order correlations, we neglect this term, making the approximation $\gamma_4 \approx 4\gamma_3\gamma_1 - 6\gamma_2\gamma_1^2 + 3\gamma_1^4$. Further justification for this approximation will be given in the next section. We obtain for the probability distribution of up to four photons:

$$\begin{aligned} p(0) &= \frac{1}{24}(24 - 24\gamma_1 + 12\gamma_2 - 4\gamma_3 + \gamma_4) \\ p(1) &= \frac{1}{6}(6\gamma_1 - 6\gamma_2 + 3\gamma_3 - \gamma_4) \\ p(2) &= \frac{1}{4}(2\gamma_2 - 2\gamma_3 + \gamma_4) \\ p(3) &= \frac{1}{6}(\gamma_3 - \gamma_4) \\ p(4) &= \frac{1}{24}(\gamma_4) \\ \gamma_4 &= 4\gamma_3\gamma_1 - 6\gamma_2\gamma_1^2 + 3\gamma_1^4 \end{aligned} \tag{7.3}$$

7.2 Experimental Procedure and Data Analysis

We use the same experimental procedure described in the last chapter to measure the first-, second- and third-order correlation function of the light that is transmitted through the cavity when individual atoms pass through the cavity mode. An example ($\Delta_c/2\pi = -16$ MHz, $\eta = 3.91\kappa$) is shown in Fig. 7.1.

The theoretical curves were obtained using the theoretical model used before (cf. Appendix B for details). We also calculate the theoretical photon-number distribution from the steady-state solution of the master equation using:

$$p_{\text{theo}}(n) = \int \langle n|\rho_{\text{s}}(x)|n\rangle P(x)dx \tag{7.4}$$

where $\rho_{\text{s}}(x)$ is the steady-state density matrix at the position x and $P(x)$ is the atomic distribution discussed in Appendix B.

To apply the reconstruction algorithm described in the previous section, we need to determine the unnormalized correlation functions γ_k. For this purpose, we first determine the average photon number $\gamma_1 = \langle a^\dagger a\rangle$ from the average photon flux behind the cavity. This enables us to calculate the unnormalized higher-order correlations via $\gamma_k = g^{(k)}(0)\langle a^\dagger a\rangle^k$. Finally, we can use Eq. 7.3 to reconstruct the photon-number distribution. To determine error bars, an uncertainty of the detection efficiency on the order of 5 % is taken into account.

To verify if the reconstruction algorithm does indeed yield reliable results, we compare the theoretical photon-number distribution with the distribution that we obtain by applying the reconstruction algorithm to the theoretical correlation functions. The results for the previous example (cf. Fig. 7.1) are plotted in Fig. 7.2. Figure (a) shows the theoretical (p_{theo}, black) as well as three different reconstructed photon-number distributions. First, we only take into account the second-order correlation function and truncate the distribution after the two-photon Fock state (p_2, gray). Second, we

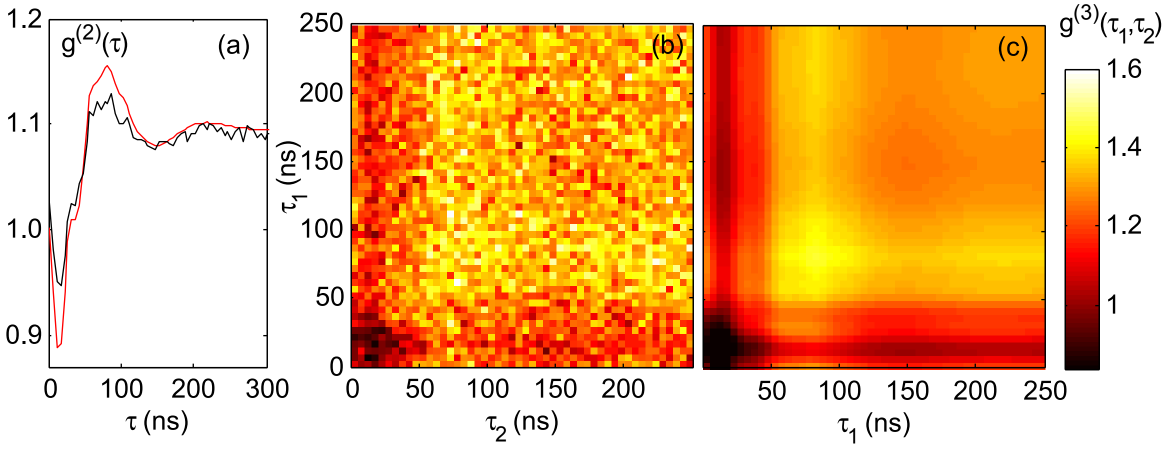

Figure 7.1: (a) Experimental and theoretical second-order correlation function, $g^{(2)}(\tau)$, at a detuning of $\Delta_c = -16$ MHz on resonance with the normal modes ($\eta = 3.91\kappa$). Third-order correlation function, $g^{(3)}(\tau_1, \tau_2)$, in the experiment (b) and theory (c). The photon-number distribution, $p(n)$, can be reconstructed by evaluating the correlation functions $g^{(2)}(0)$ and $g^{(3)}(0,0)$. Using the asymptotic values of the correlation functions, we can also determine the photon-number distribution of a coherent state with equivalent intensity modulation $p_{\mathrm{coh}}(n)$, which serves as a reference.

also take into account the third-order correlation function, but we assume $p(n \geq 4) = 0$ (p_3, blue). Last, we apply the full reconstruction algorithm described in the last section (p_4, red). The deviation of the reconstructed from the theoretical distribution (Fig. 7.2 (b)) clearly shows how the quality of the reconstruction improves for the three algorithms. A similar behavior was also observed for measurements with different parameters discussed below.

The photon number distribution alone is not very instructive, since it depends strongly on the average photon number, which obviously varies with the detuning of the probe light. In other words, even for an empty cavity, we would expect a trivial change of the photon-number distribution when the probe frequency is varied. Instead, we compare the reconstructed distribution with some reference distribution with the same average photon number. The most obvious choice for this reference distribution is of course the Poisson distribution of a coherent field with the same average photon number. However, we know that the motion of the atom causes a variation of the average photon number leading to a broadening of the photon-number distribution. Since we are not interested in the variation of the photon-number distribution due to the atomic motion but in its variation due to the anharmonic spectrum of the coupled atom-cavity system, the reference distribution that we need to determine is an average over different coherent states whose average photon numbers are varied in the same way as the atomic motion varies the average photon number in the experiment. In the following, we will refer to this distribution as $p_{\mathrm{coh}}(n)$. In theory, we can determine it by using the same position averaging as it is used for the calculation of the correlation function. For each position in the cavity, we calculate the average photon number

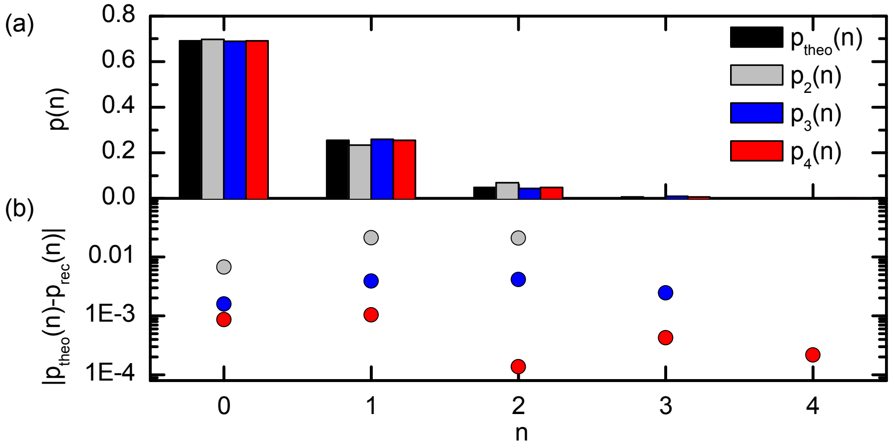

Figure 7.2: (a) Photon-number distribution with position averaging ($p_{\text{theo}}(n)$) and reconstructed distribution for different reconstruction algorithms using correlations up to second-order ($p_2(n)$), third-order ($p_3(n)$) and fourth-order ($p_4(n)$), cf. text for details). (b) The decrease of the deviation of the reconstructed distributions from the theoretical distribution shows that the accuracy of the reconstruction algorithm increases when higher-order correlations are taken into account.

and the corresponding Poisson distribution. Then we average the distribution over the different positions using the weighting function described in Appendix B.

To determine $p_{\text{coh}}(n)$ from the experimental results requires further considerations. We could directly reconstruct the distribution using the same reconstruction algorithm described before if we knew the corresponding second- and third-order correlation functions γ_k^{coh}. It is straightforward to show that these correlation functions are given by the asymptotic values of the experimentally observed correlation function. To show this, we use the same notation as in the last chapter writing $\gamma_k(\tau_1 \dots \tau_{k-1}, x)$ to denote the correlation function of the emitted light field for an atom at the position x. If the time arguments of the correlation function are larger than the coherence time of the system, the correlation function factorizes, i.e., $\gamma_k(\tau_1 \dots \tau_{k-1}, x) = \gamma_1(x)^k$, which is equivalent to the k-th order correlation function of a coherent state with the same average photon number. We thus find for the correlation functions of the modulated coherent state:

$$\gamma_k^{\text{coh}} = \int \gamma_1(x)^k P(x)dx = \int \gamma_k(\tau_1 \dots \tau_{k-1}, x) P(x)dx = g^{(k)}(\tau_1 \dots \tau_{k-1})\gamma_1^k \qquad (7.5)$$

where the time arguments have to be larger than the coherence time of the system, i.e., $g^{(k)}(\tau_1 \dots \tau_{k-1})$ are the asymptotic value of the measured correlation functions. In conclusion, we obtain the photon-number distribution of a coherent state with position averaging, $p_{\text{coh}}(n)$, by applying the reconstruction algorithm to the asymptotic values of the measured correlation function.

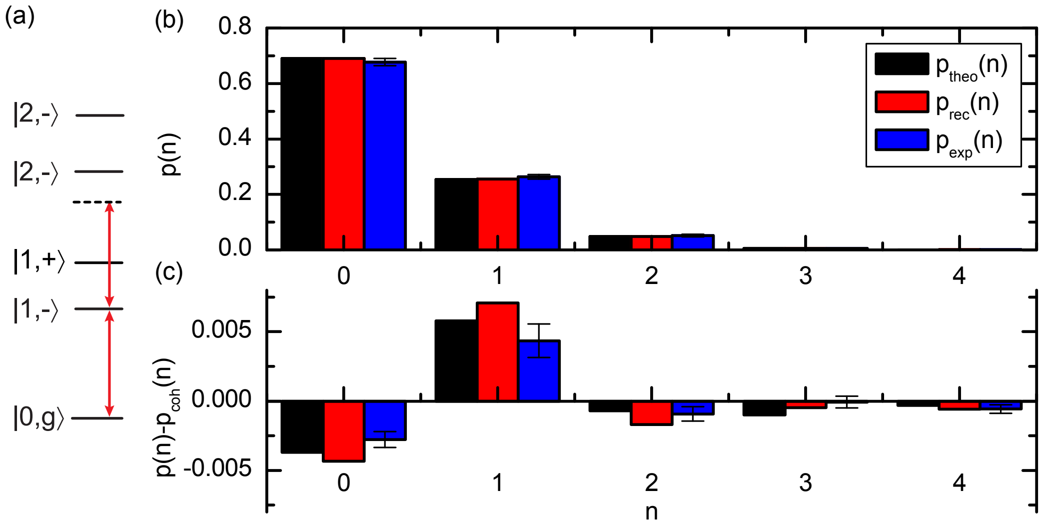

Figure 7.3: (a) The system is driven on resonance with one of the normal modes. Due to the anharmonicity of the Jaynes-Cummings ladder, this implies a detuning from the higher-order dressed states. Therefore, photons enter the cavity preferentially one-by-one. (b) Theoretical photon-number distribution ($p_{\text{theo}}(n)$) and the reconstructed distributions based on theoretical ($p_{\text{rec}}(n)$) and experimental ($p_{\text{exp}}(n)$) correlation functions at a detuning of $\Delta_c/2\pi = -16$ MHz on resonance with one of the normal modes. (c) The difference between the photon-number distribution and the distribution of a modulated coherent state with the same average photon number ($p_{\text{coh}}(n)$, cf. text for details) shows the effect of the photon blockade, namely an enhancement of the single-photon probability, $p(1)$.

7.3 Experimental Results

7.3.1 Photon Blockade

For the measurements depicted in 7.1, the probe laser was detuned by $\Delta_c/2\pi = -16$ MHz with respect to the cavity. This means it is on resonance with the normal modes even for perfectly localized atoms ($g_{\max}/2\pi = 16$ MHz). It is detuned from the higher-order dressed states for all positions of the atoms. Since the normal modes contain only a single excitation, photons are expected to enter the cavity one-by-one. This effect is referred to as a photon blockade [10] in analogy to the Coulomb blockade, which causes electrons to pass through a quantum dot one-by-one [21]. A signature of this behavior is the observation of anti-bunching of the transmitted light [10, 11, 13, 22, 23].

The relevant experimental and theoretical values of the correlation function are summarized in Table 7.1. The asymptotic values are obtained by averaging over times 200 ns $< \tau <$ 250 ns. Due to this averaging, the statistical error bars of the asymptotic values are much smaller than the values at $\tau = 0$, and they can, in fact, be neglected. We see that the second-order correlation function at $\tau = 0$ is smaller than the asymptotic values, which is the first indicator for a photon blockade effect. Because of the atomic motion, the distribution is super-Poissonian though ($g^{(2)}(0) > 1$).

Observable	Experiment	Theory
$\langle a^\dagger a\rangle$	0.39±0.02	0.37
$g^{(2)}(0)$	1.010±0.004	1.002
$g^{(2)}(\tau > 200\ ns)$	1.070	1.097
$g^{(3)}(0,0)$	1.10±0.07	0.98
$g^{(3)}(\tau_1 > 200\ ns, \tau_2 > 200\ ns)$	1.34±0.01	1.31

Table 7.1: Relevant experimental and theoretical values of the correlation functions measured for a detuning of $\Delta_c/2\pi = -16$ MHz on resonance with one of the normal modes. Since the asymptotic values have been obtained by averaging over many data points, the statistical error bars are much smaller and can be neglected.

The reconstructed photon-number distribution is depicted in Fig. 7.3 (b). Even though we find very good agreement between theory (■, black), reconstructed theory (•, red), which was obtained by applying the reconstruction algorithm to the theoretical correlation functions, and experiment (▲, blue), the effect of the photon blockade is not very striking. To observe it, we plot in Fig. 7.3 (c) the difference between the reconstructed photon-number distribution, $p(n)$, and the coherent distribution with modulation, $p_{coh}(n)$ (cf. last section). The photon blockade is now directly visible as a small but well resolved enhancement of the single-photon probability. Note that the absolute values of the effect is very small. The full reconstruction algorithm, including the approximation for the fourth-order correlation function, is necessary to observe it. Theoretical and experimental results are in reasonable agreement.

One comment about the error bars has to be made. In face of the 5 % uncertainty of the detection efficiency, it seems suprising that a change on the order of 0.005 in the photon-number distribution can be observed. However, since $p(n)$ and $p_{coh}(n)$ both depend on the detection efficiency, the uncertainties of both distributions are not independent. Therefore, the absolute error bars of the difference of the two distributions are smaller than the error bars of each individual distribution.

7.3.2 Multi-Photon Gateway

When the detuning of the probe laser with respect to the cavity is reduced, it eventually excites the higher-order dressed states via multi-photon transitions [9, 24]. The successive emission of the multiple photons contained in these states gives rise to bunching in the second-order correlation function [12, 13, 25]. In terms of the photon-number distribution, we expect an enhancement of the two-photon probability. A system that operates under these conditions has been called a two-photon gateway [12].

Experimental and theoretical results at a detuning of $\Delta_c/2\pi = -10$ MHz (η=2.83κ) are plotted in Fig. 7.4. The relevant values of the correlation functions are summarized in Table 7.3.2. In contrast to our last measurement, the correlation functions have a maximum at $\tau = 0$. Applying the reconstruction algorithm yields the photon-number distribution plotted in Fig. 7.5 (b).

As before, we find good agreement between the theoretical and the reconstructed distributions depicted in Fig. 7.5 (b). The difference between the photon-number dis-

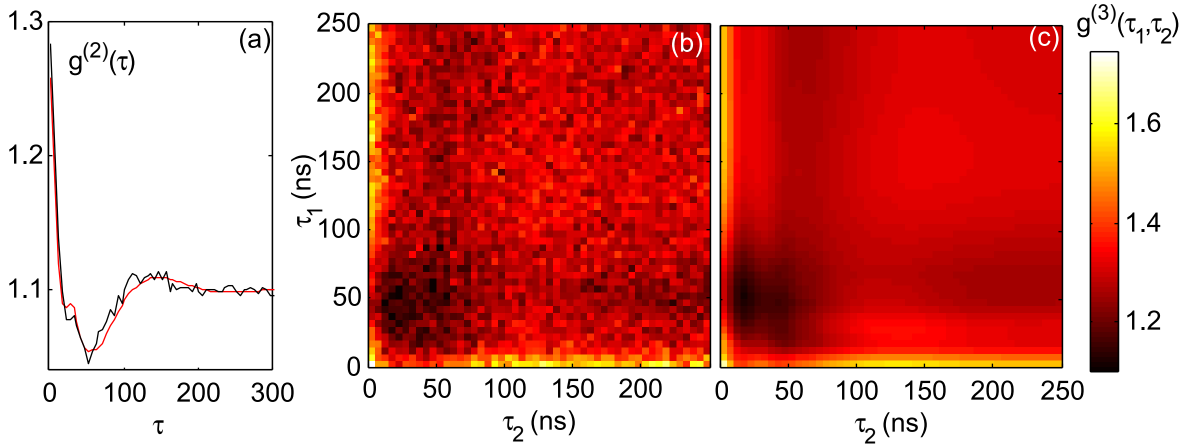

Figure 7.4: (a) Experimental and theoretical second-order correlation function, $g^{(2)}(\tau)$, at a detuning of $\Delta_c = -10$ MHz and a driving strength of $\eta = 2.83\kappa$. Third-order correlation function, $g^{(3)}(\tau_1, \tau_2)$, in the experiment (b) and theory (c).

Observable	Experiment	Theory
$\langle a^\dagger a \rangle$	0.63±0.03	0.58
$g^{(2)}(0)$	1.284±0.003	1.258
$g^{(2)}(\tau > 200\ ns)$	1.099	1.100
$g^{(3)}(0,0)$	1.75±0.05	1.75
$g^{(3)}(\tau_1 > 200\ ns, \tau_2 > 200\ ns)$	1.29±0.01	1.31

Table 7.2: Releavnt values of the correlation functions measured at a detuning of $\Delta_c/2\pi = -10$ MHz.

tribution $p(n)$ and the coherent distribution $p_{\mathrm{coh}}(n)$, shown in Fig. 7.5 (c), has changed profoundly compared to the last section. The most pronounced effect is a reduction of the single-photon probability. As a consequence of the strong driving, not only the second-order dressed state but also the third- and even higher-order dressed states, which are difficult to resolve spectroscopically, are excited. Thus, we find the expected enhancement of the two-photon probability but also an enhancement of the three- and four-photon probability. Note that this enhancement is necessarily accompanied by an increase of the zero photon probability to ensure $\sum n(p(n) - p_{\mathrm{coh}}(n)) = 0$.

7.4 Conclusion and Outlook

We have shown that measurements of the second- and third-order intensity correlation function can be used to reconstruct steady-state photon-number distributions of the atom-cavity system under strong driving. Under these conditions, a reconstruction based on the second-order correlation function only is not sufficient. We have used this technique to reconstruct the photon-number distribution in two different regimes. When the probe light is on resonance with one of the normal modes and sufficiently far detuned

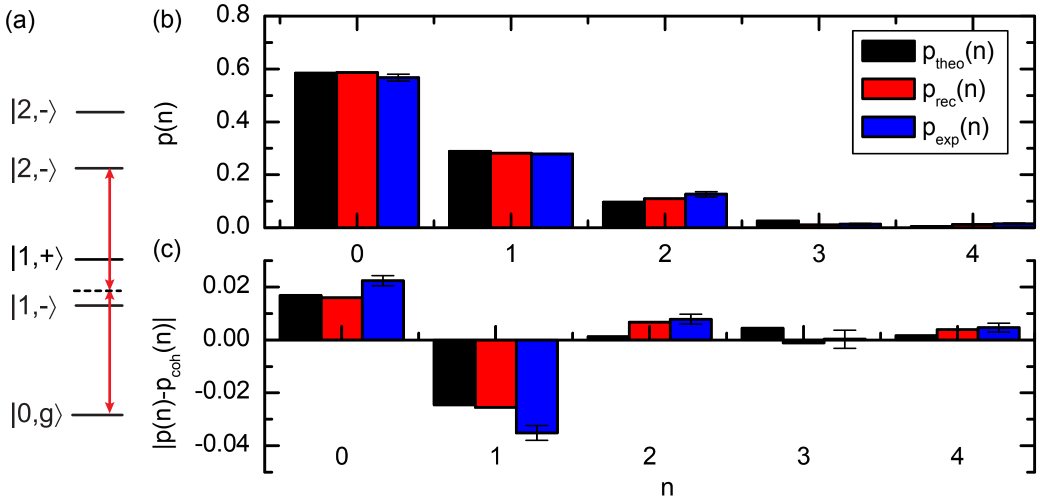

Figure 7.5: (a) The system is driven on resonance with the higher-order dressed states. Multi-photon excitations of these states results in an enhancement of the two- and three-photon probability. (b) Theoretical photon-number distribution ($p_{\text{theo}}(n)$) and the reconstructed distributions based on theoretical ($p_{\text{rec}}(n)$) and experimental ($p_{\text{exp}}(n)$) correlation functions at a detuning of $\Delta_c/2\pi = -10$ MHz on resonance with higher-order dressed states. (c) The difference between the photon-number distribution and the distribution of a modulated coherent state with the same average photon number ($p_{\text{coh}}(n)$) has changed profoundly showing an enhancement of the two and three-photon probabilities.

from the higher-order dressed states, a photon blockade leads to an enhancement of the single-photon probability, whereas the single-photon probabilities is reduced on resonance with the higher-order dressed states. The results are in good agreement with theoretical calculations. They show that correlation functions are a sensible tool to detect even small modifications of the photon statistics. Because of the atomic motion and the strong driving, the absolute effects are rather small. An enhancement can be achieved by performing experiments with trapped atoms and at lower driving strengths.

Further analysis indicates that the accuracy of the reconstruction algorithm is currently mainly limited by the finite binning time used for the evaluation of the correlation functions. A smaller binning could improve the accuracy further. By mixing the emitted light with a weak coherent light source, one can, in principle, even gain information about the coherences of the photonic density matrix [18].

As we have seen in the previous chapter, measurements of the time-dependent second-order correlation function can be interpreted as a time-dependent measurement of the average photon number. Measurements of the time-dependent third-order correlation function yield the time dependence of $\langle a^{\dagger 2} a^2 \rangle$, i.e., the second-order correlation function. Combining this with the techniques introduced in this chapter should, in principle, enable us to reconstruct the time dependence of the photon-number distribution. From this, we expect unprecedented insights into the dynamics of the system.

Another interesting aspect is to analyze the correlation functions with respect to their non-classical properties. For classical states of light, an infinite number of inequalities for the correlation functions can be derived [26]. The most prominent is probably $g^{(2)}(0) \geq 1$. Violations of classical inequalities for the second-order correlation function [10, 22, 27] or intensity-field correlation function [28] have been reported in cavity QED. Classical inequalities for the third-order correlation function have so far only been considered theoretically [26]. A particularly interesting case would be to generate states that do not violate any classical inequalities of the second-order correlation function but only show their non-classical character via third-order correlation functions. A simple example is an equal superposition of a zero- and a two-photon state, which has $g^{(2)}(0) = 1$ but $g^{(3)}(0,0) = 0$.

Bibliography

[1] L. Mandel and E. Wolf, *Optical coherence and quantum optics*, Cambridge University Press (1995).

[2] C. Guerlin, J. Bernu, S. Deléglise, C. Sayrin, S. Gleyzes, S. Kuhr, M. Brune, J.-M. Raimond, and S. Haroche, *Nature* **448**, 889 (2007).

[3] M. Hofheinz, E. M. Weig, M. Ansmann, R. C. Bialczak, E. Lucero, M. Neeley, A. D. O'Connell, H. Wang, J. M. Martinis, and A. N. Cleland, *Nature* **454**, 310 (2008).

[4] M. Hofheinz, H. Wang, M. Ansmann, R. C. Bialczak, E. Lucero, M. Neeley, A. D. O'Connell, D. Sank, J. Wenner, J. M. Martinis, and A. N. Cleland, *Nature* **459**, 546 (2009).

[5] S. Deleglise, I. Dotsenko, C. Sayrin, J. Bernu, M. Brune, J. Raimond, and S. Haroche, *Nature* **455**, 510 (2008).

[6] A. Kuhn, M. Hennrich, and G. Rempe, *Phys. Rev. Lett.* **89**, 067901 (2002).

[7] M. Keller, B. Lange, K. Hayasaka, W. Lange, and H. Walther, *Nature* **431**, 1075 (2004).

[8] J. McKeever, A. Boca, A. D. Boozer, R. Miller, J. R. Buck, A. Kuzmich, and H. J. Kimble, *Science* **303**, 1992 (2004).

[9] I. Schuster, A. Kubanek, A. Fuhrmanek, T. Puppe, P. W. H. Pinkse, K. Murr, and G. Rempe, *Nature Phys.* **4**, 382 (2008).

[10] K. M. Birnbaum, A. Boca, R. Miller, A. D. Boozer, T. E. Northup, and H. J. Kimble, *Nature* **436**, 87 (2005).

[11] C. Lang, D. Bozyigit, C. Eichler, L. Steffen, J. M. Fink, A. A. Abdumalikov, M. Baur, S. Filipp, M. P. da Silva, A. Blais, and A. Wallraff, *Phys. Rev. Lett.* **106**, 243601 (2011).

[12] A. Kubanek, A. Ourjoumtsev, I. Schuster, M. Koch, P. W. H. Pinkse, K. Murr, and G. Rempe, *Phys. Rev. Lett.* **101**, 203602 (2008).

[13] A. Faraon, I. Fushman, D. Englund, N. Stoltz, P. Petroff, J. Vuckovic, A. Faraon, I. Fushman, D. Englund, N. Stoltz, P. Petroff, and J. Vučković, *Nature Physics* **4**, 859 (2008).

[14] J. Kim, S. Takeuchi, Y. Yamamoto, and H. H. Hogue, *Appl. Phys. Lett.* **74**, 902 (1999).

[15] D. T. Smithey, M. Beck, M. G. Raymer, and A. Faridani, *Phys. Rev. Lett.* **70**, 1244 (1993).
[16] M. J. Fitch, B. C. Jacobs, T. B. Pittman, and J. D. Franson, *Phys. Rev. A* **68**, 043814 (2003).
[17] D. Achilles, C. Silberhorn, C. Śliwa, K. Banaszek, and I. A. Walmsley, *Opt. Lett.* **28**, 2387 (2003).
[18] H. Paul, P. Törmä, T. Kiss, and I. Jex, *Phys. Rev. Lett.* **76**, 2464 (1996).
[19] C. D. Cantrell, M. Lax, and W. A. Smith, *Phys. Rev. A* **7**, 175 (1973).
[20] S. Chopra and L. Mandel, *Phys. Rev. Lett.* **30**, 60 (1973).
[21] M. A. Kastner, *Rev. Mod. Phys.* **64**, 849 (1992).
[22] B. Dayan, A. S. Parkins, T. Aoki, E. P. Ostby, K. J. Vahala, and H. J. Kimble, *Science* **319**, 1062 (2008).
[23] D. J. Alton, N. P. Stern, Takao, H. Lee, E. Ostby, K. J. Vahala, and H. J. Kimble, *Nature Phys.* **7**, 159 (2011).
[24] I. Schuster, *Nonlinear spectroscopy of a single-atom-cavity system*, PhD thesis, Technische Universität München (2008).
[25] A. Kubanek, *Two-photon gateway and feedback control of a single atom in a cavity*, PhD thesis, Technische Universität München (2010).
[26] U. M. Titulaer and R. J. Glauber, *Phys. Rev.* **140**, B676 (1965).
[27] G. Rempe, R. J. Thompson, R. J. Brecha, W. D. Lee, and H. J. Kimble, *Phys. Rev. Lett.* **67**, 1727 (1991).
[28] G. T. Foster, L. A. Orozco, H. M. Castro-Beltran, and H. J. Carmichael, *Phys. Rev. Lett.* **85**, 3149 (2000).

Chapter 8

Conclusions and Outlook

A new experimental apparatus has been set up strongly coupling individual rubidium atoms to a single mode of a high-finesse optical resonator. The atoms are injected into the cavity mode via an atomic fountain. They can be trapped in the resonator by means of an intracavity standing-wave dipole trap. Compared to previous experiments, the new apparatus stands out due to the high detection efficiency, a length adjustable cavity and excellent optical access.

In a first experiment, we have investigated the mode spectrum of the empty cavity. A systematic frequency splitting of higher-order Laguerre-Gaussian modes was observed, which is in contradiction with the paraxial approximation. The splitting can be explained quantitatively by a theoretical model taking into account corrections to the paraxial approximation.

The main focus of this work lies on the investigation of the dynamics of the external and internal degrees of freedom of the coupled atom-cavity system. For this purpose, individual atoms were strongly coupled to the cavity, the system was driven by a near-resonant laser and the emitted photon stream was recorded.

By analyzing the time evolution of the transmitted intensity, we gain information about the motional dynamics of the atom trapped in an intracavity dipole trap. We have used this information to cool the radial motion of the atom via feedback. Our results are the first conclusive demonstration of feedback cooling of individual neutral particles. The dramatic increase of the storage time as well as the reduction of the atomic temperature will be essential for future cavity QED experiments. Because of its simplicity, this cooling scheme will also be attractive for experiments with other resonator geometries, in particular those with limited optical access. A further improvement of the performance is expected from the implementation of a blue-detuned dipole trap [1] breaking the radial symmetry [2]. Investigations of more complex feedback strategies, an extension of feedback cooling to the axial motion and the potential to study a small thermodynamic system in the presence of feedback are interesting prospects.

The emitted photon stream also carries information about the internal dynamics of the atom-cavity system, which undergoes a complex quantum trajectory. The coherent time evolution due to the exchange of energy between the atom and the cavity and between the cavity and the driving laser is interrupted by unpredictable quantum jumps owing to spontaneous emission of the atom or photon emission from the cavity. Even though individual emission events are unpredictable, photon pairs and triplets are emitted in a correlated way giving rise to characteristic temporal patterns in the emitted photon stream. We have characterized these patterns by evaluating time-dependent second- and third-order correlation functions. In the second-order correlation function, the coherent exchange of energy between the atom and the cavity (vacuum Rabi oscillations) and between the coupled-atom cavity system and the driving laser (super Rabi oscillations) are directly observed. The third-order correlation function shows an interplay between these processes as well as evidence for the coherent dynamics of the second-oder dressed states of the Jaynes-Cummings ladder. Moreover, a time asymmetry of the emitted photon stream is observed as a consequence of the cascaded emission of single photons and photon pairs. All results are in good agreement with theoretical calculations.

By increasing the probe power, we have entered the strong-driving regime of cavity QED where the driving amplitude exceeds the dissipation rates. Other recent experiments reporting on the observation of the super splitting of the vacuum Rabi resonance [3], super Rabi oscillations [4], phase bistability of the emitted light field [5] and several theoretical proposals [6, 7, 8] highlight a growing interest in this regime. One could expect that the more photons are in the system the smaller are the effects of the quantum fluctuations onto the light field. In other words, the system is expected to act more and more semi-classically. A potential observation of this transition from a quantum to a semi-classical behavior of the system is an interesting perspective.

Apart from changing the drive power and frequency, we could also consider completely different driving schemes. Simple examples are driving the atom instead of the cavity, a pulsed excitation [9] or a two-color excitation to excite the system selectively to higher-order dressed states [10, 11, 12]. A promising aspect with more fundamental implications would be to change the noise characteristics of the driving light field by using for example incoherent [13, 14] or even squeezed light [15, 16].

Another interesting question for future investigations is whether the information gained from the detection of single or multiple photons can be used to influence or even control the quantum trajectory of the system by means of feedback. The idea to apply feedback techniques to open quantum systems has been discussed extensively in theory (e.g., [17] and references therein). In the long term, it offers new possibilities to control and reduce decoherence effects in open quantum systems.

The use of third-order correlation functions might also have an impact on investigations of other open quantum systems whose dynamics and properties are dominated by the interplay of quantum noise and dissipation on the one hand, and coherent evolution and quantum coherence on the other hand. Examples are nano-electronic devices, optomechanical systems or ultracold atoms.

The experiments described in this work have profited heavily from the high detection efficiency of the new experimental apparatus. But so far the length adjustability of the cavity has not been exploited. In the future, we could use it to realize a situation where two atomic transitions are simultaneously on resonance or close to resonance with different longitudinal modes of the cavity. Interesting scenarios are V-type, ladder, Λ-type or N-type level schemes. In this kind of systems, the atom can mediate an effective interaction between the two light modes. Cavity electromagnetically induced transparency (CEIT) [18, 19] or a strong photon blockade [20] are just two examples of effects that can be observed.

Bibliography

[1] T. Puppe, I. Schuster, A. Grothe, A. Kubanek, K. Murr, P. W. H. Pinkse, and G. Rempe, *Phys. Rev. Lett.* **99**, 013002 (2007).

[2] A. Kubanek, M. Koch, C. Sames, A. Ourjoumtsev, T. Wilk, P. Pinkse, and G. Rempe, *Applied Physics B: Lasers and Optics* **102**, 433 (2011).

[3] L. S. Bishop, J. M. Chow, J. Koch, A. A. Houck, M. H. Devoret, E. Thuneberg, S. M. Girvin, and R. J. Schoelkopf, *Nature Phys.* **5**, 105 (2009).

[4] C. Lang, D. Bozyigit, C. Eichler, L. Steffen, J. M. Fink, A. A. Abdumalikov, M. Baur, S. Filipp, M. P. da Silva, A. Blais, and A. Wallraff, *Phys. Rev. Lett.* **106**, 243601 (2011).

[5] M. A. Armen, A. E. Miller, and H. Mabuchi, *Phys. Rev. Lett.* **103**, 173601 (2009).

[6] P. Alsing and H. J. Carmichael, *Quantum Opt.* **3**, 13 (1991).

[7] P. Alsing, D.-S. Guo, and H. J. Carmichael, *Phys. Rev. A* **45**, 5135 (1992).

[8] S. Shamailov, A. Parkins, M. Collett, and H. Carmichael, *Optics Communications* **283**, 766 (2010).

[9] J. Bochmann, M. Mücke, G. Langfahl-Klabes, C. Erbel, B. Weber, H. P. Specht, D. L. Moehring, and G. Rempe, *Phys. Rev. Lett.* **101**, 223601 (2008).

[10] H. J. Carmichael, P. Kochan, and B. C. Sanders, *Phys. Rev. Lett.* **77**, 631 (1996).

[11] T. A. Puppe, *Trapping and observing single atoms in the dark*, PhD thesis, Technische Universität München (2007).

[12] J. M. Fink, M. Göppl, M. Baur, R. Bianchetti, P. J. Leek, A. Blais, and A. Wallraff, *Nature* **454**, 315 (2008).

[13] L. Tian and H. J. Carmichael, *Quantum Opt.* **4**, 131 (1992).

[14] J. M. Fink, L. Steffen, P. Studer, L. S. Bishop, M. Baur, R. Bianchetti, D. Bozyigit, C. Lang, S. Filipp, P. J. Leek, and A. Wallraff, *Phys. Rev. Lett.* **105**, 163601 (2010).

[15] C. W. Gardiner, *Phys. Rev. Lett.* **56**, 1917 (1986).

[16] Q. A. Turchette, N. P. Georgiades, C. J. Hood, H. J. Kimble, and A. S. Parkins, *Phys. Rev. A* **58**, 4056 (1998).

[17] H. M. Wiseman and G. J. Milburn, *Quantum Measurement and Control*, Cambridge University Press, (2009).

[18] M. Mücke, E. Figueroa, J. Bochmann, C. Hahn, K. Murr, S. Ritter, C. J. Villas-Boas, and G. Rempe, *Nature* **465**, 755 (2010).

[19] M. Albert, A. Dantan, and M. Drewsen, *Nature Phys.* **5**, 633 (2011).

[20] M. J. Werner and A. Imamoglu, *Phys. Rev. A* **61**, 011801 (1999).

Appendix **A**

Jaynes-Cummings Hamiltonian in a Rotating Frame

To eliminiate the explicite time-dependence appearing in the driven Jaynes-Cummings Hamiltonian (Eq. 2.7), it is convenient to transform the full Hamiltonian to a rotating frame. As the explicit steps of this transformation are omitted in many text books and articles, this appendix aims to summarize the main steps. It is based on the more general description in [1]. A state, $|\Psi\rangle$, obeying the Schrödinger equation

$$i\hbar\frac{\partial\Psi}{\partial t} = H\Psi \tag{A.1}$$

can be transformed according to

$$|\tilde{\Psi}\rangle = \hat{U}^{\dagger}|\Psi\rangle = \exp\left(i\hat{A}t/\hbar\right)|\Psi\rangle \tag{A.2}$$

where $\hat{U}^{\dagger}$ is a unitary operator generated by an arbitrary hermitian operator $\hat{A}$. It can be shown [1] that the transformed wave function obeys the Schrödinger equation with a modified Hamiltonian

$$\tilde{H} = \hat{U}^{\dagger}H\hat{U} - \hat{A}. \tag{A.3}$$

In the case of the driven Jaynes-Cummings Hamiltonian, $H_{\mathrm{JC}}+H_d$, we chose the operator $\hat{A} = \omega_l(a^{\dagger}a+\sigma_+\sigma_-)$ to generate the unitary transformation $\hat{U}^{\dagger}$. After a short calculation we obtain the transformed Hamiltonian

$$\tilde{H} = \hbar\Delta_a\sigma_+\sigma_- + \hbar\Delta_c a^{\dagger}a + \hbar g(a^{\dagger}\sigma_- + a\sigma_+) + \hbar\eta(a + a^{\dagger}), \tag{A.4}$$

with the detunings $\Delta_a = \omega_l - \omega_a$ and $\Delta_c = \omega_l - \omega_c$. This is the Hamiltonian used for most of the calculations described in this thesis.

Bibliography

[1] S. A. Gardiner. Quantum Measurement, Quantum Chaos, and Bose-Einstein Condensates. Ph.D. thesis, Leopold-Franzens-Universität Innsbruck (2000).

Appendix B

Atomic Distributions

Because of the motion of the atoms with respect to the cavity mode, the coupling constant and, due to the AC-Stark shift of the stabilization laser, the atomic resonance frequency fluctuate. Since the observables that we have considered in this work, such as the average transmission or correlation functions, depend on these parameters, the atomic motion needs to be taken into account when a quantitative comparison of the experimental results with theory is to be made. In the past, Monte-Carlo simulations of the atomic trajectory have been used successfully to reproduce experimental results such as correlation functions [1], normal-mode spectra [2] or the observation of the two-photon resonance [3]. However, these simulations are quite time consuming and can be error-prone, since many physical effects have to be taken into account. Therefore, it is often more convenient to take into account the atomic motion by averaging over a suitable atomic probability distribution function $P(\vec{r})d\vec{r}$. The expectation value of any position-dependent observable $O(\vec{r})$ can then easily be calculated by integrating over this distribution function:

$$\bar{O} = \int O(\vec{r})P(\vec{r})d\vec{r} \tag{B.1}$$

In this work, this technique is used twice under very different circumstances. In Chapter 5, we infer temperature of a trapped atom, which is related to the width of the atomic distribution, from a measurement of the average cavity transmission. Here, we explain the underlying theoretical model and make a comparison with further measurements that strongly support the validity of this model. In contrast to these experiments with trapped atoms, the measurements of the correlation functions, described in Chapter 6 and 7, were performed with passing atoms. Therefore, a very different probability distribution of the atomic position has to be used that will be discussed in the last part of this Appendix.

B.0.1 Average Transmission for Trapped Atoms

The first observable that we are interested in is the average cavity transmission. Under weak excitation, an analytic expression can be derived [4] which yields for the transmission relative to the empty-cavity transmission:

$$T(\vec{r}) = \frac{1}{\left(1 + \frac{2C(\vec{r})}{1+\Delta_a(\vec{r})^2/\gamma^2}\right)^2 + \left(\frac{\Delta_c}{\kappa} - \frac{2C(\vec{r})\Delta_a(\vec{r})}{\gamma(1+\Delta_a(\vec{r})^2/\gamma^2)}\right)^2} \tag{B.2}$$

Here, we have introduced the position-dependent cooperativity $C(\vec{r}) = \frac{g(\vec{r})^2}{2\gamma\kappa}$. The position dependence of the atomic detuning, $\Delta_a = \omega_l - \omega_a$, is a consequence of the AC-Stark shift induced by the dipole trap laser. In cylindrical, coordinates it reads:

$$\Delta_a(r,z) = \Delta_{a0} - 2U_0 \cos(k_t z)^2 \exp\left(-2r^2/w_0^2\right). \tag{B.3}$$

Here, Δ_{a0} is the bare atom detuning without AC-Stark shifts, U_0 is the depth of the dipole potential, $k_t = 2\pi/\lambda_t$ is the wavevector of the trapping light and w_0 the waist of the cavity mode. The factor of two stems from the fact that the ground state and the excited state are shifted by almost the same amount but in opposite directions. To avoid errors due to the periodicity of the potential along the cavity axis, we approximate the cosine square profile by a Gaussian with the same curvature, i.e., $\cos(k_t z)^2 \approx 1 - (k_t z)^2 \approx \exp\left(-(k_t z)^2\right)$. Furthermore, we write the position in terms of the dimensionless variables $R = r/w_0$ and $Z = k_t z/\sqrt{2}$. This leaves us with the position-dependent atomic frequency

$$\Delta_a(R,Z) = \Delta_{a0} - 2U_0 \exp\left(-2R^2 - 2Z^2\right) \tag{B.4}$$

The position dependence of the coupling constant is determined by the profile of the cavity mode

$$g(r,z) = g_0 \cos\left(k_p z\right) \exp\left(-r^2/w_0^2\right). \tag{B.5}$$

The frequency of the dipole trap laser and the probe laser differ by four FSRs. Therefore, both modes overlap perfectly only in the center of the cavity. Moving to other potential wells along the cavity axis degrades the axial overlap. In principle, we have to consider atoms localized in different potential wells. To simplify the calculations, we restrict our treatment to a single potential well, but we allow for some finite axial displacement, z_0, of this well with respect to the anti-node of the probe light. The position dependence of the coupling constant is thus given by

$$g(r,z) = g_0 \cos(k_p(z - z_0)) \exp\left(-r^2/w_0^2\right). \tag{B.6}$$

Apart from this shift, we neglect the small difference in the probe and trap light wavelengths setting $k_t \approx k_p$´. As before, we approximate the axial mode profile by a Gaussian and introduce dimensionless position parameters. We obtain the position-dependent coupling constant

$$g(R,Z) = g_0 \exp\left(-R^2 - (Z - Z_0)^2\right). \tag{B.7}$$

To evaluate the position integration in Eq. B.1, we still need the atomic distribution function $P(\vec{r})$. For an atom in thermal equilibrium in a harmonic potential, the expected Boltzmann distribution reads

$$P(R,Z)Rd\phi\mathrm{d}R\mathrm{d}Z = N\exp\left(\frac{-2(R^2+Z^2)}{\sigma^2}\right)R\mathrm{d}\phi\mathrm{d}R\mathrm{d}Z. \tag{B.8}$$

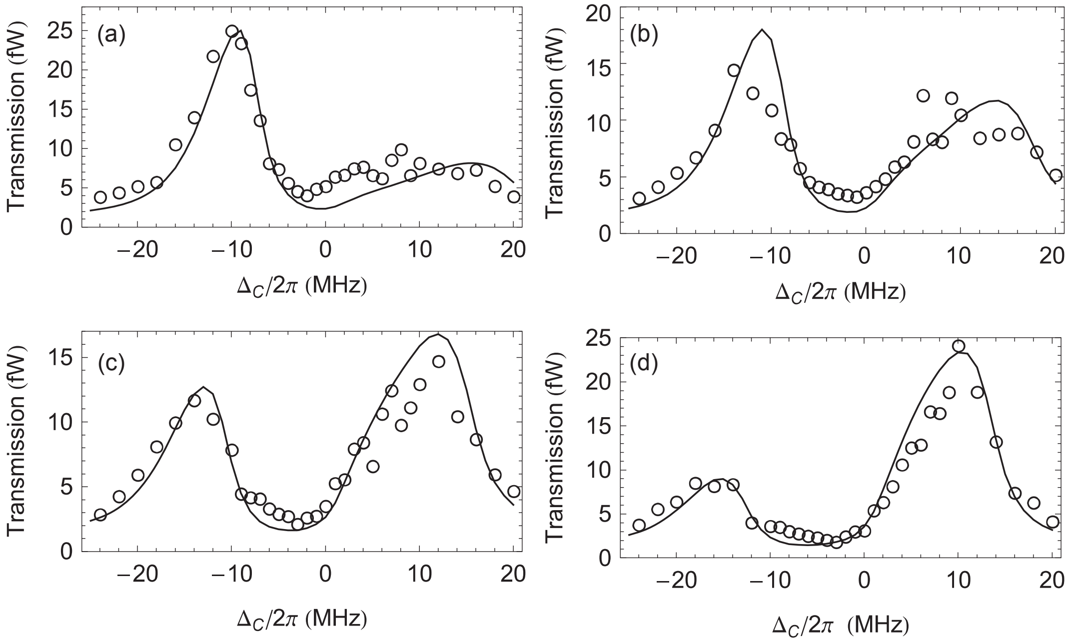

Figure B.1: Experimental (∘) and theoretical (solid line) normal-mode spectra for different dipole trap depths. The four spectra corresponding to a transmitted trap power of 340 nW, 310 nW, 280 nW, 250 nW from (a) to (d)). The width of the atomic distribution ($\sigma = 0.35$), the displacement ($Z_0 = 0.43$), the AC-Stark shift ($2U_0/2\pi = 46$ MHz), the empty-cavity transmission (260 fW) and the dark count rate (1 fW) for the theoretical curves were adjusted manually for plot (a) and then kept constant. Only the Stark-shift was scaled according to corresponding trap power. We find good agreement without any additional fit parameter.

N normalizes the distribution to one. As we discuss later on the width of the distribution, σ, is connected to the atomic temperature.

As we have introduced several approximations, it is desirable to test if our model agrees with the experiment. For this purpose, we first try to reproduce spectroscopic measurements of the normal modes obtained with the old apparatus [2]. The cavity parameters are $g_0 = 2\pi \cdot 16$ MHz and $\kappa = 2\pi \cdot 1.25$ MHz. The bare atom-cavity detuning is $\omega_c - \omega_a = 2\pi \cdot 35$ MHz. Four spectra at four different potential depths were recorded as shown in Fig. B.1. We manually adjust the probe power, dipole potential U_0, the width of the distribution σ, the mode offset Z_0, and a vertical offset due to dark counts to reproduce the first measurement Fig. B.1 (a). Without any additional fit parameter, we are able to reproduce the other spectra as well (Fig. B.1 (b)-(d)). Interestingly, the relatively big discrepancy that can be observed at a dipole trap power of 310 nW (Fig. B.1 (b)) for the left normal mode was also present in the Mont-Carlo simulation described in [2] suggesting that it is caused by a systematic error of the measurement.

We have also applied this model to two normal-mode measurements recorded with the new experimental setup shown in Fig. B.2 (a). The cavity parameters are $g_0 = 2\pi{\cdot}16$ MHz and $\kappa = 2\pi{\cdot}1.5$ MHz. The bare atom-cavity detuning is $\omega_c{-}\omega_a = 2\pi{\cdot}40$ MHz.

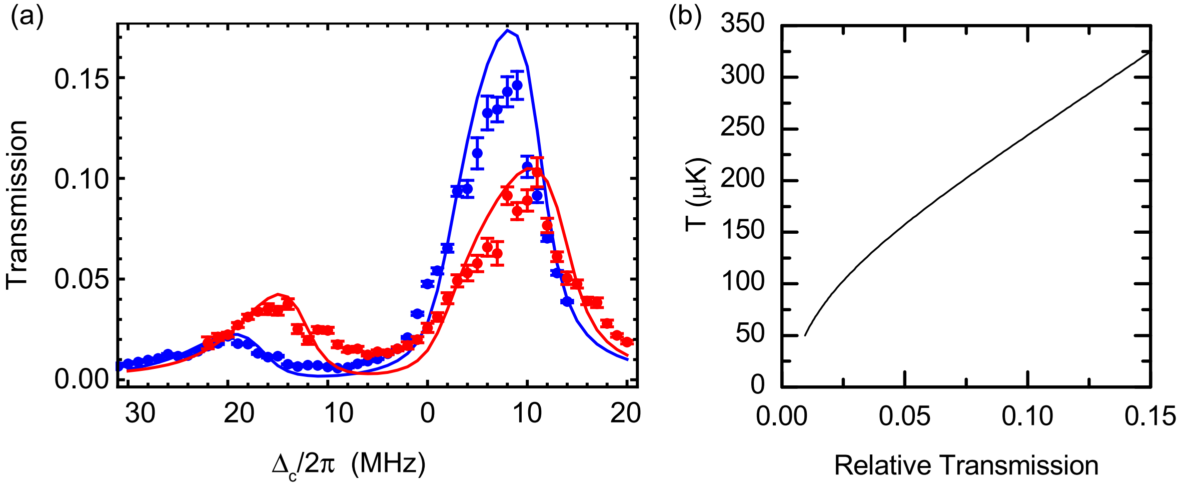

Figure B.2: (a) Normal-mode spectra recorded with the new experimental apparatus at two different dipole potentials. Reasonable agreement between theory (solid lines) and experiment (•) is found for both potential depths, U_0/h = 16.5 MHz (blue) and U_0/h = 20 MHz (red), keeping all other parameters constant (σ = 0.35, Z_0 = 0.43). (b) Fixing the detuning of the probe light, we can determine the temperature from a measurement of the average transmission using this calibration curve (Z_0 = 0.43, $\Delta_c/2\pi$=0 MHz, U_0/h = 20 MHz).

We use the same values of σ and Z_0 as before. The only adjustable parameter is the dipole potential, which we adjust to U_0/h = 16.5 MHz and U_0/h = 20 MHz, respectively. Again, we find good agreement between theory and experiment.

Having shown that our simple model does indeed reproduce experimental measurements with reasonable accuracy, we can now proceed to determine the temperature of a trapped atom from the average transmission. We make use of the fact that the width of the distribution function, σ, is connected to the atomic temperature via

$$\sigma = \sqrt{\frac{k_B T}{U_0}}. \tag{B.9}$$

In Fig. B.2 (b), we have plotted the temperature as a function of the average cavity transmission for the parameters used for the feedback experiments (U_0/h = 20 MHz, $\Delta_c/2\pi$=0 MHz, $\Delta_a/2\pi$=46 MHz, Z_0=0.43). This gauge curve was used to determine the temperature from the transmission measurement described in Section 5.3.4.

B.0.2 Correlation Functions for Passing Atoms

In Chapter 6, we have determined the second- and third-order correlation function for atoms that are passing through the cavity mode. It is obvious that, compared to experiments with trapped atoms, a different distribution function is required. We write $\langle a^\dagger a^\dagger(\tau) a(\tau) a\rangle_{\vec{x}}$ to denote the explicit position dependence of the correlation function. On timescales that are much shorter than the transit time of an atom through the

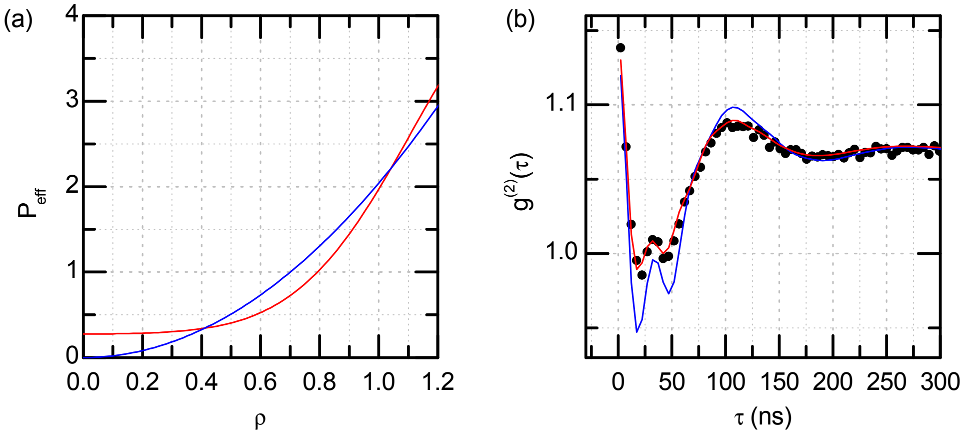

Figure B.3: (a) For homogeneously distributed atoms, a quadratic (blue line) effective distribution is expected. However, a modified distribution (red line) yields much better agreement with the experiment. This is illustrated in (b). The experimental second-order correlation function (•, $\Delta_C = -2\pi \cdot 12$ MHz, $\eta = 3.5\kappa$) is nicely reproduced by the modified distribution (red). The agreement with the quadratic distribution (blue) is considerably worse.

cavity mode, the correlation function that we measure is then given by

$$g^{(2)}(\tau) = \frac{\int \langle a^\dagger a^\dagger(\tau) a(\tau) a\rangle_{\vec{x}} P(\vec{x}) d\vec{x}}{\left(\int \langle a^\dagger a\rangle_{\vec{x}} P(\vec{x}) d\vec{x}\right)^2}. \tag{B.10}$$

For the position-dependent atom-cavity detuning and coupling constant, we use the same expression derived before (cf. eq. B.4 and B.7). However, we neglect the offset between the probe and trap mode setting $Z_0 = 0$. Under this assumption, atom-cavity detuning and coupling constant depend only on the dimensionless, radial position $\rho = \sqrt{R^2 + Z^2}$. If the same holds true for the atomic distribution (i.e., $P(\vec{r}) = P(\rho)$), the three-dimensional position integral appearing in B.1 can be reduced to a one-dimensional integral

$$\bar{O} = \int_0^\infty O(\rho) P(\rho) 4\pi\rho^2 \mathrm{d}\rho = \int_0^\infty O(\rho) P_{\mathrm{eff}}(\rho) \mathrm{d}\rho \tag{B.11}$$

with an effective one-dimensional distribution $P_{\mathrm{eff}}(\rho) = P(\rho)4\pi\rho^2$. This reduction to one dimension greatly simplifies the integration, in particular, for observables, such as correlation functions, whose computation is time consuming.

If the atomic trajectories are neither affected by the resonant probe light nor by the far-detuned laser that is used to stabilize the cavity length, the passing atoms are expected to be distributed homogeneously in the cavity mode, i.e., $P(\rho) = P_0$. This leaves us with the effective one-dimensional distribution $P_{\mathrm{eff}}(\rho) = 4\pi P_0 \rho^2$ plotted in Fig. B.3 (a) (blue line). P_0 normalizes the distribution. As we only consider atoms that cause an increase of the transmission above a certain threshold, the integration has to be truncated at some finite radial position, $\rho_{\max}$. Even by using this truncation and a vertical scaling factor as a fit parameter, we do not find satisfying agreement between experiment and theory (cf. Fig. B.3 (b)). However, a slightly modified distribution (red line in Fig. B.3 (a)) yields much better agreement with the experiment (cf. B.3 (b)). The main difference is a higher probability to find the atom at the center of the cavity mode, which can be attributed to the attractive potential created by the weak dipole trap laser that guides the atoms towards the center of the cavity mode.

This very same distribution is used for all the theoretical calculations presented in Chapter 6 and 7. For each individual measurement, we adjust the truncation parameter, ρ_{max}, and we allow for a small adjustment of the atom-cavity detuning of ±1 MHz.

Bibliography

[1] P. Münstermann, T. Fischer, P. W. H. Pinkse, and G. Rempe, *Opt. Comm.* **159**, 63 (1999).

[2] P. Maunz, T. Puppe, I. Schuster, N. Syassen, P. W. H. Pinkse, and G. Rempe, *Phys. Rev. Lett.* **94**, 033002 (2005).

[3] I. Schuster, A. Kubanek, A. Fuhrmanek, T. Puppe, P. W. H. Pinkse, K. Murr, and G. Rempe, *Nature Phys.* **4**, 382 (2008).

[4] T. Fischer, P. Maunz, P. W. H. Pinkse, T. Puppe, and G. Rempe, *Phys. Rev. Lett.* **88**, 163002 (2002).

Appendix C

Evaluating Correlation Functions

In the following, we summarize how the correlation functions $g^{(2)}(\tau)$ and $g^{(3)}(\tau_1,\tau_2)$ are evaluated and normalized. To make sure that an atom is present, we evaluate the correlation function only for intervals in which the average transmission surpasses the empty-cavity transmission by a certain threshold (cf. Chapter 6). For each of these intervals with duration T_i, we count the number of photon pairs, $n_i(\tau)$, separated by the time τ within some binning time Δt (5 ns unless otherwise stated). Because of the dead time and after pulsing of the detectors, we only evaluate photon pairs that arrive at different detectors. The finite interval duration T_i is taken into account by multiplying with a normalization factor of $(1-\tau/T_i)^{-1}$. Next, the coincidence counts $n_i(\tau)$ for all intervals are summed up. At last, the correlation function has to be normalized to the number of coincidences that is expected for uncorrelated, i.e., statistically independent clicks. As the probability to detect a single photon within the binning time is $\Delta t N/T$ (where N is the total number of photon clicks and T the sum of the duration of all the intervals), the expected number of uncorrelated coincidences is $\Delta t N^2/T$. Multiplying this by the probability that the two clicks are registered by different detectors, which is 0.75 in our case, we end up with the normalized time-dependent second-order correlation function

$$g^{(2)}(\tau) = \frac{T}{0.75N^2\Delta t}\sum_i \frac{n_i(\tau)}{1-\tau_2/T_i}. \tag{C.1}$$

The generalization to the third-order correlation function is straightforward. This time, we count the number of triple coincidences $n_{3,i}(\tau_1,\tau_2)$ with the time separations τ_1 and τ_2 between the first and second click, and the second and third click, respectively. The expected number of uncorrelated photon clicks is $\Delta t^2 N^3/T^2$ and the probability that all three photons hit different detectors is 0.375. In total, we find

$$g^{(3)}(\tau_1,\tau_2) = \frac{T^2}{0.375N^3\Delta t^2}\sum_i \frac{n_{3,i}(\tau_1,\tau_2)}{1-\frac{\tau_2+\tau_1}{T_i}}. \tag{C.2}$$

Appendix D

Detailed Balance and Time-Asymmetric Fluctuations

The principle of detailed balance plays a central role in classical statistical mechanics [1, 2]. For example, it simplifies the calculation of stationary states of a system, and it is the basis of the Onsager reciprocal relations [3]. Its definition is most straightforward for a classical system described by a set of discrete states, labeled by l, that undergoes random transitions between the states l and k at a rate γ_{kl}. The time evolution of the probability $p_l(t)$ of finding the system at the time t in the state l is described by a (classical) master equation:

$$\frac{dp_l(t)}{dt} = \sum_k \gamma_{lk} p_k(t) - \gamma_{kl} p_l(t) \tag{D.1}$$

A steady-state solution, $\frac{dp_l^s}{dt} = 0$, of this master equation is said to be in detailed balance if the transition amplitudes between each pair of states is balanced, i.e., $\gamma_{lk} p_k^s = \gamma_{kl} p_l^s$. A more general definition of the detailed balance condition for a classical system, which is described by the distribution function $p(b,t)$ of some arbitrary observable b, is given in [1]: The steady-state distribution $p^s(b)$ is in detailed balance, if the transition rate from b' to b is balanced by the time reversed transition from b to b', i.e.,

$$p(b,\tau|b',0)p^s(b') = p(\epsilon b',\tau|\epsilon b,0)p^s(b). \tag{D.2}$$

Here, $p(b,\tau|b',0)$ is the conditional probability to find the system in the state b at the time τ after an initial occupation of the state b'. The ϵb designates the time reversed observable (e.g., $\epsilon x = x$ and $\epsilon v = -v$ for position and velocity, cf. [1] for a detailed discussion). One important consequence of detailed balance is that two-time correlation functions of arbitrary observables A and B are time symmetric, i.e., $\langle A(\tau)B\rangle = \epsilon_A \epsilon_B \langle B(\tau)A\rangle$ where ϵ_A and ϵ_B is the parity of the respective operators under time reversal. A stationary state of a closed system always fulfills detailed balance as a consequence of the microreversibility (i.e., time reversal invariance) of the underlying physical laws [2]. For an open system, the situation is more delicate. In thermal equilibrium, detailed balance always holds. However, a driven system can assume a steady state with or without detailed balance.

Theoretical investigations of open quantum systems (e.g., lasers) in the 60s and 70s established a lot of parallels to classical statistical mechanics. This naturally stimulated the question, whether, and how, the principle of detailed balance can be generalized to this kind of systems. The generalization is not trivial, since the quantum master equation for the density matrix (cf. Chapter 2) does usually not have the same diagonal form as Eq. D.1. While transitions between the diagonal elements are analogous to Eq. D.1, the appearance of non-diagonal elements inhibits the use of our previous definition of detailed balance. Therefore, Agarwal [4] has proposed an alternative definition based on the mentioned time reversal symmetry of the correlation functions. According to this definition, an open quantum system is in detailed balance if the two-time correlation functions of arbitrary system operators $\hat{A}$ and $\hat{B}$ are symmetric in time, i.e.,

$$\langle \hat{A}(\tau)\hat{B}\rangle = \epsilon_A \epsilon_B \langle \hat{B}(\tau)\hat{A}\rangle. \tag{D.3}$$

It has been shown that this condition, just like the classical counterpart, follows from microreversibility for a closed quantum system and it relaxes to the classical definition of detailed balance for a diagonal master equation [5].

In a more recent paper by Denisov et al. [6], it was argued that the observation of a time asymmetry of a time and normally ordered correlation function in driven open quantum systems demonstrates a violation of Eq. D.3. It can thus be considered as a consequence of the breakdown of detailed balance. Even though the authors only discuss intensity-field and second-order, cross-correlation functions explicitly, the same arguments are also applicable to the asymmetry of the third-order correlation function that we observe here

$$\langle a^\dagger a^{\dagger 2}(\tau) a^2(\tau) a\rangle \neq \langle a^{\dagger 2} a^\dagger(\tau) a(\tau) a^2\rangle. \tag{D.4}$$

However, the connection between a normally ordered correlation function as it appears in Eq. D.4 and Eq. D.3 is by far not trivial. As this issue is neither discussed in [6] nor in the more detailed account in [7], we would like to summarize the underlying reasoning in the following. We have to thank Howard Carmichael for pointing out these arguments in a private communication.

First, we note that measurements (the detection of photons) are performed not directly on the cavity field but on the field that is leaking from the cavity. In the framework of the input-output formalism of cavity QED [8, 9], this output field can be written as a sum of the field leaking from the cavity and the input field:

$$a_{\mathrm{out}}(t) = \sqrt{2\kappa} a + a_{\mathrm{in}}(t). \tag{D.5}$$

Strictly speaking, our measurement thus shows

$$\langle a^\dagger_{\mathrm{out}} a^{\dagger 2}_{\mathrm{out}}(\tau) a^2_{\mathrm{out}}(\tau) a_{\mathrm{out}}\rangle \neq \langle a^{\dagger 2}_{\mathrm{out}} a^\dagger_{\mathrm{out}}(\tau) a_{\mathrm{out}}(\tau) a^2_{\mathrm{out}}\rangle. \tag{D.6}$$

This is equivalent (except for the normalization) to the correlation function of the intracavity field, which we have discussed so far, only in the case of vacuum input fields. Next, we make use of the fact that the output fields commute like free fields [8, 9], i.e.,

$$[a_{\mathrm{out}}(\tau), a^\dagger_{\mathrm{out}}(\tau')] = \delta(\tau - \tau'), \tag{D.7}$$

to regroup Eq. D.6:

$$\langle a_{\mathrm{out}}^{\dagger 2}(\tau) a_{\mathrm{out}}^{2}(\tau) a_{\mathrm{out}}^{\dagger} a_{\mathrm{out}} \rangle \neq \langle a_{\mathrm{out}}^{\dagger}(\tau) a_{\mathrm{out}}(\tau) a_{\mathrm{out}}^{\dagger 2} a_{\mathrm{out}}^{2} \rangle. \tag{D.8}$$

Now, by defining the operators $\hat{A}(\tau) = a_{\mathrm{out}}^{\dagger 2}(\tau) a_{\mathrm{out}}^{2}(\tau)$ and $\hat{B}(\tau) = a_{\mathrm{out}}^{\dagger}(\tau) a_{\mathrm{out}}(\tau)$ with $\epsilon_A = \epsilon_B = +1$, we see that this inequality does indeed represent a violation of Eq. D.3.

Unfortunately, there is still one subtle issue. Agarwal's original definition of detailed balance for open quantum systems [4] only refers to correlation functions involving system operators $\hat{A}$ and $\hat{B}$. The output fields do also depend on the state of the reservoir, i.e., the input field. Since measurements are always performed on the output field, this generalization of the detailed balance condition, which was assumed implicitly in [6], is very natural from an experimental point of view. However, a discussion of possible theoretical consequences is beyond the scope of this work.

Bibliography

[1] C. Gardiner, *Handbook of Stochastic Methods: for Physics, Chemistry and the Natural Sciences*, Springer (2004).

[2] N. V. Kampen, *Stochastic Processes in Physics and Chemistry, Third Edition*, North Holland (2007).

[3] L. Onsager, *Phys. Rev.* **37**, 405 (1931).

[4] G. S. Agarwal, *Z. Phys. B* **258**, 409 (1973).

[5] H. J. Carmichael and D. F. Walls, *Z. Phys. B* **23**, 299 (1976).

[6] A. Denisov, H. M. Castro-Beltran, and H. J. Carmichael, *Phys. Rev. Lett.* **88**, 243601 (2002).

[7] A. Denissov, *Conditional homodyne detection and time asymmetric fluctuations of light*, PhD thesis, University of Oregon (2004).

[8] C. W. Gardiner and M. J. Collett, *Phys. Rev. A* **31**, 3761 (1985).

[9] D. F. Walls and G. F. Milburn, *Quantum Optics*, Springer, Berlin (2007).

List of Publications

[1] M. Zeppenfeld, M. Koch, B. Hagemann, M. Motsch, P.W.H. Pinkse, and G. Rempe,”*Spin-Orbit Coupling in a Fabry-Perot Resonator via Berry's Geometric Phase*”, submitted for publication (2011).

[2] M. Koch, C. Sames, B. Balbach, H. Chibani, A. Kubanek, K. Murr, T. Wilk, and G. Rempe, ”*Three-Photon Correlations in a Strongly Driven Atom-Cavity System*”, Physical Review Letters **107**, 023601 (2011).

[3] A. Ourjoumtsev, A. Kubanek, M. Koch, C. Sames, P. W. H. Pinkse, G. Rempe, and K. Murr.”*Observation of squeezed light from one atom excited with two photons*” Nature **474**, 623 (2011).

[4] A. Kubanek, M. Koch, C. Sames, A. Ourjoumtsev, T. Wilk, P. W. H. Pinkse, and G. Rempe.”*Feedback control of a single atom in an optical cavity*” Applied Physics B **102**, 433 (2011).

[5] M. Koch, C. Sames, A. Kubanek, M. Apel, M. Balbach, A. Ourjoumtsev, P. W. H. Pinkse, and G. Rempe. ”*Feedback Cooling of a Single Neutral Atom*”, Physical Review Letters **105**, 173003 (2010).

[6] A. Kubanek, M. Koch, C. Sames, A. Ourjoumtsev, P. W. H. Pinkse, K. Murr, and G. Rempe. ”*Photon-by-photon feedback control of a single-atom trajectory*”, Nature **462**, 898 (2009).

[7] A. Kubanek, A. Ourjoumtsev, I. Schuster, M. Koch, P. W. H. Pinkse, K. Murr, and G. Rempe.”*Two-Photon Gateway in One-Atom Cavity Quantum Electrodynamics*”, Physical Review Letters **101**, 203602 (2008).

Danksagung

L'art c'est mois, la science c'est nous.
Claude Bernard

Das **Wir**, von dem auf den zurückliegenden Seiten so oft die Rede war, schließt zahlreiche Menschen ein, die über Jahre mit Hirn, Hand und Herz einen Beitrag zum Gelingen dieser Arbeit geleistet haben. Zu guter Letzt ist es mir eine Ehre und ein Vergnügen, diesen Menschen einen Namen zu geben.

Zunächst danke ich natürlich meinem Doktorvater **Gerhard Rempe** für die einzigartige Möglichkeit unter exzellenten Rahmenbedingungen der eigenen Neugier zu folgen und verrückte Ideen im Labor zu verwirklichen. Seine Freude an der Physik und sein stetes Beharren auf einer einfachen, anschaulichen Erklärung finden sich hoffentlich auch in dieser Arbeit wieder.

Ingrid Schuster und **Johannes Almer** gebührt als Mutter und Vater des längenveränderbaren Resonators eine besondere Erwähnung. Ihre Vorarbeit war der Ausgangspunkt für alles, was hier beschrieben wurde.

Mein ganz besonderer Dank gilt meinen Laborkollegen **Borys Hagemann**, **Christian Sames**, **Matthias Apel**, **Maximilian Balbach** und **Haytham Chibani**, die über die Jahre als Diplomanden und Doktoranden mit ihrem Fleiß, Ideenreichtum, Sachverstand und ihrer Wissbegierde das Experiment zu dem gemacht haben, was es heute ist. Ihre Handschrift findet sich in allen Ecken und Enden dieser Arbeit wieder.

Gleiches gilt auch für die vielen wichtigen Ideen und Diskussionen, die die Doktoren **Pepijn Pinkse**, **Karim Murr** und **Tatjana Wilk** beigesteuert haben. Ein besonderer Dank gilt Tatjana für das Korrekturlesen dieser Arbeit.

Alexander Kubanek und **Alexei Ourjoumtsev**, die letzte Besatzung des alten Experiments, haben unter anderem durch die Weitergabe ihres Wissens über die Stärken und Schwächen der alten Apparatur, über Feedback und über homodyne Messtechniken einen wichtigen Beitrag geleistet. Was die Entwicklung des neuen Experiments angeht, war außerdem die Lektüre der *alten Meister* (**Peter Münstermann**, **Thomas Fischer**, **Peter Maunz** und **Thomas Puppe**) äußerst hilfreich. **Andreas Fuhrmanek** hat mich sehr kompetent in das Simulationsprogramm eingewiesen.

Nicht hoch genug loben kann man die Arbeit von **Josef Bayerl**. Dieser hat nicht nur die gesamte mechanische Apparatur inklusive längenveränderbarer Resonator, Schwingungsisolierung und Vakuumkammer am Computer entworfen sondern auch die zeitnahe und einwandfreie Fertigung sichergestellt.

Franz Denk und **Helmuth Stehbeck** wussten zu jedem technischen Problem eine Lösung. Das Einfliegen der Vakuumkammer über einen Kran sei hier nur stellvertretend genannt als einer ihrer zahllosen großen und kleinen Beiträge. Gleiches gilt auch für **Thomas Wiesmeier**, der bei Fragen zur Elektronik und zur Kaffeemaschine stets ein kompetenter Ansprechpartner war.

Martin Zeppenfelds beeindruckende Rechnungen zum Modenspektrum des leeren Resonators zeigen, dass auch ein leerer Resonator voller interessanter Physik steckt, und sind der Ursprung von Kapitel 4 dieser Arbeit.

Manuel Uphoff, **Raul Teixeira**, **Fabian Biebl** und **Patrick Buerckstuemmer** haben als studentische Hilfskräfte und Praktikanten an verschiedenen Stellen in und um den experimentellen Aufbau ihre Spuren hinterlassen.

Allen Mitgliedern der Arbeitsgruppe danke ich für den regen Austausch von Wissen, Ideen und Equipment. Eine besondere Erwähnung verdienen **Thomas Rieger**, dessen Labor und Lasersystem wir übernommen haben, **Michael Motsch** für seine Einweisung in die Vakuumtechnik, **Jörg Bochmann**, **Carolin Hahn** und **Stefan Ritter** für die Wartung des Frequenzkamms sowie **Odette Gori** und **Christina Becker** für die adminstrative Unterstützung.

Howard Carmichael war so freundlich, meine Fragen zum Thema Detailed-Balance ausführlich zu beantworten.

Als Letztes gilt mein tiefster Dank **meinen Eltern** und **Katharina** für die kontinuierliche Unterstützung bei allen Fragestellungen und Problemen jenseits der Physik.